UNIVERSITEIT VAN PRETORIA
UNIVERSITY OF PRETORIA
YUNIBESITHI YA PRETORIA

High-content and super-resolution microscopy reveals the dynamic nuclear architecture and mobile epigenetic marks in *Plasmodium falciparum*

Caron A. Griffiths

Submitted in partial fulfillment of the requirements for the degree *Magister Scientiae* in Biochemistry in the Faculty of Natural and Agricultural Sciences

University of Pretoria

August 2012

Supervisors: Prof L Birkholtz (University of Pretoria)
Dr M Mhlanga (Council for Scientific and Industrial Research)

© University of Pretoria

Submission declaration:

I, Caron A. Griffiths, declare that this dissertation, which I hereby submit for the degree *Magister Scientiae* in the Department of Biochemistry, at the University of Pretoria, is my own work and has not previously been submitted by me for a degree at this or any other institution.

Signature: .....

Date: 24/11/2012....

UNIVERSITEIT VAN PRETORIA
UNIVERSITY OF PRETORIA
YUNIBESITHI YA PRETORIA

Plagiarism Declaration

UNIVERSITY OF PRETORIA

FACULTY OF NATURAL AND AGRICULTURAL SCIENCES

DEPARTMENT OF BIOCHEMISTRY

Full name: Caron Adrienne Griffiths Student number: 26171946

Title of the work: High-content and super-resolution microscopy reveals the dynamic nuclear architecture and mobile epigenetic marks in *Plasmodium falciparum*

Declaration

1. I understand what plagiarism entails and am aware of the University's policy in this regard.
2. I declare that this dissertation (e.g. essay, report, project, assignment, dissertation, thesis etc) is my own, original work. Where someone else's work was used (whether from a printed source, the internet or any other source) due acknowledgement was given and reference was made according to departmental requirements.
3. I did not make use of another student's previous work and submit it as my own.
4. I did not allow and will not allow anyone to copy my work with the intention of presenting it as his or her own work.

Signature 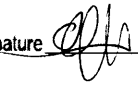 Date 21/11/2012

Acknowledgments:

To my supervisors:

- Dr Musa Mhlanga, for his mentorship, willingness to invest in me, training, guidance and patience;
- Prof Lyn-Marie Birkholtz, for her support, guidance, encouragement and patience;

To my friends and family, for their support, encouragement, faith and understanding, from both near and afar; particularly Mom, Nellis, Dad and Michael;

To Ashley, for his love, support, patience and encouragement;

To the members of the Mhlanga lab, for all of their help, encouragement and much needed laughter;

To all my willing donors and drawers, for literally giving of themselves for this work: Sr Lebitso, Tasha, Sam, Janine, Olona, Florine, Karl-Robert and Juergen;

To Theresa Coetzer (University of Witwatersrand, Johannesburg) and Artur Scherf (Institut Pasteur, Paris) for providing us with the anti-PfMyb2 and anti-PfNup1 antibodies, respectively;

To the Parliamentary grant to the CSIR and the DST grant to the Synthetic Biology Emerging Research Area, for funding this research;

To the CSIR Human Capital Development and Studentship programs, for financially supporting me in my studies.

Soli Deo gloria

Dissertation Summary

The malaria-causing parasite *Plasmodium falciparum* is dependent on tightly regulated gene expression for its progression through the intra-erythrocytic life cycle, pathogenesis and establishment of persistent infection by evasion of the human host's immune system. Evidence points towards *P. falciparum* being unusually dependent on nuclear architecture and genomic organisation for the control of gene expression. Spatially defined nuclear regions of transcriptional activity have been detected and the spatial positioning of loci may determine their transcriptional potential. Additionally, a number of epigenetic markers have been shown to occupy spatially distinct sub-compartments of the nuclear volume. Limitations of microscopic assays used until now have left us with a stereotyped and incomplete image of the organisation of the parasite nucleus and the transcriptional and epigenetic factors involved in the regulation of parasite gene expression, and the possible dynamics thereof.

This work focused on the use of high-content and super-resolution fluorescent microscopy for the study and graphical representation of the spatial organisation of various nuclear factors involved in transcriptional regulation in *P. falciparum* parasites. The first objective (chapter 2) establishes *P. falciparum* parasite sample preparation and fluorescent labeling techniques for microscopy. Immunofluorescent labeling of *var* gene associated transcription repressive and permissive histone modifications, H3K9me3 and H3K9ac, respectively, as well as serine 2-phosphorylated RNA polymerase II and the putative transcription and splicing factor PfMyb2, was optimised. DNA fluorescent *in situ* hybridisation was also optimised for labeling of *var* gene exons. In the second objective (chapter 3), the assays established in the previous chapter are used for high-content combinatorial labeling in thousands of nuclei, followed by analysis using a bespoke computational algorithm for the detection and classification of different labeling patterns. This approach revealed a high level of diversity in the nuclear distributions of each assayed target. Super-resolution stochastic optical reconstruction microscopy was used to further study the sub-diffraction organisation of selected labeling patterns.

The data presented in this dissertation reveal that the complex spatial organisation of certain nuclear factors is subject to greater diversity within the nucleus of *P. falciparum* parasites than previously thought.

Table of Contents

List of Figures

List of Tables

List of Abbreviations

AdSucSyn	Adenyl succinate synthetase
BCIP-T	5-bromo-4-chloro-3-indolyl phosphate, *p*-toluidine salt
BrUTP	5-Bromouridine 5'-triphosphate
BSA	Bovine serum albumin
ChIP	Chromatin immunoprecipitation
CTPSyn	CTP synthetase
DAPI	4',6-diamidino-2-phenylindole
DNA	Deoxyribonucleic acid
EDTA	Ethylenediaminetetraacetic acid
EM	Electron microscopy
FISH	Fluorescent *in situ* hybridisation
FITC	Fluorescein isothiocyanate
gDNA	Genomic DNA
HEPES	4-(2-hydroxyethyl)-1-piperazineethanesulfonic acid
HPLC	High-Pressure Liquid Chromatography
IF	Immunofluorescence
IMP-DHG	Inosine monophosphate dehydrogenase
H3K9ac	Histone H3 lysine 9 acetylation
H3K4me2	Histone H3 lysine 4 dimethylation
H3K4me3	Histone H3 lysine 4 trimethylation
H3K9me3	Histone H3 lysine 9 trimethylation
H3K79me3	Histone H3 lysine 79 trimethylation
H4K20me3	Histone H4 lysine 20 trimethylation
MSP1	Merozoite surface protein 1
mRNA	Messenger RNA
NA	Numerical aperture
ncRNA	Non-coding RNA
NBT	Nitro blue tetrazolium
Nop1	Nucleolar marker
Nup1	Nuclear pore complex marker
NPC	Nuclear pore complex

PALM	Photoactivatable light microscopy
PBS	Phosphate buffered saline
PCR	Polymerase chain reaciton
PERC	Perinuclear repressive center
PFA	Paraformaldehyde
PfEMP-1	*P. falciparum*-infected erythrocyte membrane protein 1
PfHP1	*P. falciparum* heterochromatin protein 1
PfMyb2	*P. falciparum* Myb2
PfOrc1	*P. falciparum* Origin-of-recognition-complex 1
PfSIR2	*P. falciparum* Silent information regulator 2
RAMA	Rhoptry associated merozoite antigen
RAP1	Rhoptry associated protein 1
RAP3	Rhoptry associated protein 3
RBC	Red blood cell
RNA	Ribonucleic acid
RNase	Ribonuclease
RNAPII	RNA polymerase II
RPMI	Roswell Park Memorial Institute
SAGA	Spt-Ada-Gcn5-acetyltransferase complex
SIR	Silent information regulator
SSC	Saline-sodium citrate buffer
SSPE	Saline-sodium phosphate-EDTA buffer
STORM	Stochastic optical reconstruction microscopy
rRNA	Ribosomal ribonucleic acid
TBE	Tris-borate EDTA
TE	Tris-EDTA
UTP	Uridine 5'-triphosphate

Guide to Appendices

- **Appendix A:**
  - A.1: Additional information regarding STORM imaging and analysis
  - A.2: Additional imaging results from assay establishment and optimisation
  - A.3: smFISH probe sequences
  - A.4: smFISH conjugation and purification results

- **Appendix B:**
  - B.1: Computational image processing protocol
  - B.2: Additional images results for dual labeling and classification

- **Appendix C:**
  - C1: Euclidean Norm analysis results

Chapter One

Introduction

1.1. The cell nucleus is organised into different compartments.

The eukaryotic nucleus is often referred to as the "control hub" of the cell. It is the organelle from which functions such as gene expression and genomic duplication steer the functioning and fate of the cell and, ultimately, the organism. The nucleus itself is dependent on a complex three-dimensional spatial organisation of its contents, firstly to allow the DNA polymer, which in higher metazoans can be up to a meter in length, to be contained within a micrometer volume and secondly to sequester functionalities and transcriptional states of genes. Despite the lack of internal membrane-defined sub-organelles, this complex organelle is organised into various morphologically and functionally distinct spatial compartments (reviewed in Misteli 2005). These compartments, also termed domains, can often be characterised by the enrichment of specific proteins or complexes that serve to spatially segregate and regulate many of the fundamental processes carried out within the nucleus. A prototypic example of one such functionally defined nuclear domain may be that of the nucleolus. This domain functions in relation to ribosomal gene regulation, serving as a site of ribosomal gene expression, rRNA processing and ribosome assembly (Xu and Cook, 2008); yet the domain has no physical separation from the rest of the nucleus. A cell's genetic material is equally subject to spatial organisation and compartmentalisation within the nucleus. As such, nuclear architecture is an important determining factor in genome organisation and plays an important role in the regulation of gene expression.

1.2. The cell's genome is subject to compartmentalisation within the nucleus.

The packaging of the totality of a cell's genomic material into the nuclear volume requires not only a high degree of compaction, but also a system of organisation that allows any specific region of the genome to be unpacked, accessed and repacked, as required (Figure 1.1). Chromatin organisation occurs by the non-random packing at

both the level of chromosomes and the entire genome. Each of a cell's individual chromosomes are non-randomly organised into their own discrete chromosome domains (reviewed in Cremer and Cremer, 2001) (Figure 1.1A). Chromosomes are highly compacted within these domains, partly by the tight coiling of double-stranded DNA around histones to form nucleosomes. These are further coiled to form densely folded 30 nm chromatin fibres. Further condensation of individual chromosomes has been suggested to occur by a "fractal globule" model, in which chromosomes are compacted by the dense folding of the polymer into a series of small globules, which are in turn folded in on themselves forming a dense, knot-free conformation (Lieberman-Aiden *et al.*, 2009) (Figure 1.1B). This model allows for the folding and unfolding of chromosomal regions as required, as individual loci can be unpackaged for processing and repacked without the formation of knots.

Variable degrees of chromatin compaction within chromosome domains effectively divide the genome into two discrete spatial compartments. One compartment consists of loosely compacted gene dense regions, or euchromatin; the other consists of heterochromatic densely compacted gene poor regions. Such compartments are generally considered transcriptionally active or repressive regions, respectively (Schneider and Grosschedl, 2007; Lieberman-Aiden *et al.*, 2009). Even so, the assignment of a gene locus to one or the other genomic compartment alone is insufficient to ensure a given transcriptional status or potential for the gene. Instead, there is a large body of evidence showing that gene expression is also strongly dependent on a loci's sub-nuclear position, its interactions with other regulatory molecules, as well as chemical histone modifications (Schneider and Grosschedl, 2007; Sexton *et al.*, 2007; Kumaran *et al.*, 2008).

1.3. The spatial positioning of loci contributes to gene regulation.

The close packaging of chromatin within chromosome domains presents a physical barrier to the transcriptional machinery, which is unable to penetrate many of the tightly compacted regions for transcription (Cremer *et al.*, 2001). One of the simplest manners in which the cell is able to overcome this obstacle is to make use of a system that physically relocates the locus of interest from the transcriptionally repressive compartment to one of active transcription.

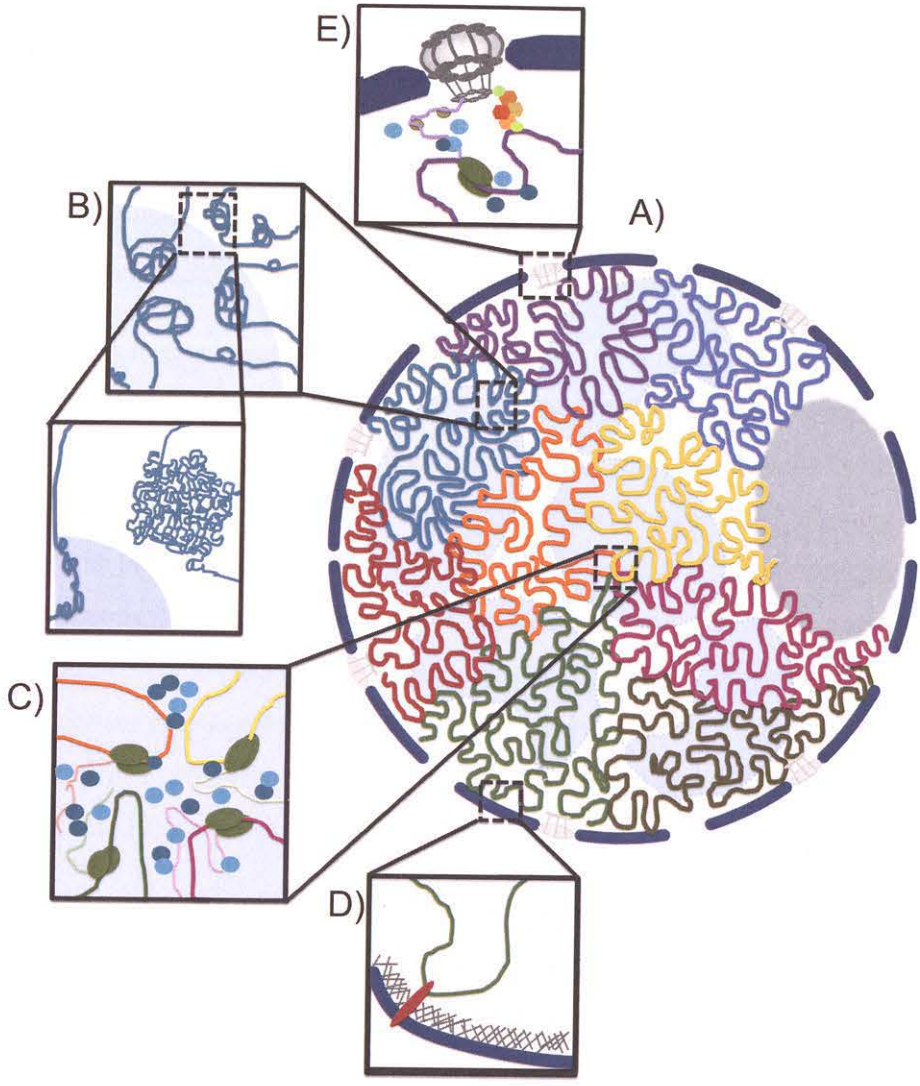

Figure 1.1: Spatial organisation of the genome within the nucleus. A) Each chromosome (different coloured lines) is organised into its own individual chromosome domain within the nucleus (Cremer and Cremer, 2001. Within each domain, chromosomes are partitioned between euchromatic (pale blue background) and heterochromatic (cream background) compartments. Contacts can occur between chromosomes at the edges of domains, or by the formation of chromatin loops to establish long-range interactions. B) Fractal globule model: organisation of chromatin, in which the DNA crumples upon itself to form a "beads-on-a-string" configuration. The globules in turn crumble upon themselves in a series of folding events, until globules consisting of globules of globules are formed (Lieberman-Aiden *et al.*, 2009). C) Transcription factory model: Transcriptionally active loci (coloured curves) are recruited at a transcription centre, with transcription and splicing factors (turquoise circles) and RNAPII (green shapes). RNA transcripts are shown as lighter coloured lines. (Pombo *et al.*, 1999; Osborne *et al.*, 2004) D) Tethering of a heterochromatic chromosome (green) to the nuclear periphery by a transmembrane lamin protein (red) resulting in repression of nearby loci. (Sexton *et al.*, 2007) E) Gene-gating model: A chromosome (dark purple) may interact with the nuclear pore complex (NPC). Tethering to the NPC occurs by NPC-associated factors (yellow and orange shapes). Transcription machinery can be recruited to nearby loci, facilitating transcription and RNA export (light purple), assisted by export factors (brown circles) (Blobel, 1985, Taddei *et al.,* 2004).

This occurs by the de-condensation of the chromatin containing the gene to be transcribed, and its looping out into transcriptionally permissive compartments where it can be more easily accessed by the transcriptional machinery (Schneider and Grosschedl, 2007). Transcriptional activation upon such relocalisation is observed in several genes, including the human major histocompatibility complex (Volpi *et al.*, 2000) and *Drosophila melanogaster* HoxB loci (Chambeyron and Bickmore, 2004).

Several relocalisation events appear to target loci specifically to particular spatial regions or genomic elements, facilitating important interactions between gene loci and specific regulatory molecules or elements, which may positively or negatively influence transcription of genes. For example, a *trans*-enhancer element, the H-enhancer, has been shown to interact with the single active odorant receptor allele in sensory neurons, to regulate the mono-allelic expression of a single gene from the large odorant receptor gene family (Lomvardas *et al.*, 2006). Long-range chromosome interactions also play a role in T-cell differentiation, where transcriptional activation of specific genes on non-homologous chromosomes is dependent on their clustering for co-ordinated expression (Spilianakis *et al.*, 2005).

Evidence from specific mammalian cell types suggests that transcriptional activation may occur upon relocalisation of genes to discrete regions specifically enriched in transcriptional machinery. The detection of large numbers of discrete foci of active transcription (by immunofluorescent (IF) assays of sites of BrUTP incorporation and RNA polymerase II (RNAPII); Pombo *et al.*, 1999; Osborne *et al.*, 2004), and co-localisation of selected active gene loci and transcripts in these foci (by DNA/RNA fluorescent *in situ* hybridisation (FISH) with IF; Osborne *et al.*, 2004), has led to the development of the transcription factory hypothesis. This hypothesis suggests that clusters of RNAPII, presumably with the necessary transcription factors, form sites of concentrated nascent RNA production. These transcription foci may be simultaneously occupied by multiple active gene loci where the genes may be co-regulated (Figure 1.1C) (Osborne *et al.*, 2004). It is thought that these RNAPII clusters are tethered to a stable nuclear structure, allowing them to remain intact even in the absence of transcription. Upon activation, genes are expected to re-localise to these stable clusters, as opposed to the transcription machinery complexes aggregating on activated genes (Mitchell and Fraser, 2008). However, evidence of transcription factories occurring as stable features of nuclear architecture has only

been shown in a limited number of mammalian cell types. Further biochemical and microscopic evidence, from several different cell types and transcriptioinal contexts, is required for more conclusive confirmation of the transcription factory hypothesis.

In addition to specific interactions, the transcriptional activity of a locus may also be dependent on its position within the broader nuclear landscape. Specific regions of the nucleus generally have a well-defined gene activity status. For example, in many cell types the nuclear interior has been observed to be transcriptionally permissive, while the nuclear periphery is generally transcriptionally repressive. This perinuclear silencing arises for several reasons, including the clustering of repressed genes in heterochromatin foci, association with Silent Information Regulator (SIR) histone de-acetylases, as well as tethering to the nuclear periphery via close association of heterochromatin with nuclear lamins (Taddei *et al.*, 2004; Sexton *et al.*, 2007) (Figure 1.1D).

Despite the close association of heterochromatin with the nuclear periphery, this sub-domain is not exclusively repressive. Studies in *Saccharomyces cerevisiae* have shown that association with the nuclear pore complex (NPC) activates gene expression (Taddei *et al.,* 2004), in partial confirmation of the gene-gating hypothesis (Blobel, 1985) (Figure 1.1E). Activated genes have been found tethered to the nuclear pore via the SAGA histone acetyltransferase, which binds to the genes' promoters (Cabal *et al.*, 2006; Sexton *et al.*, 2007). The precise process of activation at the nuclear pore is unclear, but evidence suggests that proteasome regulated histone ubiquitination and subsequent acetylation by SAGA is required for the activation of some NPC tethered genes (Sexton *et al.*, 2007). Some components of the RNA-export machinery have been suggested to be involved in gene expression at the NPC (Sexton *et al.*, 2007; Schneider and Grosschedl, 2007), and proximity to the nuclear pore is thought to facilitate export of the newly synthesised mRNA to the cytoplasm (Blobel, 1985).

1.4. *Plasmodium falciparum* pathogenesis is dependent on highly regulated gene expression.

The protozoan parasite *Plasmodium falciparum*, is the main causative agent of the disease malaria in humans. The parasite has a complex life cycle, occurring in 3 main stages: in the *Anopheles* mosquito vector, in the human liver and in human blood (Figure 1.2). The proliferative intra-erythrocytic stage of the parasite life cycle, during which the parasite undergoes multiple cycles of asexual replication within the host's erythrocytes, is often the most sustained stage of parasite infection, and accounts for the bulk of pathogenesis within the human host.

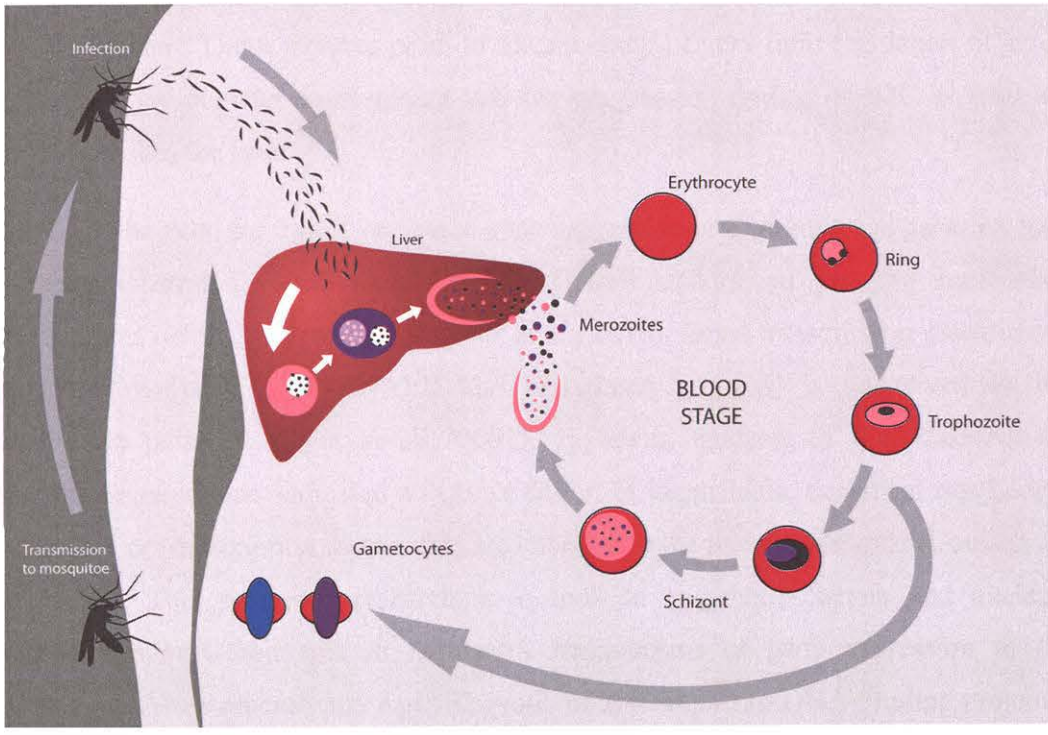

Figure 1.2: Schematic representation of the complete *P. falciparum* life cycle. As a carrier mosquito takes a blood meal infective sporozoites are injected into the human host. They invade host hepatocytes and undergo asexual replication, releasing a large number of merozoites. These merozoites invade host erythrocytes, allowing subsequent asexual replication where merozoites develop into early trophozoites, morphologically described as rings. Trophozoite maturation is followed by multiple rounds of schizogony and nuclear division without cytokinesis, resulting in the formation of schizonts, each containing ~20 merozoites, which invade uninfected erythrocytes upon their release. A small population of erythrocytic parasites develops into gametocytes to be taken up by feeding mosquitoes and sexually replicate in its gut. Released sporozoites migrate to salivary glands to complete the cycle.

Multiple receptor-ligand interactions play an important role in *P. falciparum* invasion of host cells, and are essential for the intra-cellular development and survival of the parasite (Cowman *et al.*, 2000; Tuteja, 2007). Many of the surface receptors presented, as well as other essential processes mediating particularly the intra-erythrocytic developmental cycle (IDC) of the parasite, are dependent on stage-specific gene expression in the parasite. Transcriptome analysis of the various stages of the parasite's IDC has revealed that *P. falciparum* parasites make use of a tightly co-ordinated continuous cascade of gene expression throughout the IDC, expressing genes required for stage-specific functions only at the time at which they are needed (Bozdech *et al.*, 2003). In addition, the parasite makes use of mono-allelic expression for several of its major surface antigens (Ralph *et al.*, 2005), allowing host immune system evasion. These features point to the necessity of very tight regulation of gene expression for parasite development and the progression during its IDC as well as survival within the host.

Although the need for tightly regulated gene expression in *P. falciparum* parasites has been demonstrated, what remain far less well understood are the molecular mechanisms behind this regulation (Volz *et al.*, 2010). Basal transcription machinery, such as involvement of RNAPII and associated proteins, is conserved in *P. falciparum* parasites (Kyes *et al.*, 2007). However, analysis of the *Plasmodium* genome sequence has indicated a distinct deficit of identifiable, canonical regulatory molecules or transcription factors that are encoded in the parasite genome (Coulson *et al.*, 2003). This prompted researchers to look to epigenetic factors and nuclear organisation and their role in regulatory mechanisms of gene expression in *P. falciparum*. More recently the ApiAP2 group of apicomplexan DNA-binding proteins have been identified as putative transcription and regulatory factors in the parasite (De Silva *et al.,* 2008; Flueck *et al.*, 2010). Emerging data of interactions between ApiAP2 factors and chromatin binding and modifying factors point to the intersection of multiple mechanisms of transcriptional regulation within the parasite (Saksouk *et al.*, 2005; Flueck *et al.*, 2010; Merrick and Duraisingh, 2010). Given the clinical relevance of variant antigen expression in establishing persistent infection in the human host, there has been a particular focus on elucidating the transcriptional regulation of these genes. Thus the largest body of evidence for epigenetic regulation relates directly to variant antigen gene expression in the parasite.

1.5. Mono-allelic expression of *var* genes is related to their genomic and sub-nuclear localisation.

The complexity of intersection between epigenetics and nuclear organisation for transcriptional regulation in the *P. falciparum* parasite hint at a role for the spatial regulation of gene transcription in the parasite, similar to that observed in the regulation of HoxB loci (Chambeyron and Bickmore, 2004) and other systems, described above. Thus far, the only observed instance of such spatial transcriptional regulation in the parasite is that of the *var* gene family. These extensively studied genes thus serve as a central model for our understanding of the role of nuclear organisation in gene expression within the parasite. Although much about the mechanisms and pathways facilitating their regulation remain unknown, studies into *var* gene expression have revealed valuable information about both *var* gene regulation and the role of genome organisation in gene expression in the intra-erythrocytic parasite.

The approximately 60-member *var* gene family encodes for PfEMP1 (*P. falciparum*-infected erythrocyte membrane protein 1), a parasite adhesin involved in malaria pathogenesis (Scherf *et al.*, 1998; Kraemer and Smith, 2006). These genes are subject to mono-allelic expression such that only one dominant *var* gene is expressed in a parasite while the others remain transcriptionally silent, accounting for the presentation of only one PfEMP1 variant at a time to the host. As the expressed allele is switched, so the presented antigen variant is switched (Scherf *et al.*, 1998), aiding host immune system evasion.

The majority of *var* genes are located in the sub-telomeric regions of each of the haploid parasite's 14 chromosomes, adjacent to highly conserved telomeric repeats and telomere-associated repetitive elements (Freitas-Junior *et al.*, 2000). This sub-telomeric positioning plays an important role in the constitutive silencing of *var* genes as the parasite chromosome telomeres, including these sub-telomeric variant genes, are packaged into four to five tight heterochromatin-like clusters at the nuclear periphery in intra-erythrocytic parasites (Freitas-Junior *et al.*, 2000). Upon activation, a single sub-telomeric *var* gene has been shown to dissociate from the repressive telomeric clusters and relocalise to a spatially distinct region of the nuclear periphery where transcription is able to take place (Freitas-Junior *et al.*, 2005; Ralph *et al.*,

2005; Lopez-Rubio *et al.*, 2009) (Figure 1.3). Although it is uncertain if this relocalisation is a cause or consequence of transcriptional activation and many aspects of the complex molecular mechanism remain obscure, the peripheral tethering and relocalisation of *var* genes is known to be dependent on conserved genetic elements (Voss *et al.,* 2006; Dzikowski *et al.,* 2006), perinuclear filamentous actin (Zhang *et al.,* 2011), epigenetic histone modifications and chomatin modifying proteins (Mancio-Silva *et al.*, 2008a; Lopez-Rubio *et al.*, 2009; Perez-Toledo *et al.*, 2009).

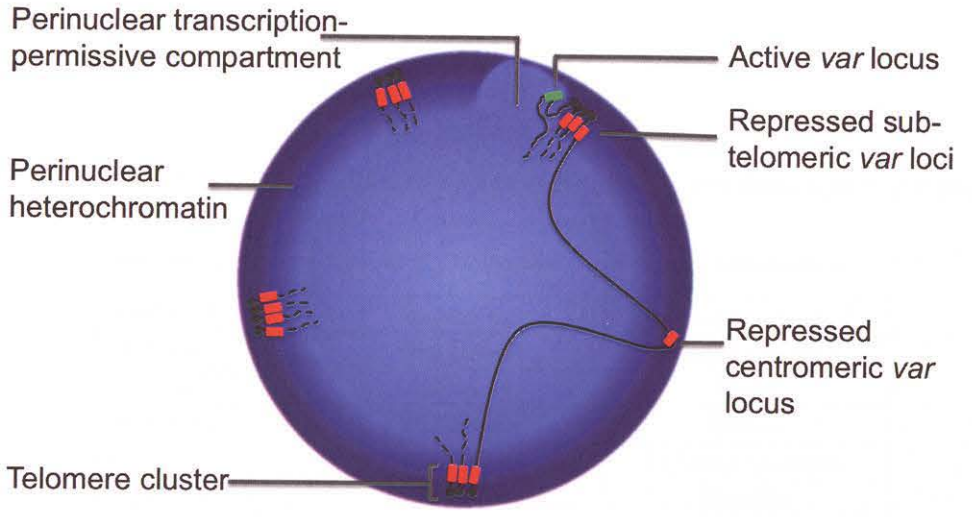

Figure 1.3: Model of spatial organisation of var loci among perinuclear heterochromatin and transcription compartments in the *P. falciparum* nucleus. Sub-teleromeric var loci are shown in telomeric clusters at the nuclear periphery, which consists primarily of heterochromatin. A single transcriptionally active var locus is shown in a distinct perinuclear region of active transcription. Adapted from Lopez-Rubio *et al.* (2009).

1.6. Epigenetic histone modifications function as important factors in *P. falciparum* nuclear organisation and transcriptional regulation.

In conjunction with nuclear spatial organisation, *P. falciparum* parasites depend on histone modifications for the regulation of gene expression (Horrocks *et al.*, 2009). Chromatin immunoprecipitation (ChIP)-based assays have shown tri-methylation of lysine 4 on histone H3 (H3K4me3) and acetylation of lysine 9 on histone H3 (H3K9ac) (marks usually associated with active promoters) to have a broad and dynamic distribution across the *P. falciparum* genome (Table 1.1). These marks are homogenously enriched across the majority of both active and inactive gene regions

in ring-stage parasites, maintaining the bulk of the parasite genome in a euchromatic state (Salcedo-Amaya *et al.*, 2009). In contrast to such a broadly euchromatic genomic landscape, the heterochromatin mark H3K9me3 is limited specifically to chromosome telomeric regions and a few select centromeric regions (Lopez-Rubio *et al.*, 2009). This pattern correlates to the chromosomal distribution of *var* genes and other sub–telomeric variably expressed gene families such as *rif*, *stevor* and *pfmc-2tm* (Salcedo-Amaya *et al.,* 2009; Lopez-Rubio *et al.,* 2009) (Table 1.1). Such H3K9me3 enrichment is distinctly restricted to repressed loci; upon activation, a *var* locus becomes enriched for the active marks H3K9ac and H3K4me3 (Lopez-Rubio *et al.*, 2007; Lopez-Rubio *et al.*, 2009).

Table 1.1: Common histone modifications and their nuclear disribution in *P. falciparum*.

Histone mark	Role in *P. falciparum*	Nuclear distribution
H3K9me3[(1)]	Repressive	Punctate/perinuclear
H4K20me3[(2)]	Repressive	Diffuse/perinuclear
H3K9ac[(1)(3)]	Activating	Diffuse
H3K4me2[(2)]	Activating	Diffuse
H3K4me3[(2)]	Activating	Diffuse/perinuclear
H3K79me3[(2)]	Activating	Irregular

(1) Lopez-Rubio *et al.*, 2009
(2) Issar *et al.*, 2009
(3) Volz *et al.*, 2010

As in other eukaryotic organisms, the *P. falciparum* nucleus appears to be organised into general regions that are permissive or repressive to transcription. Electron microscopy (EM) studies show an electron dense heterochromatic region at the nuclear periphery of ring-stage parasites, broken by one or more perinuclear euchromatic "gaps" (Ralph *et al.*, 2005) (Figure1.4A). These features are consistent with the perinuclear localisation of heterochromatic genes and the transcriptionally permissive zone occupied by actively transcribed *var* loci, respectively (Ralph *et al.*, 2005).

Default silencing of telomeric clusters, as well as other virulence-associated gene regions, has been proposed to occur by their localisation within specific sub-nuclear compartments termed PERCs (perinuclear repressive centers) (Lopez-Rubio *et al.*,

2009) (Figure 1.4A). PERCS would be enriched with gene silencing chromatin binding proteins and modifying enzymes, such as the telomere-associated heterochromatin propagating factors, PfSIR2 (*P. falciparum* silent information regulator 2), PfOrc1 (*P. falciparum* origin-of-recognition complex 1) and PfHP1 (*P. falciparum* heterochromatin protein 1) (Mancio-Silva *et al.*, 2008a; Perez-Toledo *et al.*, 2009). Silenced telomeric and centromeric loci would associate with these compartments by a series of small chromatin loops (Lopez-Rubio *et al.*, 2009).

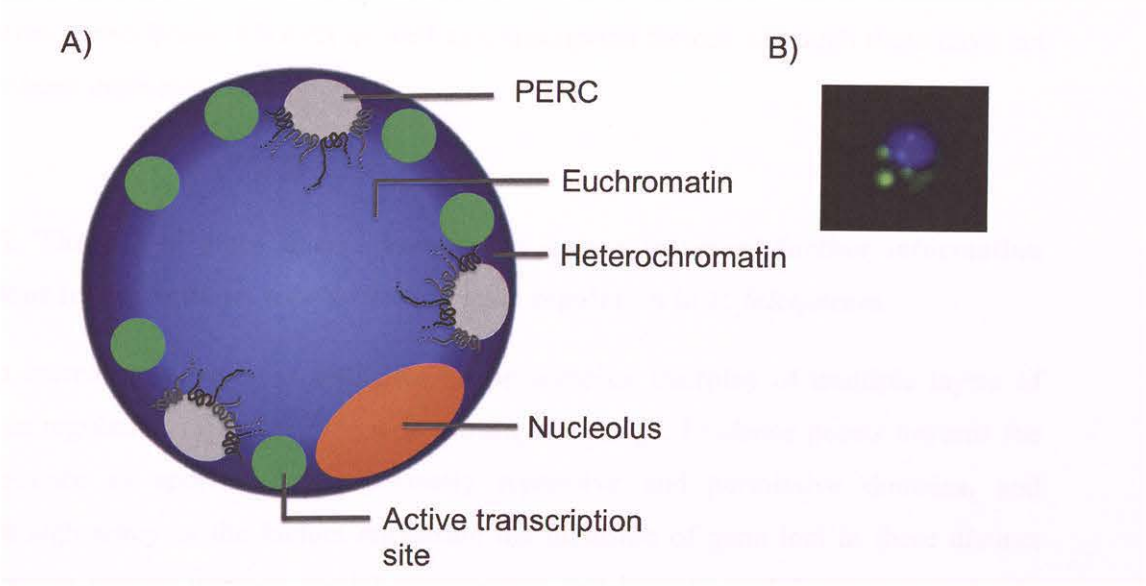

Figure 1.4: Model of spatial organisation of transcription in *P. falciparum*. A) Schematic model showing where sites of active transcription (green) may occur, in relation to perinuclear heterochromatin (dark blue), PERCs (grey) with chromosome loops, and euchromatin (lighter blue). B) BrUTP incorporation labeling (green), in a ring-stage nucleus (labeled with DAPI, blue), showing a limited number of signal foci for active transcription (Modified from Mancio-Silva *et al.*, 2010).

It has been suggested, although not demonstrated, that the perinuclear euchromatic compartment is *var* specific (Dzikowski *et al.*, 2007). Thus, based on the localisation of active histone marks such as H3K4me3 and H3K9ac (Issar *et al.*, 2009), activating proteins such as putative methyl transferases and actively transcribed centromeric loci (Volz *et al.*, 2010) to the central region of the parasite nucleus, this domain was initially thought to house the bulk of transcriptional activity. Recent analysis of spatial organisation of active transcription by IF detection of BrUTP incorporation in *de novo* synthesised RNA revealed a distinct staining pattern of a limited number of spatially distinct perinuclear spots (usually between four and seven in ring-stage nuclei)

(Mancio-Silva *et al.*, 2010) (Figure 1.4B). This indicates that all detected active transcription is in fact restricted to these distinct perinuclear foci (Figure 1.4A). The existence of such transcription foci implies that all actively transcribed genes in the parasite associate with only a limited number of actively transcribing regions, which is in turn suggestive of transcription factory-based gene expression as opposed to a globally transcriptionally active nuclear core region. The spatial organisation of transcription foci in *P. falciparum* parasite nuclei also implies the perinuclear localisation of actively transcribed genes, histone modifications characteristic of active transcription, RNAPII as well as transcription factors, although these have not yet been demonstrated.

1.7. The use of high-content microscopy assays to reveal further information about transcriptional territories and gene regulation in *P. falciparum.*

An increasingly coherent depiction of the complex interplay of multiple layers of gene regulation in *P. falciparum* is starting to emerge. Evidence points towards the existence of specific transcriptionally repressive and permissive domains, and although many of the factors regulating the inclusion of gene loci in these distinct domains remain unclear, spatial organisation and histone modifications are clearly involved. Yet, the interactions between many of these regulatory factors and how they affect each other remain undetermined.

Current models of spatial organisation, which delineate genomic regions of varying states of transcriptional activity into distinct static zones within the nucleus of *P. falciparum,* as described above, may overly simplify the complexity of spatial and epigenetic regulation. These models may fail to account for many of the nuances of transcriptional and spatial regulation within the parasite nucleus, as well as for processes that must occur during the parasite's IDC. Gross nuclear remodeling associated with progression of the parasite through each stage of the IDC, as the nucleus increases in size and undergoes multiple rounds of division, may be expected to occur with a range of nuclear-internal reorganisations. Such changes may account for the known capacity of loci to be actively modified in their epigenetic marks as well as to spatially reposition to different compartments in the nucleus (Ralph *et al.*, 2005; Lopez-Rubio *et al.*, 2009). Finally, this would be consistent with significant

modifications of genomic material within the nucleus, such as the recently observed cell cycle-coupled chromatin dynamics (Weiner *et al.*, 2011). Dynamics in the genomic distribution of histone modifications during the IDC (Salcedo-Amaya *et al.*, 2009) are suggestive of dynamic shifts in the nuclear organisation between the different developmental stages.

The literature to date on *Plasmodium* nuclear architecture provides only a series of snapshots showing limited information regarding the parasite's nucleus. This intimates a stereotyped *P. falciparum* nuclear organisation, which appears static at least within specific IDC stages, such as ring or schizont stages (i.e. Lopez-Rubio *et al.*, 2009; Manci-Silva *et al.*, 2010; Volz *et al.*, 2010). There is an inherent contradiction in such a perspective, as gene expression is an intrinsically dynamic process. The chromatin remodeling (i.e. Salcedo-Almaya *et al.*, 2009, Weiner *et al.*, 2011) and transcription-dependent relocalisation events (Ralph *et al.*, 2005) proposed to play a role in transcriptional regulation imply a constant shifting of both genomic matter as well as chromatin modifying molecules, epigenetic modifications, and various factors involved in the transcription process.

The dearth of information about the spatial organisation of the plasmodial nucleus may be attributed to limitations in the available imaging technology, and thus the approaches used for microscopy-based studies. Current approaches to imaging have several inherent limitations, not least of all the universal resolution limit of light microscopy of approximately 200 nm. This limited resolution can result in the blurring of nuclear sub-compartments resulting in the inability to distinctly localise objects, particulary in a nucleus such as that of *P. falciparum* ring-stage parasites, with a size range of 1-5 μm. In addition, the lack of high-throughput automated imaging of experiments results in relatively small sample sizes of tens to, at best, hundreds of nuclei. Larger sample sizes would allow for statistical analysis of probabilistic nuclear compartmentalisation, as well as the detection of underlying variation in imaging results. This may reveal otherwise overlooked subtleties and dynamics in nuclear organisation. Finally, the often-simplistic imaging data analysis commonly used tends to reduce multi-dimensional information to one-dimensional data-points, thus omitting a large amount of information and possibly underestimating the role of nuclear architecture in gene regulation (Berger *et al.*, 2008).

Berger *et al.* (2008) attempted to overcome these limitations using computational image analysis of large sample sets to construct high-resolution probabilistic maps of gene loci in *Saccharomyces cerevisiae* nuclei. This was achieved by identifying nuclear landmarks, in this case the nuclear envelope, nucleolus and the nuclear centre, with which to construct a three-dimensional co-ordinate system of the nucleus. These landmarks were labeled alongside genes of interest, and thousands of nuclei were imaged for each experiment. Computational analysis tools allowed the extraction of the necessary three-dimensional information out of the images, leading to the construction of high-resolution probabilistic maps of gene loci within the stereotypical symmetrical yeast nucleus (Figure 1.5a). These maps revealed very clearly defined gene territories with a resolution greater than could be obtained by analysing just one or a few nuclei. They also demonstrated very clearly how these gene territories are remodeled upon a change in the transcriptional status of the locus (Figure 1.5b).

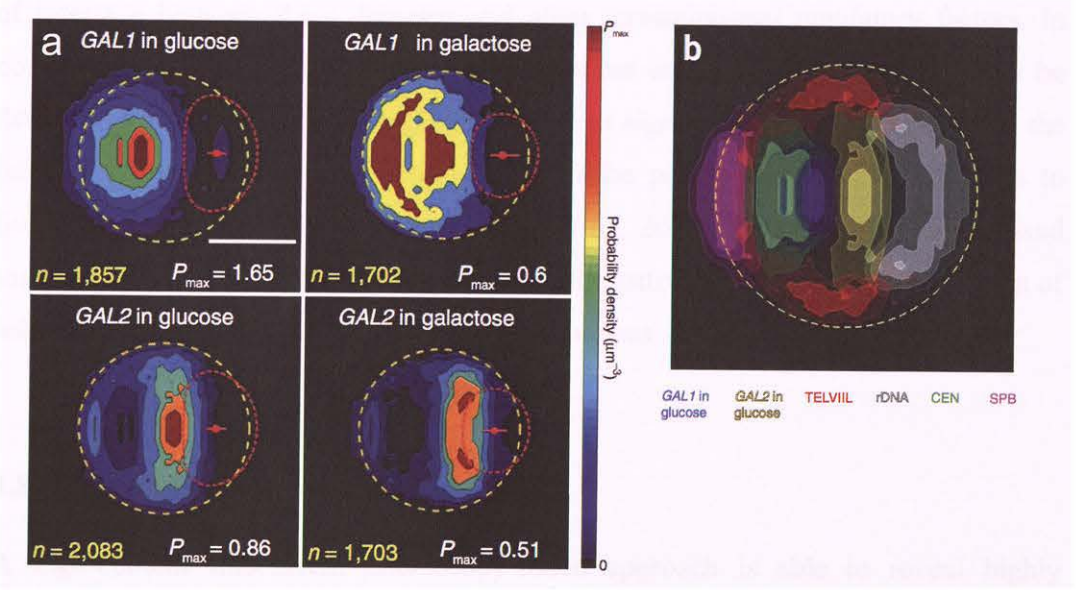

Figure 1.5: Probabilistic maps of gene loci in yeast nuclei. a) Maps of the *GAL1* and *GAL2* loci in yeast in media containing glucose (transcriptionally inactive loci) or galactose (active loci). The yellow dotted circle indicates the nuclear periphery; the red dotted circle indicates the position of the nucleolus. The colour of an area indicates the probability of the locus occurring in that given region (warm colours indicate a higher probability than cooler colours). b) Composite map showing the distinct sub-nuclear territories occupied by the spindle pole body (SPB, purple) and five gene loci: repressed *GAL1* (blue), repressed *GAL2* (yellow), a sub-telomeric locus (TELVIIL, red), a centromeric plasmid (CEN, green), an rDNA locus known to localize with the nucleolus (grey). Map resolution ~150 nm. Modified from Berger *et al.* (2008), with copyright permission from Nature Publishing Group.

In this work, we set out to understand the spatial arrangement of transcriptionally active and repressive regions within the nucleus of *P. falciparum* parasites, in relation to both each other as well as other nuclear factors of interest such as RNA polymerases and transcription factors. Conventional epifluorescent microscopy, as well as a recently developed super-resolution microscopy technique, STORM (stochastic optical reconstruction microscopy) (Rust *et al.,* 2006), was applied to the study of such nuclear organisation within individual parasites. In addition, we sought to investigate the extent to which such spatial organisation may be observed to be variable and dynamic within a single IDC stage, the ring-stage of the parasite by applying a similar strategy to that used by Berger *et al.* (2008). Such an approach was selected based on the expectation that it would provide spatial information on a population scale, giving a broader perspective on the spatial regulation of gene expression in the parasite. In the case of a stereotypical and static parasite nuclear architecture, this approach would allow the establishment of highly resolved and clearly defined domains of transcriptional activity and repression, as well as regions of interface between these domains and other transcriptional regulatory factors. In contrast, if the nuclear organisation features more extensive dynamics, this may be detected by the high-content imaging approach as significant levels of variation in the labeling patterns for target molecules. Given the parasite-specific impediments to live-cell imaging of *P. falciparum* (Wissing *et al.,* 2002), the analysis of large, fixed sample populations offer a suitably sensitive alternative approach for the detection of subtle variation or rearrangements within the nucleus.

1.8. Hypothesis

A high-content fluorescent microscopy-based approach is able to reveal highly resolved spatial information regarding the nuclear organisation of transcriptionally repressive and active domains across the *P. falciparum* ring-stage parasite population.

1.9. Aims

In chapter two, nuclear markers instructive of transcriptional activity and repression in *P. falciparum* were experimentally established for application in fluorescent

microscopy. The assays focused on the establishment and optimisation of a number of fluorescent labeling techniques, including IF and *in situ* hybridisations, in the ring-stage of the intra-erythrocytic parasite.

In chapter three, the spatial organisation and dynamics of markers for transcriptional repression and activity were directly investigated. High-content fluorescent imaging and computational analysis were used to map the nuclear architecture within synchronous *P. falciparum* populations, as well as throughout the ring-stage of the parasite in a time-dependent manner.

1.10. Outputs

- Poster presentation:

  Dynamic localisation of repressive and permissive zones of transcription in the *Plasmodium falciparum* nucleus. Caron Griffiths, Rethabile Kuthlang, Lyn-Marie Birkholtz, Musa M. Mhlanga. SASBMB-FASBMB Congress, KwaZulu-Natal, 29 January- 1 February 2012.

- Review article:

  Henriques R, Griffiths C, Rego EH, Mhlanga MM. 2011. PALM and STORM: unlocking live-cell super-resolution. Biopolymers 95: 322-330

Chapter Two

Establishment and optimisation of labeling techniques for fluorescent microscopy assays in the *P. falciparum* nucleus

2.1. Introduction

Microscopy allows the unique opportunity to directly observe individual cells or micro-organisms and their structures, as well as the spatial arrangements and movements of the molecules and factors within these, that we can otherwise only assess by biochemical measures. Although traditional biochemical approaches may reveal functional information such as chemically interacting factors within a system, the spatial information required for the deciphering of the function and role of nuclear and genomic organisation can only be obtained by visual observation of the system. While various microscopy techniques may be applied to cell biology, fluorescent light microscopy lends itself particularly well to many studies as it allows precise labeling and visualisation of multiple molecules of interest in a single sample, often with non-invasive and non-destructive techniques.

The use of a fluorescent imaging-based approach to studying nuclear organisation of *P. falciparum* is heavily dependent on our ability to specifically and sensitively label the nuclear factors of interest in fixed parasites. In particular, for a high-content approach in which many samples need to be reproducibly labeled with the same targeting molecules and techniques, it is useful to consider the practicalities behind the techniques and well as their repeatability to provide consistent labeling within and between samples. Thus, the establishment of specific, reliable and reproducible fluorescent microscopy assays for the detection of nuclear genomic regions and proteins of interest becomes central to the functioning of a project such as this. Additionally, we sought to adapt each labeling assay for use primarily with ring-stage parasites in this work. This is based on the expectation that this single-nuclear stage would present the simplest model with which to establish a high-content microscopy approach.

Taking a cue from the mapping strategy used by Berger *et al.* (2008), a number of candidate markers for transcriptional domains of repression or activity, as well as

nuclear structures or landmarks, were identified as potential target molecules for use in this study. Antibodies against the nucleolus and nuclear pore complexes were selected for testing with immunofluorescent labeling of these structures. Of particular interest in this project are nuclear target molecules that may reveal information about nuclear regions of transcriptional repression or activation. Histone modifications H3K9me3 and H3K9ac were thus selected, as well characterised markers of transcriptionally repressive and active chromatin, respectively (Lopez-Rubio *et al.*, 2009; Salcedo-Amaya *et al.*, 2009).

Functional markers of sites of active transcription were also identified. Labeling of serine-2-phosphorylated RNAPII (the actively transcribing form of RNAPII), as well as PfMyb2 (a putative transcription and splicing factor) were tested. PfMyb2, a DNA-binding protein related to the plasmodial transcription factor PfMyb1, is thought to be involved in the regulation of genes controlling parasite cell cycle progression, as well as playing a role in RNA splicing (Meyersfeld, 2005; Baker, 2008). The potential role of PfMyb2 in RNA processing suggests that the labeled protein may serve as a prospective indicator of transcriptional activity. In addition, BrUTP incorporation (Mancio-Silva *et al.*, 2010) as well as a technique for single molecule RNA-FISH (smFISH) (Raj *et al.*, 2008) were investigated as potentially suitable techniques for the detection of *de novo* RNA synthesis and nascent RNA transcripts. DNA-FISH labeling of *var* genes, the majority of which are constitutively repressed, was selected as an additional label for regions or clusters exclusive of transcriptional processing. Further, such labeling allows us to relate the labeling patterns of other target molecules to this extensively studied gene family.

Despite the wealth of information that may be provided by high-content fluorescent microscopy, conventional light-based imaging remains hindered by an inherent resolution limit of approximately 200 nm in the lateral plane, based on the diffraction limit of light (Abbe, 1873; Rust *et al.*, 2006). Recent advances in light microscopy have seen the emergence of so-called "super-resolution" techniques, which provide the opportunity to overcome this resolution limit and potentially study the arrangement of molecules of interest at the single molecule level.

Such super-resolution techniques have enjoyed limited application to the study of *P. falciparum* biology thus far. Only 3D structured illumination microscopy has been

employed; for the study of host cell invasion events (Riglar *et al.,* 2011) and parasite protein trafficking (Hanssen *et al.*, 2010). Our understanding of the spatial organisation within the compact *P. falciparum* nucleus would greatly benefit from the ability to resolve individual particles or clusters to less than 100 nm.

We have investigated the application of a more readily available super-resolution technique, STORM (Rust *et al.,* 2006; reviewed in Henriques *et al.,* 2011), for the visualisation of sub-diffraction distribution of target molecules within the nucleus of *P. falciparum.* By making use of a specialised imaging protocol and computational analysis of data to overcome this resolution limit, STORM is able to provide data reconstructions of up to 20 nm lateral resolution. Implementation of STORM imaging in *P. falciparum* would provide an appealing approach for obtaining information regarding the spatial organisation of individual target molecules or clusters of molecules within the parasite nucleus. The high time and computational resource demands of STORM for the acquisition of even a single STORM image renders such an approach unsuitable for the batch processing of large samples. It could, however, be used as a complementary approach to investigate specific spatial arrangements of molecules of interest at higher resolutions.

2.2. Materials and Methods

2.2.1. *P. falciparum in vitro* culturing

P. falciparum parasites (3D7 strain) were cultured based on the method established by Trager and Jensen (1976). The *P. falciparum* culture was maintained in phenol red-free RPMI-1640 liquid medium (Complete culture medium) with 2 mM L-Glutamine (Gibco, Life Technologies, USA), 25 mM HEPES, 22.2 mM glucose, 5% (w/v) Albumax II (Invitrogen, Life Technologies, USA), 24 µg/ml gentamicin (Sigma Aldrich) and 647 µM hypoxanthine (Sigma Aldrich), to which human red blood cells (Type A^+ or AB^+) (RBCs) were added in the culture flask to maintain a final haematocrit of 5%. The culture was kept infused with a gas mixture of 5% CO_2, 5% O_2, 90% N_2 (PureGas, South Africa), and incubated at 37°C.

Culture synchronisation was carried out as per Lambros and Vanderberg, 1979; by centrifuging the culture at 1200*g* for 3 minutes, aspirating the medium, and adding 10 volumes of 5% (w/v) D-sorbitol. The mixture was incubated at 37°C for 10 minutes and centrifuged as above. The supernatant was removed, the pellet resuspended in complete culture medium and transferred to a new culture flask. The flask was suffused with the gas mixture and returned to the incubator.

Parasite IDC progression and parasitaemia were checked by viewing giemsa-stained thin blood smears of cultures by light microscopy. Blood smears were prepared by smearing a small drop of packed RBCs across a glass slide and allowing it to air dry for approximately 1 minute. The slide was then briefly immersed in methanol, followed by immersion in fresh giemsa stain (10% (v/v) giemsa stock (Sigma Aldrich) in 1x PBS) for 5 minutes. The slide was briefly rinsed under running water, blotted dry and allowed to air-dry completely. The slide was viewed with a 100x oil immersion objective on an inverted light microscope (Olympus CKX-41).

2.2.2. Parasite sample fixation

Chemical sample fixation is required to preserve the parasites as they are at that given time, with the same sub-cellular molecular arrangements as exist in a living cell or organism. The RBCs are lysed by saponin treatment in order to release the parasites from the cells, as well as to eliminate a large amount of background fluorescence due to the RBC membrane and haemoglobin. The parasites are fixed using paraformaldehyde (PFA) and glutaraldehyde, which have aldehyde groups that react with amine groups on proteins and nucleic acids, cross-linking cellular components and holding them in place. Fixation is carried out with the parasites in suspension, as this has been found to best preserve nuclear architecture (Mancio-Silva *et al.,* 2008b), perhaps due to gentler mechanical forces and the avoidance of air-drying.

Fixation was optimised for IF and FISH, based on a fixation protocol communicated by personal correspondence with Mancio-Silva in 2009 (Scherf lab, Institut Pasteur, Paris), and a newer protocol published by Contreras-Dominguez *et al.* (2010). The optimised protocol was as follows: A 10-20 ml sample of synchronised *P. falciparum* culture of 5% haematocrit and 5-10% parasitaemia was obtained in a 50 ml tube. The

RBCs were pelleted by centrifugation at 1200*g* for 3 minutes, and resuspended in a large volume (20-30 ml) cold 1x PBS (140 mM NaCl, 2 mM KCl, 10 mM Na_2HPO_4, 1.8 mM KH_2PO_4, pH 7). Saponin (Merck) was added to the culture sample at a final concentration of 0.15% (w/v). The culture sample was incubated on ice for 2 minutes (for trophozoite or schizont parasites) or 10 minutes (for ring-stage parasites). The solution was centrifuged at 1500*g* for 5 minutes at 10°C, and the pellet was washed by resuspension in 1 ml cold PBS and centrifugation at 5300*g* for two minutes. The wash step was repeated twice. The pellet was resuspended in 4% (w/v) PFA with 0.025% (v/v) glutaraldehyde in 1x PBS, and incubated on ice for 30 minutes. Glycine was added to the sample at a final concentration of 0.1% (w/v), followed by a further 5 minutes incubation on ice. The solution was then centrifuged at 5300*g* for 5 minutes. The pellet was resuspended in cold 1x PBS followed by centrifugation at 5300*g* for 5 minutes. The pellet was resuspended in cold 1x PBS and stored at 4°C until used.

2.2.3. Coverslip cleaning

Glass coverslips (0.17 mm thick, Menzel-Gläser, Germany) were cleaned by a combination of solvent wash steps with sonication. Solvents were used to remove residues of any chemicals that may be on the coverslip surface. Subsequent sonication in a reducing agent functions to release small particles of debris from the surface of the glass coverslip, where they may be adhered by ionic interactions to free, negatively charged silicate groups. Such residues and debris may otherwise contribute to autofluorescent non-specific signal in a sample.

Coverslips were rinsed in a series of 100% acetone, 100% methanol and distilled water. This was repeated twice. Coverslips were then placed in 1 M KOH, and sonicated for 45 minutes, followed by sonicating twice in fresh distilled water for 15 minutes each. Coverslips were rinsed twice more in distilled water and then stored in 40% (v/v) ethanol in distilled water at room temperature until use.

2.2.4. Poly-L-lysine coating of coverslips

Coverslips were coated with poly-L-lysine (PLL), which forms a cationic surface charge on the coverslips. Fixed parasites can adhere to this surface by ionic attraction to the negative charge in the samples' cell membrane, increasing retention of sample on the coverslip surface.

Coverslips were coated by inverting them onto a thin film of 0.01% (w/v) PLL (Sigma Aldrich) in 1x PBS, and incubating them as such in a humid chamber for 30 minutes. Coverslips were then rinsed twice with 1x PBS, and used on the same day for fluorescent microscopy experiments.

2.2.5. Immunofluorescence

IF is based on the specific binding of an antibody to the target molecule within the sample. Direct IF labeling involves the detection of the target molecule using a primary antibody that is directly conjugated to a fluorophore itself. More commonly, indirect IF detection makes use of a fluorescently labeled secondary antibody to target and label the bound primary antibody. Secondary antibodies that recognize peptides or immunoglobulins from a specific species are used. Thus indirect IF makes use of specific antibody pairs: a primary antibody against the target molecule of interest and a secondary antibody against immunoglobulins from the host animal in which the primary antibody is raised. Table 2.1 provides information on each of the primary antibodies used to detect nuclear targets of interest (H3K9me3, H3K9ac, PfMyb2, RNAPII, PfNup1 and the nucleolar component fibrillarin). A number of broadly cross-reactive anti-fibrillarin antibodies were used to test the ability of each to cross-react with plasmodial fibrillarin as a label for the nucleolus.

Indirect IF was optimised based on a protocol published by Mancio-Silva *et al.* (2008a) and carried out as follows: Fixed parasites (50-100 µl), prepared as in section 2.2.2, were deposited onto cleaned, PLL-coated coverslips (prepared as per sections 2.2.3 and 2.2.4) and allowed to settle for 30 minutes to one hour to form a dispersed monolayer of parasites on the coverslip. Samples on the coverslips were rinsed with PBS and incubated with 1% bovine serum antigen (BSA) in 1x PBS for 20 minutes at room temperature to block non-specific antibody binding.

Table 2.1: Primary antibodies and corresponding secondary antibodies used in IF labeling of nuclear targets. Primary antibody and appropriate secondary antibodies for detection of indicated primary antibody are listed next to each other.

Primary Antibodies					**Secondary Antibodies**[4]		
Antigen	**Host**	**Reactivity**	**Supplier**	**Dil. used**[3]	**Host**	**Reactivity**	**Label**
H3K9me3	Rabbit	Broad cross-reactivity	Millipore	1:500	Goat Goat Goat	Rabbit IgG[§] Rabbit IgG Rabbit IgG	AlexaFluor 532 ATTO488 ATTO647N
H3K9ac	Rabbit	Broad cross-reactivity	Millipore	1:2000	Goat Goat Goat	Rabbit IgG[§] Rabbit IgG Rabbit IgG	AlexaFluor 532 ATTO488 ATTO647N
RNAPII	Rabbit	Broad cross-reactivity	Cell Signalling	1:50	Goat Goat Goat	Rabbit IgG Rabbit IgG Rabbit IgG	ATTO647N ATTO488 ATTO647N
H3K9me3	Mouse	Broad cross-reactivity	Abcam	1:100	Goat	Mouse IgG	ATTO488
H3K9ac	Mouse	Broad cross-reactivity	Sigma Aldrich	1:750	Goat	Mouse IgG	ATTO488
BrdU	Mouse	Broad cross-reactivity	Santa Cruz	1:100	Goat Goat	Mouse IgG Mouse IgG	ATTO488 ATTO565
Yeast fibrillarin (38F3)	Mouse	Broad cross-reactivity	Abcam	1:100	Goat Goat	Mouse IgG Mouse IgG	ATTO488 ATTO565
Yeast fibrillarin (6H4)	Mouse	Broad cross-reactivity	Santa Cruz	1:50	Goat Goat	Mouse IgG Mouse IgG	ATTO488 ATTO565
Human fibrillarin (M-A1)	Mouse	Broad cross-reactivity	Thermo Scientific	1:100	Goat Goat	Mouse IgG Mouse IgG	ATTO488 ATTO565
Human fibrillarin (A-16)	Goat	Broad cross-reactivity	Santa Cruz	1:50	Rabbit	Goat IgG	ATTO488
PfMyb2	Chicken	*P. falciparum*	Non-commercial[1]	1:100	Rabbit Rabbit Rabbit	Chicken IgY Chicken IgY Chicken IgY	TMR FITC Biotin
PfNup1	Rat	*P. falciparum*	Non-commercial[2]	1:100	Goat	Rat IgG	CY5

(1) Coetzer lab, University of Witwatersrand
(2) Scherf lab, Institut Pasteur, Paris
(3) Dil. Used: Dilution used.
(4) Each secondary antibody was used at 1:500 dilution. Secondary antibodies denoted by (§) were supplied by Invitrogen; all other secondary antibodies were supplied by Rockland.

BSA-blocked samples were then incubated with the appropriate concentration of primary antibody (as given in Table 2.1) in 1% BSA in 1x PBS, in a humid chamber at 37°C for 45 minutes, followed by three washes with 1x PBS. Coverslips with samples were incubated with the appropriate fluorophore- or biotin-conjugated secondary antibody (as given in Table 2.1), at the suitable dilution in 1% BSA in 1x PBS, in a humid chamber at 37°C for 45 minutes. Samples were washed three times in 1x PBS. Coverslips with samples labeled with fluorophore-conjugated secondary antibodies were mounted on slides with Vectashield mounting medium containing 1.5 µg/ml DAPI (Vector Laboratories). Samples labeled with biotinylated secondary antibodies were incubated in 1% BSA in 1x PBS for 20 minutes, followed by a 45 minute incubation with 0.05 mg/ml streptavidin-conjugated fluorophore (either ATTO488 or ATTO674N) (Atto-Tec, Germany) at room temperature. These samples were then washed three times with 1x PBS at room temperature and coverslips were mounted in Vectashield mounting medium with 1.5 µg/ml DAPI, as above.

A range of different fluorophores were used in IF and other fluorescent assays (Table 2.2). Fluorophores were selected based on suitability of the excitation and emission properties of the dye as well as dye availability. When multiple labels are used, the selection of fluorophores with spectrally distinct excitation and emission wavelengths ensures the ability to distinguish between labels.

Table 2.2: Fluorophores used in IF and other fluorescent labeling assays.

Fluorophore	UV-*vis* spectrum colour	Excitation wavelength (nm)	Emission wavelength (nm)
DAPI	Blue	350	470
ATTO488	Green	501	523
ATTO495	Green	495	527
FITC	Green	490	525
AlexaFluor532	Orange	532	554
AlexaFluor594	Orange	590	617
ATTO565	Orange	563	624
TMR	Orange	557	576
CY3	Orange	550	570
FluoProbe647H	Red	653	675
ATTO647	Red	645	669
ATTO647N	Red	644	669
CY5	Red	650	670

2.2.6. Conjugation of fluorescent dyes to antibodies

Indirect IF labeling allows simple, sensitive detection of molecules of interest. However, the necessity for two antibodies per target molecule is limiting when IF against multiple targets is carried out, particularly in the case of the labeling of two targets with primary antibodies that were raised in the same species. This limitation may be overcome by the conjugation of primary antibodies to spectrally distinct fluorophores, which may then be used in direct IF detection. To this end, selected primary antibodies were used in conjugation reactions with fluorescent dyes using Lightning Link conjugation kits (Innova Biosciences) (described below).

2.2.6.1. Antibody purification

Prior to antibody-fluorophore conjugation, if an antibody is supplied in serum it should be purified to remove free serum proteins and other small molecules, which may also be subject to the conjugation reaction. These molecules can limit labeled antibody yield and interfere with downstream IF assays with the antibody. Purification was carried out using the AbSelect Antibody Purification System (Innova Biosciences). This proprietary system makes use of the high affinity of protein A for IgG molecules from a wide range of host animals. The antibody is bound to protein A immobilised on resin in a centrifuge column, allowing the contaminating proteins and molecules to be washed off the antibody and resin, after which the antibody is eluted and neutralised using proprietary reagents. The purification procedure was performed with 130 µl rabbit-anti-H3K9ac stock solution in serum (Millipore), as per the kit-issued instructions. Specificity and sensitivity of the purified antibody for its target were evaluated by indirect IF (as in section 2.2.5), using titrated purified rabbit-anti-H3K9me3 antibody (1:50, 1:100 and 1:500 dilutions), and goat-anti-rabbit-AlexaFluor532.

2.2.6.2. Antibody buffer exchange

If an antibody is supplied in amine-containing buffers, such as azide and tris, it is not suitable to be used directly in antibody-fluorophore conjugation reactions using the

Lightning Link system. The contaminating amine-molecules, which can interfere with the antibody-labeling reaction, should first be removed or greatly reduced in concentration. This was achieved using the Antibody Concentration and Clean-up Kit (Innova Biosciences), a proprietary system that makes use of centrifugation columns packed with matrices with very small pores. The pores allow small contaminating molecules to pass through the column, while larger proteins such as the antibody are retained on the matrix. Thus an antibody buffer exchange can take place by a series of centrifugation steps in which the antibody is repeatedly concentrated into a small volume of old buffer on the matrix and then diluted into a larger volume with a new proprietary buffer suitable for use with downstream conjugation reactions. Such centrifugation steps are repeated until only a very small proportion of the old buffer, with few contaminating molecules, remains in the antibody solution. The buffer exchange procedure was carried out using 80 µl rabbit-anti-H3K9me3 stock in tris buffer (Millipore), as per the kit-issued instructions. Specificity and sensitivity of the purified antibody for its target were evaluated by indirect IF (as in section 2.2.5), using titrated purified rabbit-anti-H3K9ac antibody (1:50, 1:100 and 1:500 dilutions), and goat-anti-rabbit conjugated to AlexaFluor532.

2.2.6.3. Antibody-dye conjugation

Both purified and unpurified rabbit-anti-H3K9me3 (Millipore) and rabbit-anti-H3K9ac (Millipore) antibodies, as well as unpurified goat-anti-fibrillarin (A-16) (Santa Cruz) and chicken-anti-PfMyb2 (Coetzer lab, University of Witwatersrand) antibodies (listed in Table 2.1) were conjugated with fluorescent dyes using Lightning Link conjugation kits (Innova Biosciences). These kits make of use proprietary reagents that react with amide groups on the proteins to form a covalent bond with the fluorophores. A 40-100 µl volume solution, containing 50-200 µg of antibody to be labeled, was used in each conjugation reaction, as per the kit-issued instructions. Separate samples of each antibody were conjugated to either of the two fluorophores ATTO488 and FluoProbe647H. Labeled antibodies were stored in the dark at 4°C.

2.2.6.4. IF using fluorescently labeled primary antibodies

Direct IF with fluorophore-labeled primary antibodies was carried out as in section 2.2.5, with the difference that, following sample incubation with the primary antibody samples were washed three times in 1x PBS and mounted directly using Vectashield with 1.5 µg/ml DAPI.

2.2.7. BrUTP incorporation

BrUTP incorporation was carried out as previously described (Mancio-Sliva *et al.*, 2010). A 10 ml ring-stage *P. falciparum* culture of ~10% parasitaemia and 5% haematocrit was used. The infected RBCs (iRBC) were pelleted by centrifugation at 1200*g* for 3 minutes, and then resuspended in 8 ml complete culture medium containing 5 U/ml RiboLock RNase inhibitor (Fermentas, USA), prewarmed to 37°C, followed by incubation at 37°C for 5 minutes. The iRBC's were pelleted as above, and resuspended in 15 ml complete culture medium with 5 U/ml RNase inhibitor (37°C). Saponin was added to a final concentration of 0.1%, and the sample was incubated at 37°C for 5 minutes, in order to lyse the parasites from the RBCs. The released parasites were pelleted by centrifugation at 1500*g* for 5 minutes. The pellet was resuspended in 4 ml complete culture medium with 10 U/ml RNase inhibitor, and transferred to 2 ml microcentrifuge tubes. The parasites were pelleted by centrifugation at 5300*g* for 1 minute, and the pellets were resuspended and combined in 1 ml transcription buffer (50 mM HEPES, 100 mM KCl, 5 mM $MgCl_2$, 0.5 mM EGTA, 0.5 mM PMSF, 5 mM DTT, 100 U/ml RNase inhibitor, 2 mM ATP, 1 mM CTP, 1 mM GTP and 0.01 mM BrUTP). The parasites were then incubated at 37°C for 20 minutes to allow transcription to occur. The parasites were pelleted by centrifugation at 5300*g* for 1 minute and the pellet was washed in 1x PBS (room temperature), centrifuged as above, and resuspended in cold (4°C) 4% PFA in 1x PBS. This suspension was incubated on ice for 20 minutes to fix the parasites. The parasites were pelleted again by centrifugation at 5300*g* for 5 minutes, washed in cold PBS, centrifuged at 5300xg for 5 minutes, and resuspended in cold 1x PBS.

Following BrUTP incorporation and fixation, the fixed parasites were deposited onto clean coverslips and allowed to settle for 30 minutes to 1 hour before the coverslips

were washed once in 1x PBS. IF was carried out with these coverslips, as described in section 2.2.5, using a mouse-anti-BrdU primary antibody (Santa Cruz, USA) at a 1:100 dilution in 1% BSA in 1x PBS, and a rabbit-anti-mouse ATTO565 or ATTO488 labeled secondary antibody; 1:500 in 1% BSA in 1x PBS.

2.2.8. DNA-probe synthesis for use in DNA-FISH

DNA-FISH labeling of *var* genes was based on the method used by Lopez-Rubio *et al.* (2009). This allows generic labeling of the bulk of the *var* gene family by using a mixture of probes targeting the conserved exon 2 regions, *var* Exon2A, B and C, as well as a probe specifically targeting the *var*2CSA locus. DNA-FISH makes use of large (1-2kb) DNA probes, labeled multiple times with a fluorophore for detection. The probes are synthesised by PCR amplification, firstly of the probe region off genomic DNA (gDNA), in order to generate templates for further PCR amplification. In a second round of amplification, chemically modified dNTPs, such as biotinylated dUTP, are included in the reaction, to be incorporated into the elongation product. These products are used as probes in the FISH protocol. Following hybridisation, streptavidin-conjugated fluorophores are added to bind to the biotin groups in the FISH-probes, allowing fluorescent localisation of the hybridised probes.

2.2.8.1. Genomic DNA extraction

A 10 ml trophozoite/schizont stage *P. falciparum* parasite culture of ~10% parasitaemia, 5% haematocrit, was used as starting culture. The RBCs were pelleted by centrifugation at 800*g* for 5 minutes. The pellet was resuspended in 5 volumes ice-cold PBS with 0.1% saponin, and incubated on ice for 10 minutes. The parasites were pelleted by centrifugation at 1500*g* for 5 minutes. The supernatant was discarded and the pellet was washed twice in 1x PBS before being resuspended in 300 µl TE buffer (10 mM Tris-Cl, 1 mM EDTA) containing 200 µg/ml proteinase K and 3% SDS. The solution was carefully mixed and incubated at 65°C for 1-2 hours, with occasional mixing and maceration. One volume each of phenol and chloroform was added and the solution was mixed by inversion for 10 minutes. The aqueous and organic phases were separated by centrifugation at 15000*g* for 10 minutes. The upper aqueous layer

was removed to a new tube, to which another 1 volume of chloroform was added and mixed for another 10 minutes. The tube was then centrifuged at 15000*g* for 10 minutes and the aqueous phase was transferred to a new tube. One volume of chloroform was added, mixed for 5 minutes and centrifuged at 15000*g* for 5 minutes before the aqueous phase was transferred to a new tube. Sodium acetate, pH 4.5, was added to a final concentration of 0.3 M, followed by 2.5 volumes cold 99% ethanol, and the solution was mixed thoroughly. The solution was stored at -20°C for 1 hour and then centrifuged for 15000*g* for 10 minutes. The supernatant was discarded and the pellet air-dried. The pellet was resuspended in 100 µl TE, and the concentration of the gDNA was monitored spectrophotometrically at 260 nm, using a Nanodrop (Thermo Scientific). The quality of the gDNA was checked by analysis on a 0.5% agarose gel. The gDNA was stored at -20°C.

2.2.8.2. PCR amplification of DNA-FISH probe sequences

PCR was carried out using the extracted gDNA as template, using the primers given in Table 2.3 (as listed in Lopez-Rubio *et al.*, 2009).

Table 2.3: Primer sequences used for the PCR amplification of regions of *var* exon2 loci from *P. falciparum* gDNA.

Locus	Forward primer sequence	Tm* (°C)	Reverse primer sequence	Product (bp)	Tm* (°C)
Exon 2A	5'-ATTCCATACATCCGATATAGG-3'	54	5'-CCGAAATCACCTGTTGACCTC-3'	1185	54
Exon 2B	5'-TATAGGATATTTCTCTTTCACC-3'	53	5'-AAAACTAAAAGCCCTGTGGACC-3'	1260	58
Exon 2C	5'-AGGGTTGTGGTGGTTATAGG-3'	57	5'-AAAACCAAAGCATCTGTTGG-3'	1272	53
*Var*2 CSA	5'-AGCTGATCCTAGTGAAGTGG-3'	57	5'-TGAAGTATCTTGTTCAGCGG-3'	2000	55

*Melting temperature =69.3+0.41(%GC)-650/N where N=length of oligonucleotide (Rychlik *et al.*, 1990).

PCR reaction mixtures for amplification of each locus were prepared by mixing the appropriate forward and reverse primers (0.2 µM each) with 5x Crimson Taq Buffer

(New England Biosciences) to a 1x final concentration, 200 µM dNTPs, 200 ng gDNA template and 2.5 U Crimson Taq Polymerase (New England Biosciences), to a final volume of 50 µl. Optimisation of the thermal cycling profile for a PCR reaction was carried out in terms of the annealing and extension temperatures. The reaction mixture was used with the following final protocol in a GS1 Thermal Cycler (G-Storm, UK): an initial denaturation step at 95°C for 30 seconds, followed by 40 cycles of denaturation at 95°C for 30 seconds, annealing at 50°C for 1 minute, and product extension at 64°C for 1 minute 20 seconds. Following a final extension step of 5 minutes at 64°C, the reaction mixture was kept at 4°C.

Following amplification, the PCR products were separated and analysed by agarose gel electrophoresis, using a 0.8% (w/v) agarose gel with 15 V/cm. Generuler® DNA ladder mix (100-10000 bp) (Fermentas, Thermo Scientific, USA) was used as a moleculer marker. DNA was visualized by ethidium bromide staining, and illumination with UV light in a G:Box Gel Documentation and Analysis system (Syngene, UK). Each DNA band of interest was excised from the gel and the DNA product was purified from the agarose gel using a commercial gel purification kit, NucleoSpin® Gel and PCR cleanup (Macherey-Nagel), as per manufacturer's specifications. Following heating of the agarose gel fragment to dissolve the gel, the kit makes use of a silica gel in a centrifugation colmn, to which the DNA in the sample binds in the presence of chaotropic salt. Following a series of wash steps in a proprietary ethanolic buffer, the purified DNA is eluted in a proprietary low-salt buffer.

2.2.8.3. DNA-FISH probe biotinylation

Following DNA-FISH probe amplification and purification, the double-stranded DNA products were biotinylated. A commercial DNA labeling kit, the Biotin DecaLabel DNA labeling kit (Fermentas, Thermo Scientific, USA), was used, which incorporates biotinylated-dUTPs into new strands as they are synthesised. The kit makes use of a random-primed labeling method in which decameric primers of random sequences are able to anneal to the DNA probe strands, allowing Klenow fragment polymerase to extend the probe sequence along the DNA template, creating a new strand. Because a

portion of the dNTPs in the reaction is biotin-11-dUTP, these modified bases are incorporated into the new DNA strand, creating new biotinylated DNA-FISH probes. The biotinylation reaction was carried out as per the kit-issued instructions, using 1 μg DNA template.

Confirmation of the biotinylation reaction as well as quantification of the yield of biotinylated-probe was carried out using a commercial Biotin Chromogenic Detection kit (Fermentas, Thermo Scientific, USA). This kit makes use of the chromogenic reaction of BCIP-T (5-bromo-4-chloro-3-indolyl phosphate, *p*-toluidine salt) with alkaline phosphatase. The enzyme cleaves the BCIP-T substrate, producing an insoluble blue precipitate. A dot blot assay is used, in which the biotinylated probe-target dsDNA hybrid molecules are immobilised on a positively charged nylon membrane. Streptavidin-conjugated alkaline phosphatase binds to the biotin in the probes. The membrane can be soaked in a solution of BCIP-T, producing a clearly defined coloured spot, amplified in strength in the presence of the chromogen enhancer NBT (nitro blue tetrazolium).

A range of dilutions, from 1:10 to 1:1 000 000, of the purified biotinylation reaction product were prepared, and each dilution was spotted onto a nylon membrane strip and allowed to air dry. In addition, a series of dilutions of a control solution of biotinylated-DNA of known concentration, ranging from 500 pg to 5 fg, were blotted onto the membrane. The probes and control DNA were cross-linked to the membrane by illumination with UV light for 2-3 minutes. Detection of the biotinylated-DNA was then carried out, using proprietary buffers included in the detection kit, as per the manufacturer's instructions.

Quantification of the biotinylation reaction yield was achieved by densiometric analysis, using ImageJ open source image analysis software (NIH, USA). The approximate biotinylated-DNA probe concentrations were calculated by comparing signal density from the blots of the most dilute probe solutions detectable above background, to that of the 500fg standard.

2.2.9. DNA-FISH

DNA-FISH was initially carried out as published by Ralph *et al.*, 2005, using parasites fixed as described in section 2.2.2. A dispersed layer of fixed parasites was deposited onto each PLL-coated coverslip (prepared as in sections 2.2.3 and 2.2.4) and allowed to settle for 30 minutes to an hour. Deposited parasites were rinsed in PBS and then incubated with 0.1% (w/v) Triton X-100 for 5 minutes before being washed twice more in 1x PBS. Biotinylated dsDNA FISH probe (50 ng) was added to 15 µl hybridisation buffer (50% (v/v) deionised formamide (Ambion, Life Technologies, USA), 10% (w/v) dextran sulphate, 1x SSC (150 mM NaCl, 15 mM sodium citrate)), and denatured by heating at 95°C for 5 minutes, followed by rapid cooling to 4°C in an ice slurry for 5 minutes. Coverslips with parasites were inverted onto the hybridisation solution on an inert glass surface, and heated at 92°C for 3 minutes, before being incubated in a moist chamber at 37°C overnight. Coverslips were lifted from the glass surface by floating them on ~50µl wash buffer (50% formamide, 2x SSC), preheated to 37°C. The coverslips were then washed twice in wash buffer at 50°C for 30 minutes, twice in 2x SSC at 37°C for 30 minutes, and once in 4x SSC for 30 minutes at room temperature. The coverslips were then rinsed briefly in 1x PBS and incubated in 1% BSA in 1x PBS for 20 minutes. Coverslips were then inverted on 10 µl droplets of 20 ng/ml streptavidin-conjugated ATTO565 or ATTO647N, and incubated in a moist chamber at room temperature for 40 minutes. Following this, coverslips were washed three times in PBS with agitation, then mounted on a slide with Vectashield mounting medium containing 1.5 µg/ml DAPI (Vector Laboratories).

Following optimisation experiments, the determined DNA-FISH protocol performed was in accordance with Mancio-Silva *et al.* (2008b). This protocol differs from that given above in the hybridisation conditions, as well as the wash steps. Hybridisation was carried out using 100 ng FISH probe, in a hybridisation buffer consisting of 50% (v/v) formamide, 10% (w/v) dextran sulphate and 2x SSPE (150 mM NaCl, 10 mM NaH_2PO_4, 1mM EDTA). Following addition of the hybridisation solution to the sample, the sample was heated to 80°C for 30 minutes, and then incubated at 37°C overnight in a humid chamber. Following hybridisation, the sample was washed once in wash buffer, at 37°C for 30 minutes, once in 1x SSC at 50°C for 10 minutes, once in 2x SSC at 50°C for 10 minutes and once in 4x SSC at 50°C for 10 minutes. The

samples were then rinsed once in PBS at room temperature, and blocked and labeled with streptavidin-conjugated dye as above, before mounting in Vectashield with 1.5 µg/ml DAPI.

2.2.10. smFISH

smFISH makes use of a large number (up to 48) of oligonucleotide probes targeting sequences arrayed along the length of an mRNA molecule. Each 20 nucleotide-long probe is conjugated to a single fluorophore, such that the binding of many probes to a single mRNA molecule will render it detectable by fluorescent microscopy.

2.2.10.1 smFISH probe preparation

smFISH probes were designed using the smFISH probe algorithm available on the smFISH website: singlemoleculefish.com. Gene sequences for the target genes coding for CTP synthetase (CTPSyn; PF14_0100), adenyl succinate synthetase (AdSucSyn; PF13_0287) and inosine monophosphate dehydrogenase (IMP-DHG; PFI1020c) were used as input for the algorithm, which generated 48 distinct 20 nucleotide-long sequences for each target gene. These oligonucleotides were synthesised by BioSearch Technologies (USA) with a 3' amino group modification.

Conjugation of the oligonucleotide probes to fluorophores occured between the 3' amino group on the oligonucleotides and the NHS-ester group on the fluorophores by an esterification reaction. Pellets of each of the 48 oligonucleotides per target gene were resuspended in 100 µl Tris-EDTA (TE) buffer. Each oligonucleotide solution (10 µl) for a target gene was pooled together, and the concentration of DNA of each probe mixture was measured spectrophotometrically at 260 nm, using a Nanodrop. The oligonucleotides were precipitated by the addition of sodium acetate to 0.3 M, vortexing, and the addition of 1.5 volumes ice-cold 100% ethanol, followed by further vortexing. The mixture was incubated at -20°C overnight, then centrifuged at 18000*g* for 20 minutes. The supernatant was removed and the pellet was resuspended in 200 µl fresh 0.1 M sodium tetraborate. The DNA concentration of the probe solution was determined spectrophotometrically at 260 nm, using a Nanodrop. Approximately 0.2

mg of dye to be used (either ATTO495-NHS ester or ATTO647N-NHS ester) was dissolved in 10 µl anhydrous DMSO, and then added to 200 µl 0.1 M sodium tetraborate. This dye solution was added to the probe solution, vortexed, and incubate at 37°C overnight. The oligonucleotides were precipitated as above. The solution was centrifuged at 18000*g* for 20 minutes and the supernatant was removed. The pellet was washed in 70% ethanol, air-dried and resuspended in 200 µl 0.1 M triethyl ammonium acetate (HPLC buffer A). The DNA concentration of the probe solution was again determined spectrophotometrically before purifying the dye-conjugated oligonucleotides. Purification was carried out by HPLC with a C18 column and a gradient of 2-98% HPLC buffer B (10% acetonitrile in 0.1 M triethyl ammonium acetate) in HPLC buffer A over 25 minutes (ATTO647N labeled-probes) or 60 minutes (ATTO 495 labeled-probes). Collected dye-conjugated oligonulceotide fractions were dried *in vacuo*. The probe pellets were resuspened in 100 µl TE buffer, and the DNA concentration was measured spectrophotometrically. Labeled probes were stored at -20°C until use.

2.2.10.2. smFISH hybridisation

smFISH was initially carried out as adapted from Raj *et al.* (2008) and Mancio-Silva *et al.* (2008b). Probes against the ring-stage expressed transcripts prepared in section 2.2.10.1, as well as probes recognising transcripts of trophozoite-expressed genes rhoptry associated proteins 1 and 3 (RAP1; Pf14_0102 and RAP3; PFE0075c), rhoptry associated merozoite antigen (RAMA; MAL7P1.208) and merozoite surface protein 1 (MSP1; PFI1475w) were used for smFISH. The trophozoite-stage tasncript probes were already available for use, having been previously conjugated to AlexaFluor594, CY3 or CY5 fluorophores by Catherine Gouyette (Institut Pasteur, Paris).

A dispersed layer of fixed parasites was deposited onto a glass coverslip, prepared as in sections 2.2.3 and 2.2.4. The coverslip was washed in 1x PBS and incubated in 0.1% (w/v) Triton X-100 for 5 minutes before being washed twice with 1x PBS. Fluorophore conjugated probe (20-30 ng) to be used was added to 20 µl of hybridisation buffer (50% (v/v) deionised formamide, 10% (w/v) dextran sulphate, 300 mM NaCl, 20 mM NaH_2PO_4, 2 mM EDTA, 2mM vanadyl ribonucleoside

complex (Sigma Aldrich), 250 µg/ml *E. coli* tRNA (Sigma Aldrich)). The solution was pipetted onto parafilm on a flat surface, and the parasite-coated coverslips were inverted onto the hybridisation buffer and incubated overnight at 37°C in a moist chamber.

After overnight incubation, the coverslips were lifted from the parafilm and the hybridisation buffer was aspirated. The coverslips were incubated in wash buffer (50% (v/v) formamide in 2x SSC) at 30°C for 30 minutes, followed by a second incubation in fresh wash buffer at 30°C for 30 minutes, a 10 minute incubation in 4x SSC at 30°C, and 10 minutes incubation in 2x SSC at 30°C. The coverslip was then washed in 1x PBS and mounted on a slide with Vectashield mounting medium containing 1.5 µg/ml DAPI.

During further optimisation, the following changes were made to the protocol: the formamide content of the hybridisation and wash buffer was changed to 10% (v/v) and wash steps were changed to two 30 minute incubations in wash buffer at 37°C followed by two washes in 1x PBS and mounting in Vectashield with DAPI.

2.2.12. Epifluorescent Microscopy

Imaging was carried out using a Nikon Eclipse Ti inverted fluorescent microscope, with a 100x, 1.49 numerical aperture (NA) oil immersion objective. Images were captured using the Andor 897 iXion EMCCD camera (Andor, Belfast, UK). The microscope was controlled using µManager open source microscope management software (UCSF and NIH, USA). Exposure times for DAPI signal was kept at 50 milliseconds, and ranged between 200 milliseconds and 1.5 seconds for other signals.

2.2.13. Image processing

Image processing and manual inspection was carried out in ImageJ open source image software (NIH, USA). A single 2D image of z-section stacks was produced by maximum intensity projection. This projects the brightest pixel value of each position throughout the z-stack onto a single composite image. This was followed by background subtraction and contrast adjustment. Pseudo-colours were applied to the

different channels (Figure 2.1), and images of the same field of view in the appropriate channels were overlaid to show relative localisation of signals from each channel. Correction for chromatic aberration was achieved by adjustment of violet or blue-spectrum images downwards by 1 pixel, green-spectrum images right by 2 pixels, and far-red images right by 1 pixel.

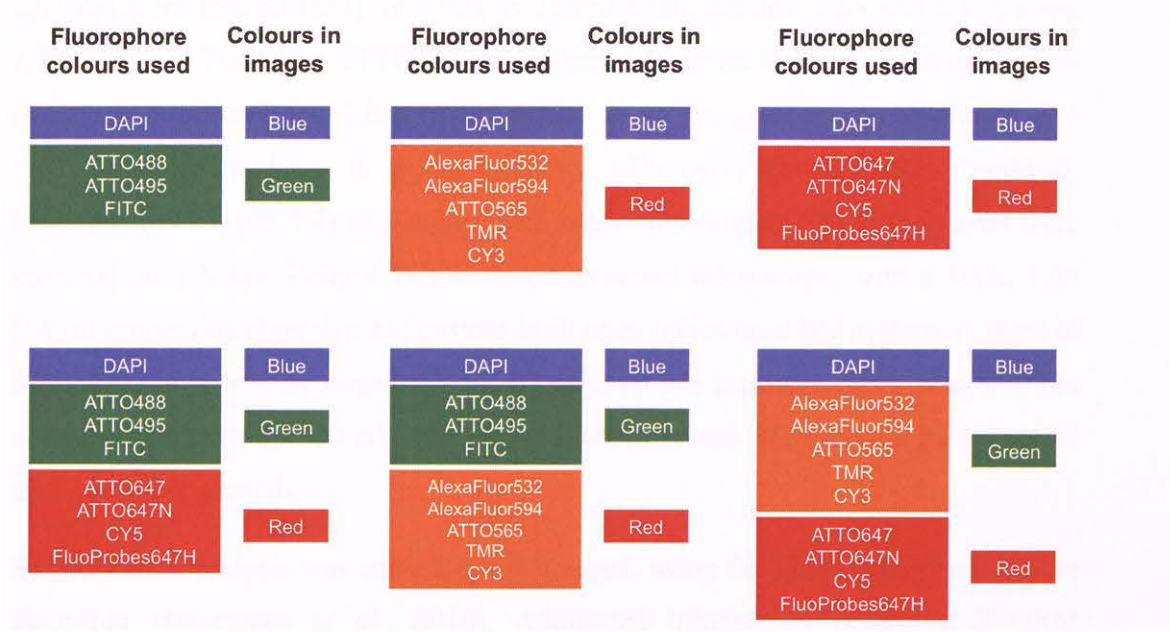

Figure 2.1: Schematic of pseudo-colours applied to spectrally distinct fluorophores, depending on the combination of fluorophores used. Single fluorophores from each group of fluorophores detected at different regions of the UV-*vis* spectrum ("colours") could be used in different combinations with each other. The pseudo-colour applied to signal from each colour channel depends on the combination of colours used; so that only red, blue and green pseudo-colours were used, for maximum contrast between colours.

2.2.14. STORM Imaging and analysis

STORM is based on the principle that if a single point-source of light can be detected, and the distortion of the light as it passes through an optical system can be modeled, the original image of the light can be calculated, and the precise location of the object can be determined. The technique makes use of high intensity light and a controlled imaging environment to stimulate the stochastic cycling of fluorophores in the sample between the light and dark states, or fluoroophore "blinking" (Vogelsang *et al.*, 2008), such that individual adjacent fluorophores are unlikely to be "on" at the same instant. Images of single fluorophores, without overlapping signals from nearby objects, can be detected as single points of light, and the centre of mass of each detected

fluorophore can be computationally localised with a very high precision (Rust *et al.*, 2006; reviewed in Henriques *et al.*, 2011). By acquiring a sufficiently large sequence of images of blinking fluorophores, the majority of fluorophores in the sample can be localised and plotted in a single reconstruction image, with a resolution of up to approximately 20 nm.

Samples were labeled for IF or FISH as described in sections 2.2.5 and 2.2.9, using ATTO488, ATTO565 or ATTO647 fluorophores. Samples were mounted on Teflon-coated diagnostic slides (Thermo Scientific) in an oxygen-scavenging buffer (0.5 mg/ml glucose oxidase, 40 µg/ml catalase, 10% (w/v) glucose and 50 mM β-mercaptoethanol, pH 7.4) and sealed with clear nail varnish. STORM images were acquired on a Nikon Eclipse Ti inverted fluorescent microscope, with a 100x, 1.49 NA oil immersion objective and custom-built open optics laser bed system. A burst of 5000-8000 images were acquired with 10 milliseconds exposure time, using 640 nm or 561 nm lasers at 60-100 mW for sample excitation, with 488 nm laser pulsing at 80 mW every 1-2 seconds.

STORM data analysis was carried out in ImageJ, using the QuickPALM processing algorithm (Henriques *et al.*, 2010). Additional information regarding STORM imaging and analysis is available in Appendix A.1.

2.3. Results

Several of the protocols used in this study are novel applications to studying the malaria parasite, necessitating extensive optimisations. Figure 2.2 provides a schematic of the workflow for the establishment of each assay used. In the following sections, only representative figures showing results after selected optimisation steps are provided, with additional individual optimisations provided separately and electronically in an Appendix, as is referenced throughout the text.

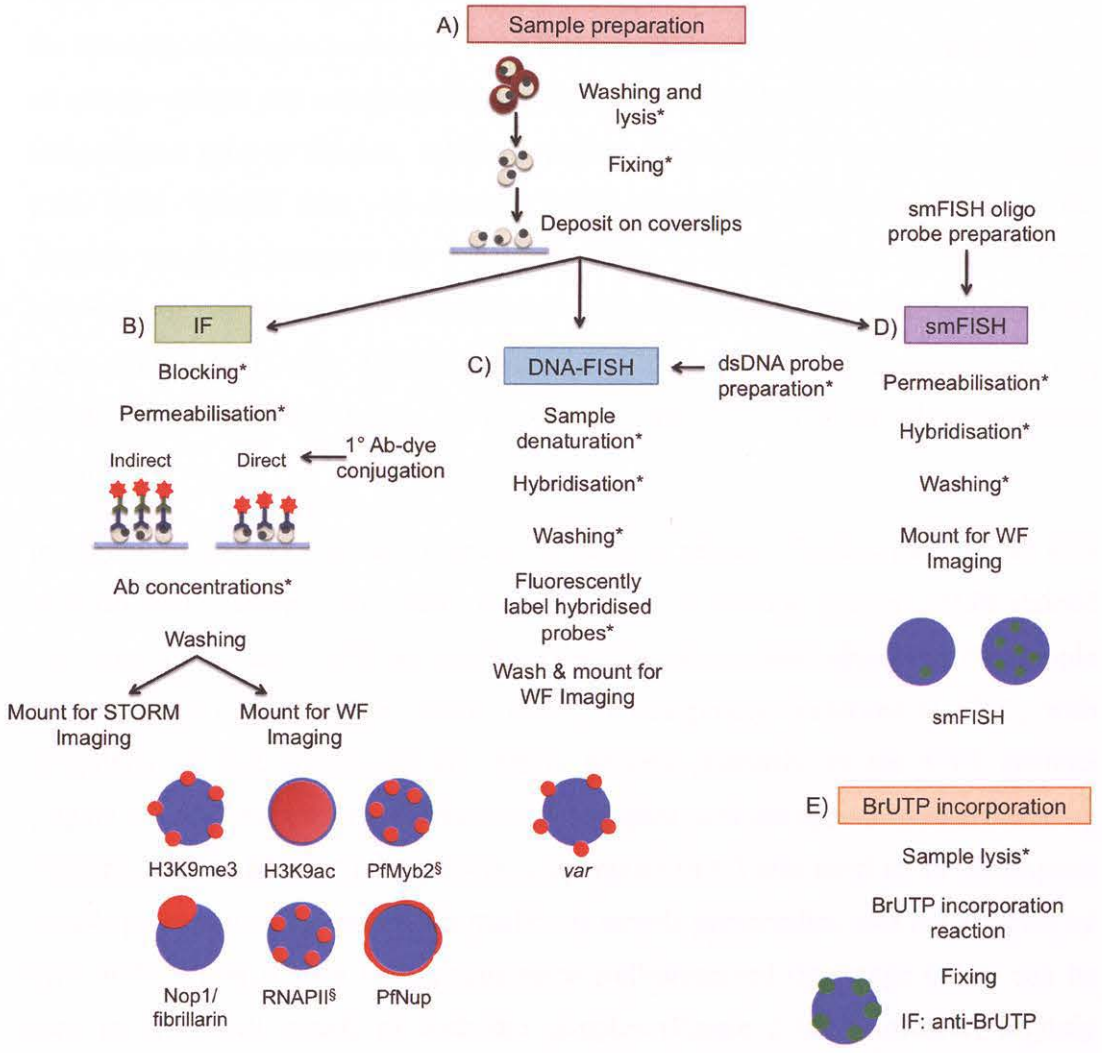

Figure 2.2: Schematic of workflow used in the establishment and optimisation of assays in this chapter. A) Sample preparation precedes other assays. Lysis of parasites (light shapes with black spot) from RBCs (red circles) is indicated. B) IF establishment included testing direct and indirect labeling, indicated by schematics of primary and labeled secondary antibodies (indirect labeling) or labeled primary antibodies (direct labeling) recognising immobilized parasties. C) DNA-FISH and D) smFISH required preparation of probes, and were optimised at several steps. E) BrUTP incorpororation was dependent on fixation and IF optimisation. Schematics of nuclei showing expected nuclear label patterning for each assay and label (green or red), on blue DAPI-stained nuclei, are included. Ab: Antibody. Asterix (*): a process or step at which conditions were optimised. §: Potential labeling pattern is uncertain; the expected patterns given are based on the expected BrUTP incorporation pattern.

2.3.1. Sample preparation: Optimisation of the fixation protocol for fluorescent microscopy assays

P. falciparum sample fixation was optimised for sample preservation and to withstand the labeling conditions used in IF and FISH protocols, with the minimum generation of sample debris and autofluorescence. Optimisation addressed sample preparation temperatures prior to fixation, solutions and conditions used for sample washing and RBC lysis, fixation time and fixatives used. Microscopy-based assessment of the samples sought to compare the levels of parasite or cellular debris in each sample, how well the parasites were preserved and autofluorescence levels in the blue (DAPI), green (FITC, ATTO488, ATTO495), orange (CY3, AlexaFluor532, AlexaFluor594, TMR, ATTO565) and far-red (CY5, FluoProbe647H, ATTO647/N) microscopy channels.

In Figure 2.3, temperature and duration of saponin release of intact parasites as well as wash buffer composition were optimised prior to fixation. Firstly, DAPI stained ring-stage nuclei are visible as small, well delineated circular objects in the sample prepared at 4°C, while they appear clumped and poorly preserved at 37°C, with irregularly shaped autofluorescent debris present primarily in the CY3 channel (Figure 2.3.A). The amount of debris in the samples does not appear to be affected by temperature (Figure 2.3A). The lower temperature (4°C) was used in all subsequent sample preparations. Secondly, the quality of sample preservation was not affected by PBS or RMPI as solutes for saponin since well-preserved ring-stage nuclei can be seen in the DAPI panels of both the samples (Figure 2.3B). However, brightly autofluorescing debris was visible in each of the CY3, CY5 and GFP channels for the sample prepared with RPMI, while this was not observed for the samples prepared with PBS. Lastly, incubation times of 5-10 minutes preserved ring-stage and late-stage schizont nuclei but 15-20 minute treatment times resulted in indistinct and irregularly shaped nuclei (Figure 2.3C, DAPI channel). Low levels of parasite-associated autofluorescence were detected in the CY3 channel in schizont parasite samples treated for 10 minutes or longer. These results suggest that a 5 minute saponin-treatment may be best suited for the release of mature-stage parasites from RBCs without producing parasite-associated debris, while a slightly longer incubation time of 10 minutes may be optimal for the complete release of younger ring-stage parasites from RBCs.

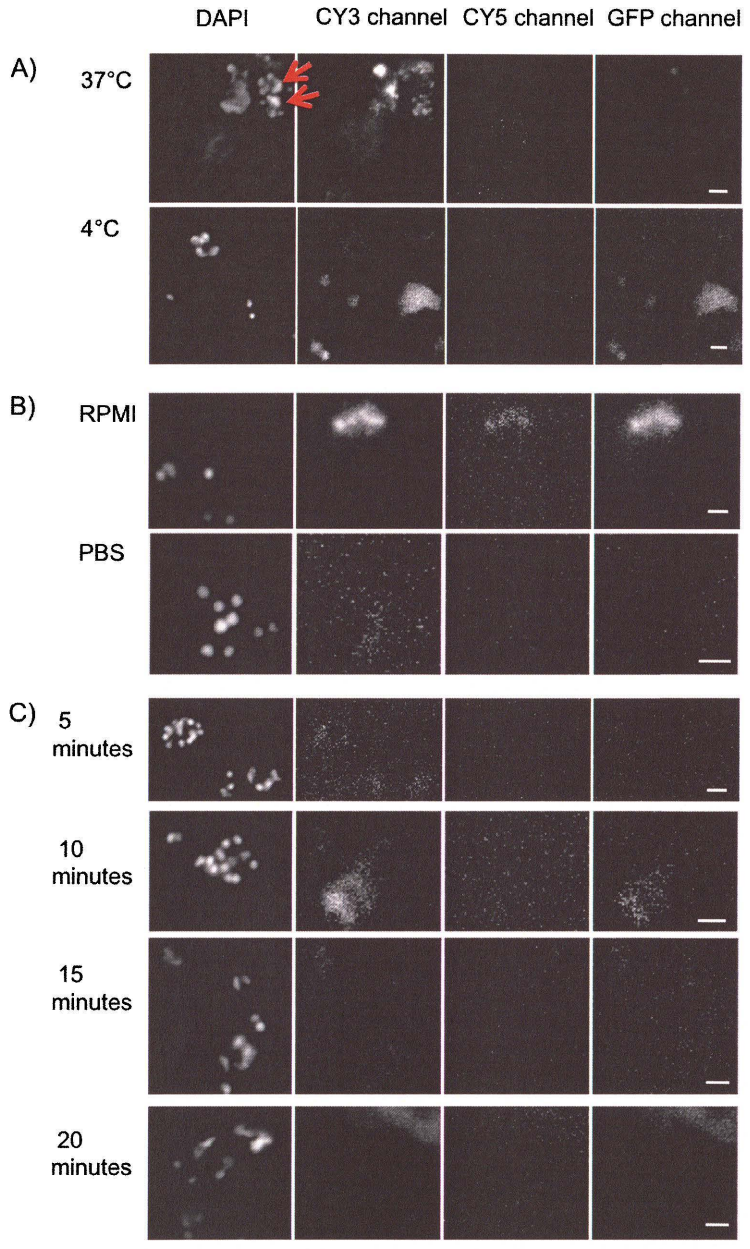

Figure 2.3: Comparison of different conditions for the washing of samples and lysis of red blood cells, and their effect on sample quality and preservation. A) Preparation of samples at different temperatures. Parasites were washed and saponin-treated at either 37°C or 4°C prior to fixation. Red arrows indicate DAPI-labeled nuclei among debris. B) Use of different buffers for washing samples prior to lysis. From culture, samples were pelleted then resuspended in either fresh RPMI or PBS, to which saponin was added. C) Duration of saponin treatment of *P. falciparum* cultures. Parasites were washed and incubated in 0.15% (w/v) saponin, at 4°C for 5, 10, 15 or 20 minutes, prior to fixation. In each case, following fixation, samples were deposited on coverslips and mounted with Vectashield with DAPI for imaging. All images are representative images of DAPI-stained fixed parasites, imaged in each of the spectrally distinct fluorescent channels shown. Scale bars =3 μm.

Following *P. falciparum* parasite sample washing and lysis from RBCs, the samples were washed and chemically fixed. Fixation conditions were optimised for fixative solution used and the duration of incubation therewith (Figure 2.4). Clear, individually distinct nuclei are visible in samples fixed for both 15 and 30 minutes, although more distinct delineation of nuclear boundaries, as well as slightly brighter DAPI labeling were observed at 30 minutes fixation (Figure 2.4A). Samples fixed overnight showed poorly preserved nuclear structure and increased levels of autofluorescence.

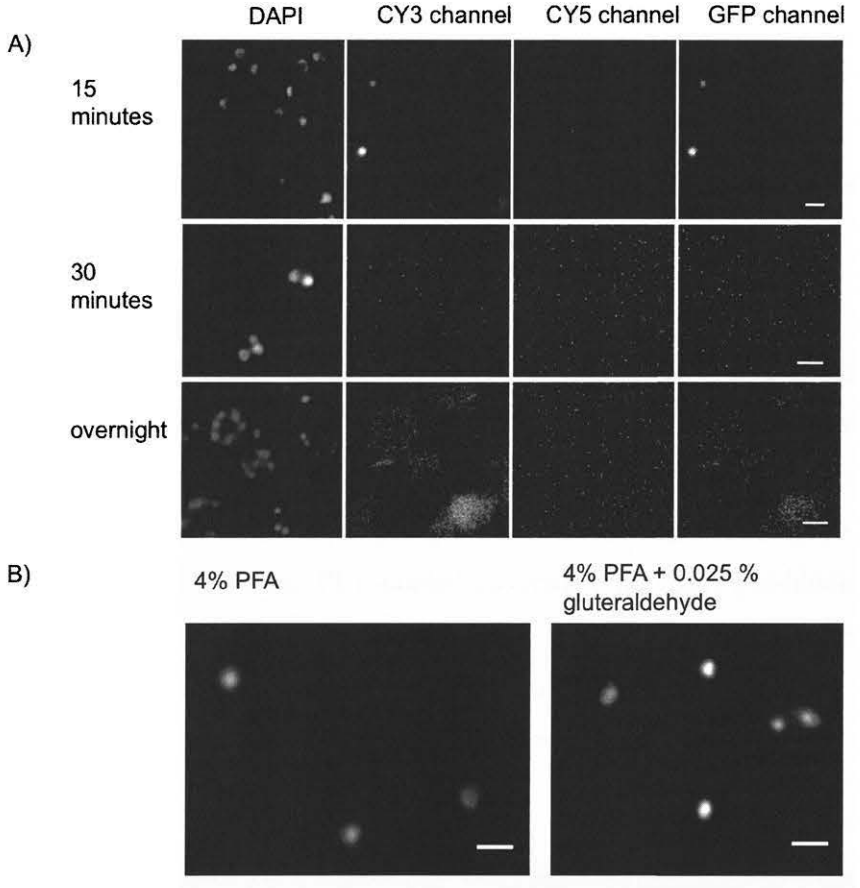

Figure 2.4: *P. falciparium* samples treated with different fixation conditions. A) Representative images of DAPI-stained parasite samples, each fixed in 4% (w/v) PFA for either 15 or 30 minutes, or overnight, at 4°C. Following fixation, samples were washed and mounted with Vectashield with DAPI for imaging. B) Representative images of DAPI-stained fixed parasites, fixed for 30 minutes in either 4% PFA in PBS, or in 4% PFA (w/v) with 0.025% (v/v) glutaraldehyde, in PBS. Following fixing, these samples were washed, and used in mock DNA-FISH experiments before being washed and mounted with Vectashield with DAPI for imaging. Scale bars =3 μm.

Fixation of samples with just 4% PFA resulted in a loss of some integrity, with nuclei appearing slightly dispersed or degraded after the FISH procedure (Figure 2.4B). In contrast, the sample fixed with additional glutaraldehyde was better able to tolerate the harsh conditions of the FISH procedure, retaining tight, regularly shaped nuclei.

2.3.2 Establishment of Immunfluorescence assays

2.3.2.1 Optimisation of the IF protocol

Optimisation of the original IF protocol by Mancio-Silva *et al.* (2008a) was carried out to ensure sufficient access of the antibody to the full nuclear structure, as well as minimising non-specific binding, debris or autofluorescence. Optimisation was carried out using a commercial rabbit-anti-H3K9me3 antibody (Millipore) known to recognise H3K9me3 in *P. falciparum* (Lopez-Rubio *et al.*, 2009).

Anti-H3K9me3 IF assays were carried out using both PLL-coated and non-coated coverslips and BSA pre-blocking steps in various combinations in order to determine the effect of these treatments on sample retention, autofluorescence and non-specific binding, respectively. Clear nuclear-associated H3K9me3 signal, visible as one or multiple punctate regions at the periphery of the nucleus or just interior to the nuclear periphery, was obtained using PLL-coated coverslips and BSA pre-blocking (Figure 2.5). Neither the use of PLL-coated coverslips nor BSA pre-blocking affected the nuclear localisation signal pattern. Additionally, no detectable debris or autofluorescence was introduced by these treatments.

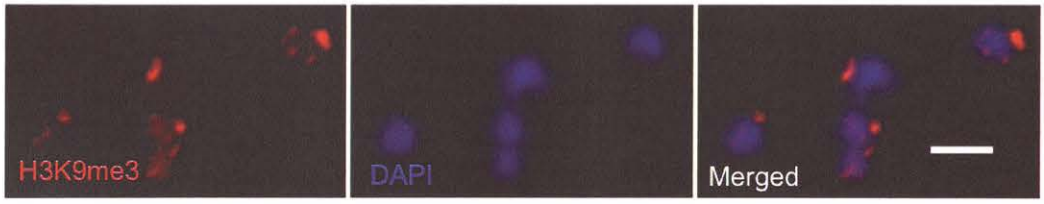

Figure 2.5: The effect of PLL-coating of coverslips and BSA pre-blocking samples in IF assays. Representative IF results of anti-H3K9me3 labeling (red), co-stained with the nuclear label DAPI (blue), carried out on a PLL-coated coverslip and using a pre-blocking step with BSA. Scale bar =3 μm.

The effect of different permeabilisation treatments on IF labeling of H3K9me3 as well as nuclear integrity was tested to determine sample permeability and access of the antibody to the nuclear target. Figure 2.6 shows characteristic H3K9me3 labeling results, independent of pre-permeabilisation, co-permeabilisation or un-permeabilised samples, with similar levels of perinuclear or nuclear interior labeling in ring-stage nuclei in each sample. A late-stage ring or trophozoite nucleus is also visible (arrow), which shows very strong perinuclear staining, arranged in multiple distinct foci. Nuclei in the co-permeabilised sample showed slight irregularity of their shape and lack of clear delineation of the nuclear periphery with slightly less distinct immuno-labeling.

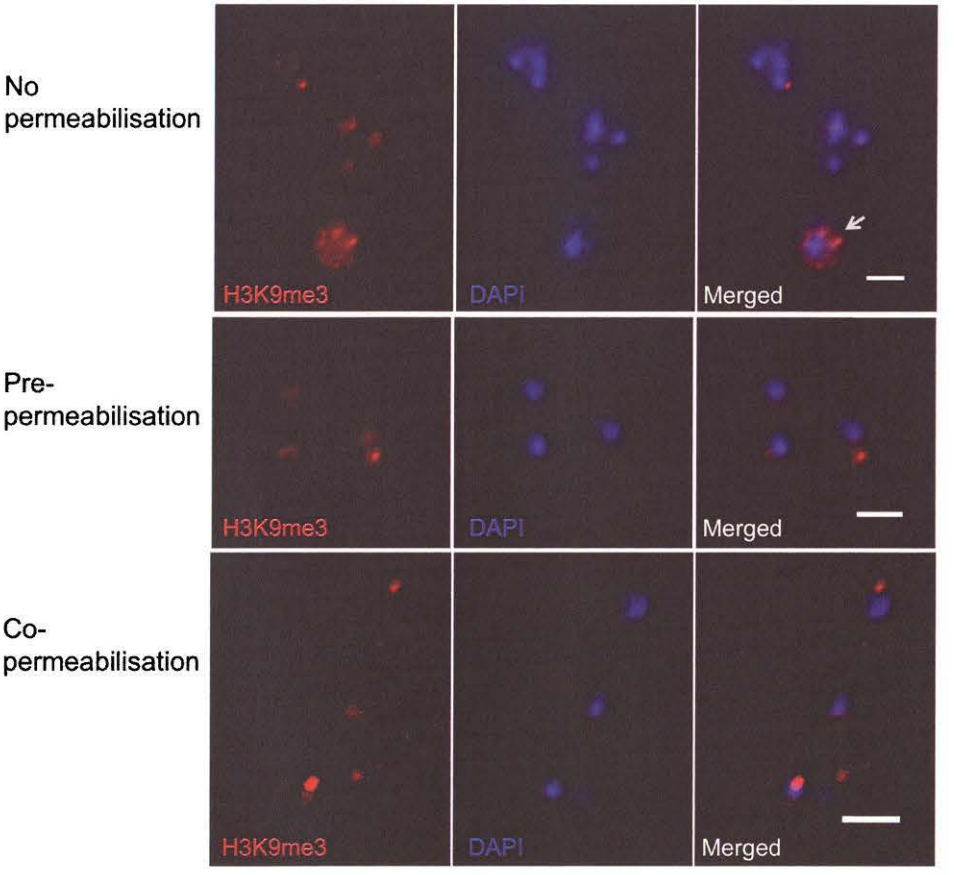

Figure 2.6: Comparison of IF results with samples subjected to different permeabilisation treatments. Representative results of IF anti-H3K9me3 labeling (red), co-stained with the nuclear label DAPI (blue), in samples subjected to no additional permeabilisation, pre-permeabilised samples pretreated with 0.01% Triton X-100 for 10 minutes, and samples that were co-permeabilised with 0.01% Triton X-100 with the antibody incubation, as labeled. The majority of nuclei detected are of ring-stage parasites. The arrow points to a late ring or trophozoite-stage nucleus, with a markedly different labeling pattern. Scale bars =3 μm.

Taking these optimisation results together, IF was subsequently performed with no additional permeabilisation using PLL-coated coverslips and a BSA pre-blocking step.

2.3.2.2 Optimisation of antibody concentrations for use in IF labeling

The optimised IF labeling protocol described above was subsequently tested on other nuclear targets. The optimal dilution factor to be used for each antibody for IF detection was determined for mouse-anti-H3K9me3, rabbit-anti-H3K9ac, mouse-anti-H3K9ac, rabbit-anti-RNAPII and chicken-anti-PfMyb2, with appropriate fluorescently labeled secondary antibodies (Table 2.1) (Figure 2.7). Additional results for each individual antibody are given in Appendix A.2, Figures A-2 to A-6.

At the determined optimal concentrations, the majority of the antibodies used produced clear, nuclear-associated signal, with minimal non-specific signal or background (Figure 2.7 A-D). By contrast, even at an optimised concentration, anti-RNAPII provided poor labeling efficiency with a low level of non-specific signal (Figure 2.7 E). The labeling patterns or sub-nuclear distributions varied for each label, ranging from perinuclear foci to diffuse signals within the nucleus. As expected, H3K9ac and RNAPII signals were primarily nuclear-interior labels, while H3K9me3 labeling was primarily perinuclear in character.

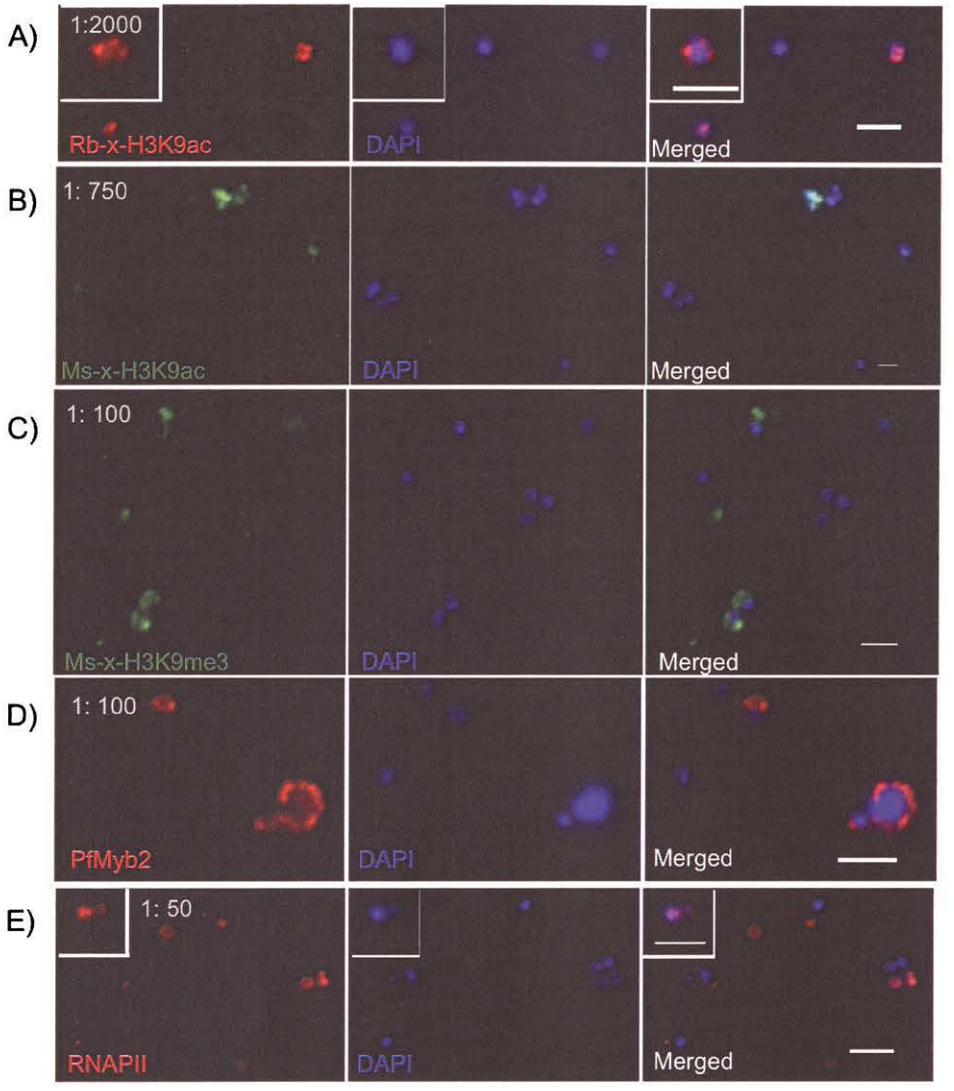

Figure 2.7: Optimised dilutions of anti-H3K9me3, anti-H3K9ac, anti-PfMyb2 and anti-RNAPII antibodies for IF. Representative results for IF assays carried out using antibodies against nuclear targets at the determined optimal dilutions, as indicated. A) Rabbit-anti-H3K9ac (red) was used at 1:2000, B) mouse-anti-H3K9ac (green) was used at 1:750, C) mouse-anti-H3K9me3 (green) was used at 1:100, D) chicken-anti-PfMyb2 (red) was used at 1:100, and E) rabbit-anti-RNAPII (red) was used at 1:50 dilution. Parasite nuclei were stained with DAPI (blue). Scale bars =3 μm.

2.3.2.3. Optimisation of IF detection of nuclear pore complexes

In order to localise and label the NPC as a marker of the nuclear periphery and as a structure possibly involved in transcriptional regulation, a non-commercial, parasite-specific anti-PfNup1 antibody (provided by the Scherf lab, Institut Pasteur, Paris) was

tested for use in IF experiments. Poor sample quality and unusually high levels of background signal and non-specific labeling complicated the titration of anti-PfNup1 (Appendix A.2, Figure A-7) and finally a 1:100 dilution was used as a compromise between signal intensity and non-specific labeling (Figure 2.8).

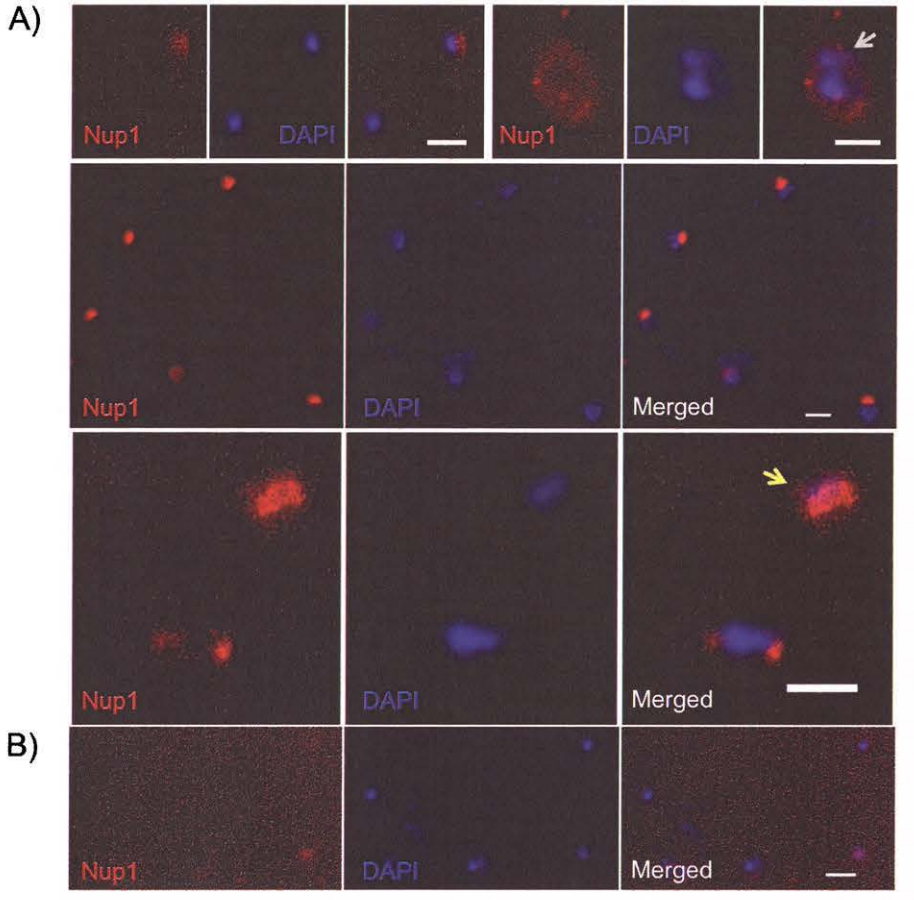

Figure 2.8: Representative images of anti-PfNup1 labeling. A) Representative results showing highly variable results of initial IF assays using 1:100 rat-anti-PfNup1 primary antibody, with anti-rat-CY5 secondary antibody (red). The parasite nuclei were stained with DAPI (blue). The grey arrow indicates perinuclear signal surrounding the nucleus. Diffuse label occupying a large portion of the nuclear volume is indicated by the yellow arrow. B) Results of similarly labeled IF assays showing loss of antibody-target binding activity. Scale bars =3 μm.

Figure 2.8A shows clear Nup1 IF signal with distinct nuclear co-localisation, and decreased non-specific signal and noise. However, the results obtained were inconsistent in both the pattern of nuclear localisation as well as intensity or quality of signal and background noise. Detected labeling included a perinuclear signal pattern

encompassing a part or the whole of the nucleus (Figure 2.8A, grey arrow) and a diffuse pattern covering a large part of the nuclear volume (Figure 2.8A, yellow arrow). More frequently, a single signal focus was observed either at the periphery or just within the nuclear volume (top-left and middle panel in Figure 2.8A). Subsequent experiments with this antibody resulted in decreased signal intensity, suggesting a loss of antibody binding activity (Figure 2.8B). The anti-PfNup1 antibody thus could not be used in further labeling experiments.

2.3.2.4. Optimisation of IF detection of the nucleolus

The nucleolar protein fibrillarin was identified as a potential IF target for nucleolar labeling in *P. falciparum* parasites. As no plasmodial-specific anti-nucleolar antibodies were readily available, several commercial anti-fibrillarin antibodies (listed with details in Table 2.1) were selected as candidate antibodies for binding to the nuclear structure in *P. falciparum* IF experiments. These antibodies were known to have broad cross-reactivity against fibrillarin in a number of species, including human, mouse, *Caenorhabditis elegans*, Chicken, *D. melanogaster* and *Schizosaccharomyces pombe.* IF was carried out with each antibody (mouse-anti-fibrillarin 38F3, mouse-anti-fibrillarin 6H4, goat-anti-fibrillarin A-16, mouse-anti-fibrillarin M-A1) to test for possible cross-reactivity with *P. falciparum* fibrillarin (Figure 2.9).

From these, only anti-fibrillarin A-16 labeling was seemingly able to detect the nucleolus. Some signals were detected as one or two sharp foci that do appear to be associated with the nuclear DAPI stain. However, a significant level of background noise and some non-specific signal was detected (e.g. signal adjacent and distinct to the nuclear signal). All other antibodies tested resulted in variable, non-specific binding to structures not co-localised with the nucleus, in addition to a large amount of background noise.

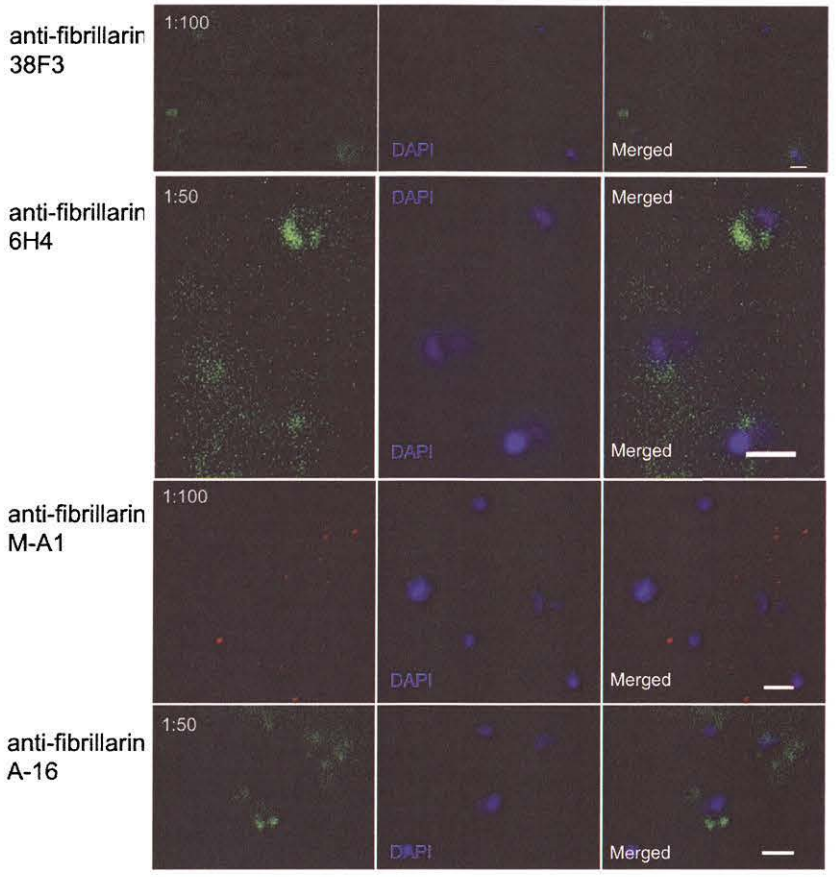

Figure 2.9: Comparison of IF results using different anti-fibrillarin antibodies. Representative results of IF experiments using 1:100 mouse-anti-fibrillarin 38F3, 1:50 mouse-anti-fibrillarin 6H4, 1:100 mouse-anti-fibrillarin M-A1, and 1:50 goat-anti-fibrillarin A-16, as labeled. Anti-fibrillarin 38F3 and 6H4 are labeled with 1:500 ATTO488-conjugated rabbit-anti-mouse (green). Anti-fibrillarin M-A1 is labeled with 1:500 ATTO565-conjugated rabbit-anti-mouse (red), and anti-fibrillarin A-16 is labeled with 1:500 ATTO488-conjugated rabbit-anti-goat (green). Nuclei are co-stained with DAPI (blue). Scale bars =3 μm.

Based on these observations, the use of the anti-fibrillarin A-16 antibody was titrated to optimise antibody concentration for IF assays with *P. falciparum* parasites (Figure 2.10). Anti-fibrillarin A-16 used at 1:50 and 1:100 dilutions produced similar signal patterns, with a similar intensity. In each case nuclear-associated signal occurs as one or two small, bright foci overlapping with the DAPI signal at the nuclear periphery. As can be expected, decreased antibody concentration results in a smaller proportion of nuclear-associated signal with decreased signal-to-noise ratio although the high level of non-specific signal between the two samples appears to remain constant

(Figure 2.10). This persistent non-specific signal renders the anti-fibrillarin A-16 antibody unsuitable for the high-content assays used in this study.

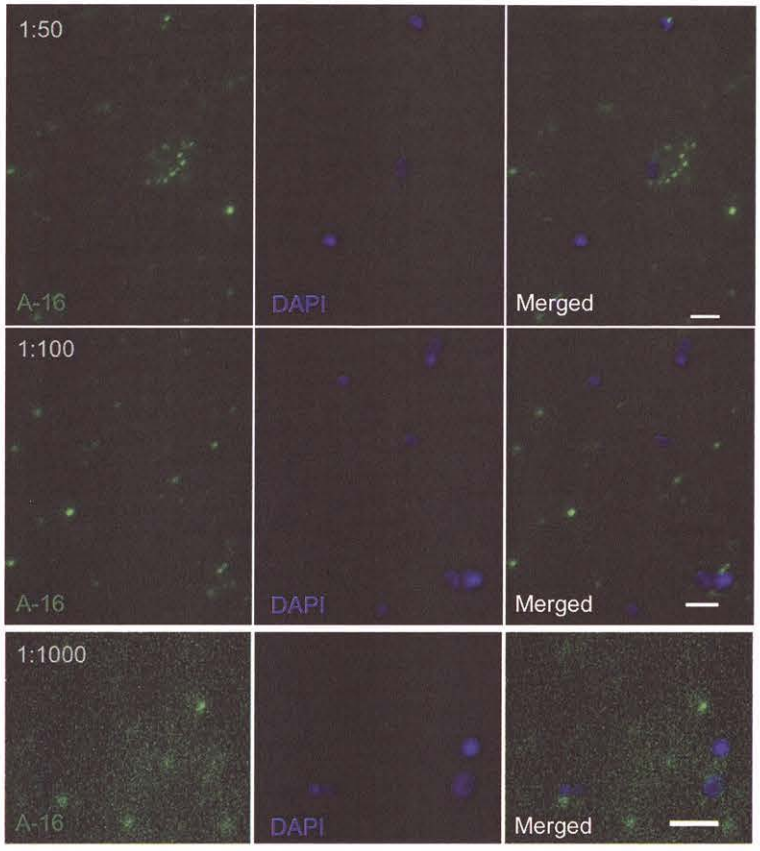

Figure 2.10: Titration of anti-fibrillarin A-16 antibody for IF. Representative results for IF assays carried out using 1:50, 1:100 and 1:1000 goat-anti-fibrillarin A-16 primary antibody, as indicated, with anti-goat-ATTO488 secondary antibody (green). The parasite nuclei were stained with DAPI (blue). Scale bars =3 μm.

2.3.2.5. Fluorescent labeling of primary antibodies

Primary antibodies previously established or tested for indirect IF detection (rabbit-anti-H3K9me3, rabbit-antiH3K9ac, chicken-anti-PfMyb2 and goat-anti-fibrillarin A-16 primary antibodies), were used here in antibody-fluorophore conjugation reactions in order to produce directly labeled primary antibodies. Prior to conjugation rabbit-anti-H3K9me3 and rabbit-antiH3K9ac antibodies were purified from the initial buffer or serum they were supplied in (as described in sections 2.2.6.1 and 2.2.6.2), to limit conjugation inhibitory compounds like with free amide groups. The binding specificity and sensitivity of the unconjugated, purified antibodies were tested by

indirect IF with titrations of purified antibodies (Figure 2.11A). Specific H3K9me3 signal was obtained at a 1:500 diltution, while H3K9ac signal was only detected at a 1:1000 dilution.

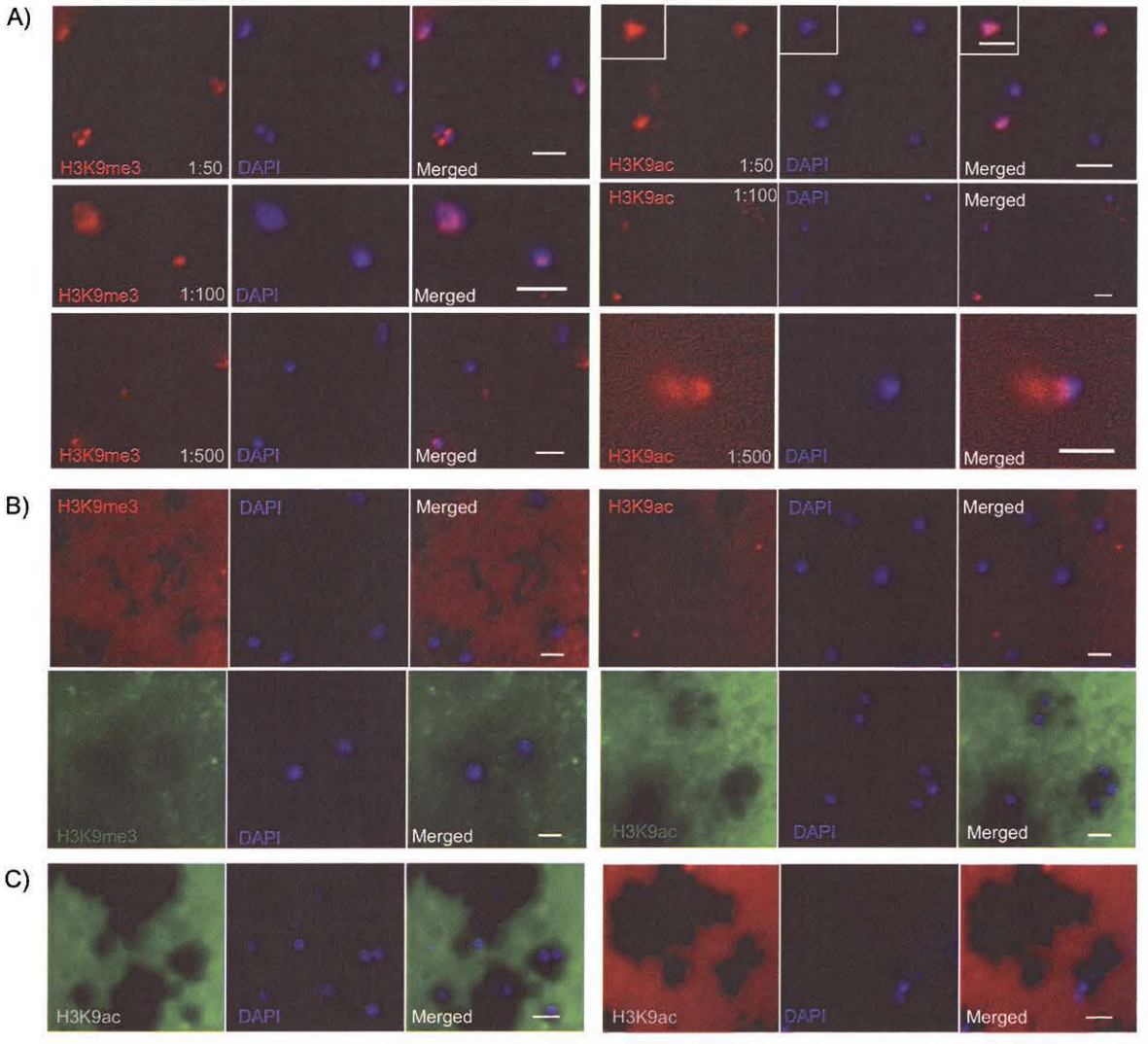

Figure 2.11: IF results in preparation of fluorophore-conjugated primary antibodies. A) Representative images of indirect IF detection of titrated, purified primary antibodies, rabbit-anti-H3K9ac and rabbit-anti-H3K9me3, as labeled (red). B) Representative images of direct IF using unpurified anti-H3K9me3 and anti-H3K9ac, directly conjugated to ATTO488 (green) and FluoProbe647H (red), as labeled. C) Representative images of direct IF using purified anti-H3K9ac, directly conjugated to ATTO488 (green) and FluoProbe647H (red). The parasite nuclei were stained with DAPI (blue). Scale bars =3 μm.

Following confirmation of antibody activity both unpurified and purified anti-H3K9me3 and anti-H3K9ac antibodies were used in conjugation reactions for

labeling with ATTO488 or FluoProbe647H fluorophores (as described in section 2.2.6.3). Figure 2.11B and C shows direct IF results using unpurified and purified primary antibodies, respectively, following the fluorophore conjugation reactions. Each representative image in Figure 2.11B and C shows almost exclusively non-specific labeling for antibodies conjugated to each dye, with a very small proportion of signal forming foci at, or just beyond, the nuclear periphery. The very high levels of non-specific labeling have a striking pattern themselves with signal largely excluded from the parasite and a small surrounding region. Conjugation of anti-PfMyb2 and anti-fibrillarin A-16 primary antibodies showed a similar loss of antibody binding affinity (Appendix A.2, Figure A-8).

2.3.3. Establishment of BrUTP incorporation assay and IF detection

BrUTP incorporation was carried out according to the published protocol by Mancio-Silva *et al.* (2010), as described in section 2.2.7. Saponin permeabilisation, as was used for red blood cell lysis above, was optimised in order to 1) ensure sufficient nuclear permeability to the BrUTP incorporation reaction components and the labeling antibodies and 2) maintain maximal nuclear preservation. Increasing concentrations of saponin (from 0.05 to 0.15%) resulted in improvement of nuclear-associated BrUTP incorporation and IF detection signals and diminished levels of non-specific signal (Appendix A.2, Figure A-9).

BrUTP incorporation assay with 0.15% saponin treatment resulted in a much greater degree of nuclear association and overlap of BrUTP signal with DAPI signal, even for various different stages of the parasite (rings vs trophozoites) (Figure 2.12). The results were also more reproducible between experiments. The majority of the observed signal was in the expected perinuclear localisation, while there was also an increased level of signal within the nuclear volume, particularly in the later-stage nuclei. Both nuclear-associated signals as well as high levels of non-specific signal were detected from both fluorophores used.

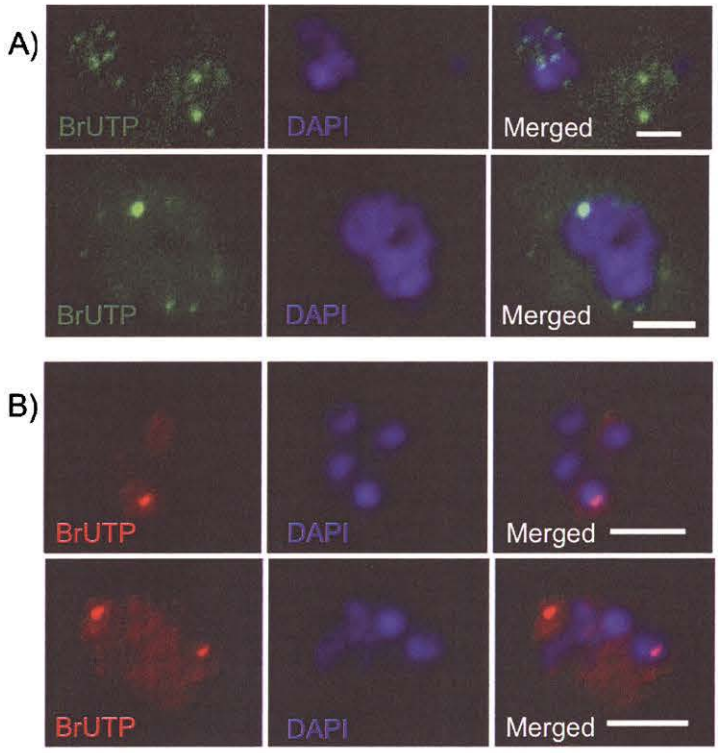

Figure 2.12: BrUTP incorporation assays. Representative results of two independent experiments (A and B) of IF against incorporated BrUTP. A) Trophozoite parasites with incorporated BrUTP labeled with 1:100 mouse anti-BrdU and 1:500 rabbit-anti-mouse-ATTO488 (green). B) Ring-stage parasites with incorporated BrUTP labeled with 1:100 mouse anti-BrdU and rabbit-anti-mouse-A565 (red). The parasite nuclei were stained with DAPI (blue). Scale bars =3 µm.

2.3.4. Establishment of DNA-FISH

2.3.4.1. Probe template isolation and amplification

Working with post-doctoral fellow Dr Youtaro Shibayama (Mhlanga Lab, CSIR, Pretoria), gDNA was extracted from cultured samples of *P. falciparum* parasites for the production of DNA-FISH probes, as described in section 2.2.8.1. The extracted gDNA concentration was determined to be 40 ng/µl and gDNA quality was verified by gel electrophoresis (Appendix A.2, Figure A-10). The extracted gDNA was used as template in optimisation reactions for PCR amplification of the probe regions for *var* exon 2A, 2B, and 2C (as per section 2.2.8.2) (Figure 2.13).

PCR amplification, with 64°C extension time, of each of the Exon 2 probe regions produced broad, intense bands of the expected product sizes (1185 bp, 1260 bp, 1272 bp, for Exon 2A, 2B and 2C, respectively) for each of the primer pairs, albeit with some overamplification evident (Figure 2.13A). In contrast, extension at 68°C resulted in loss of detectable amplification of Exon 2B so that 64°C was therefore used as the extension temperature in subsequent reactions.

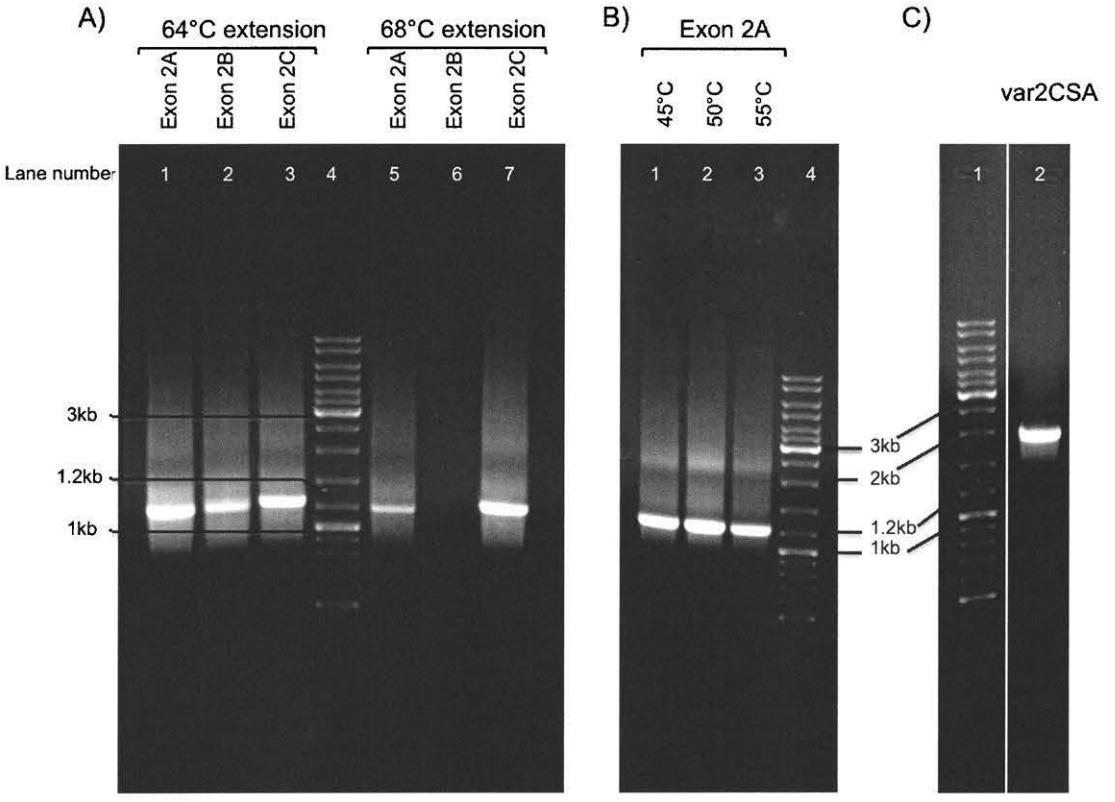

Figure 2.13: Testing different PCR extension and annealing temperatures. Agarose electrophoresis gels showing PCR products for A) different extension temperatures and B) annealing temperatures, using extracted gDNA as template. A) Lanes 1-3: PCR product for primer sets Exon 2A, Exon 2B and Exon 2C, at 64°C extension temperature, 45°C annealing temperature, lane 4: DNA mix ladder, lanes 5-7: PCR product for primer sets Exon 2A, Exon 2B and Exon 2C, at 68°C extension temperature, 45°C annealing temperature. B) Lane 1-3: PCR product for primer set Exon 2A at 64°C extension temperature, 45°C, 50°C and 55°C annealing temperature, lane 4: DNA mix ladder. C) Agarose electrophoresis gel showing PCR products using *var*2CSA primer set and extracted gDNA as template, at 64°C extension temperature and 50°C annealing temperature (lane 2). Lane 1: DNA mix ladder.

The effect of different annealing temperatures (45-55°C) on the amplification of just one primer set, Exon 2A was tested to check if this may reduce the production of smears of over-amplified product (Figure 2.13B). Although little difference was

observed in the product smear between these samples, an annealing temperarature of 50°C was used for subsequent PCR experiments. The same PCR conditions were tested using the *var*2CSA primer pair (Figure 2.13C). Although the reaction produces a bright band of the expected product size (~2kb in length), the presence of two bands of approximately 7.5 kb and 6.5 kb are indications of a small amount of non-specific annealing and amplification in the reaction.

Despite the slight overamplification and non-specific product, this level of PCR optimisation is considered sufficient for the application and the desired product bands were gel purified as per section 2.2.8.2. The gel-purified dsDNA probe fragments were subsequently modified to allow FISH detection through biotin labeling, as described in section 2.2.8.3. The efficiency and yield of this incorporation reaction was densiometrically quantified as in section 2.2.8.3, using a chromogenic assay on a dot-blot array (Figure 2.14, Table 2.4). Although the biotinylation yields were low and variable, they were sufficient for use with DNA-FISH and these probes were used in the establishment of DNA-FISH labeling in the next section.

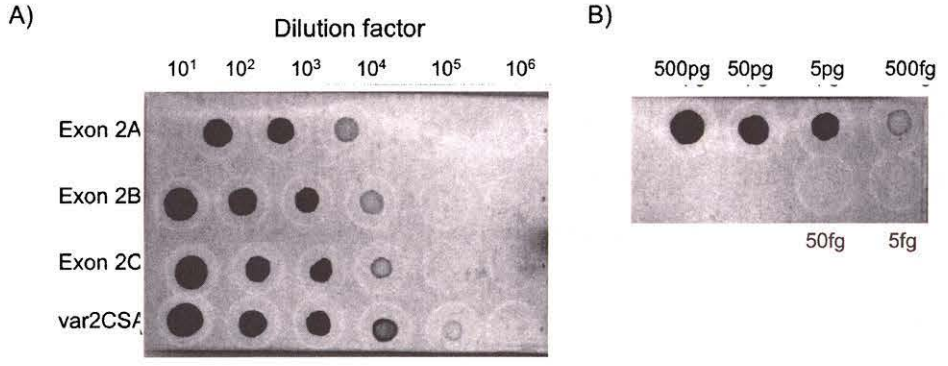

Figure 2.14: Dot blots for assessment of biotinylated probe labeling efficiency. A) Dot blot of dilution series, indicated by the dilution factor, of the biotinylation reaction products each of the DNA-FISH probes indicated. B) Dot blot of a series of dilutions of biotinylated DNA standards of known concentrations, as indicated.

Table 2.4: Concentrations and yields of biotinylated DNA-FISH probes per 50 µl reaction.

Probe	Concentration (ng/ul)	Total Yield (ng)
Exon 2A	18.68	93.4
Exon 2B	11.95	597.5
Exon 2C	9.31	465.7
*var*2CSA	29.24	1462.0

2.3.4.2 DNA-FISH optimisation

DNA-FISH was optimised based on previously published protocols (Ralph *et al.*, 2005 and Mancio-Silva *et al.*, 2008b). Protocol optimisation tested multiple aspects of the DNA-FISH protocols, addressing denaturation and hybridisation conditions, as well as sample washing and fluorescent labeling processes (Figure 2.15).

Hybridisation in 50% formamide, 10% dextran sulphate and 2x SSC (hybridisation buffer A) at higher denaturation temperatures resulted in primarily diffuse labeling within the nucleus. Lowering the denaturation temperature improved this somewhat, with a small degree of punctate perinuclear labeling visible (Figure 2.15A). Improved signal was obtained in a 2x SSPE buffer (hybridisation buffer B), resulting in more condensed FISH labeling signal, with some more distinct perinuclear foci detectable (Figure 2.15B). Changing the sample washing to a shorter process of 30 minutes with wash buffer at 37°C, followed by a series of 10 minute washes at 50°C in increasing SSC buffer concentrations (Figure 2.15C) resulted in DNA-FISH signals arranged in multiple punctate, primarily perinuclear foci. Such signals are in accordance with expected *var* exon2 signal patterns. More clearly punctate signals were obtained with a 30 minute, 80°C denaturation treatment in each case; this thermal treatment appearing to be more gentle on the samples. Hence, all further DNA-FISH experiments were carried out using hybridisation buffer B, the lower temperature denaturation treatment, and the shorter wash process B.

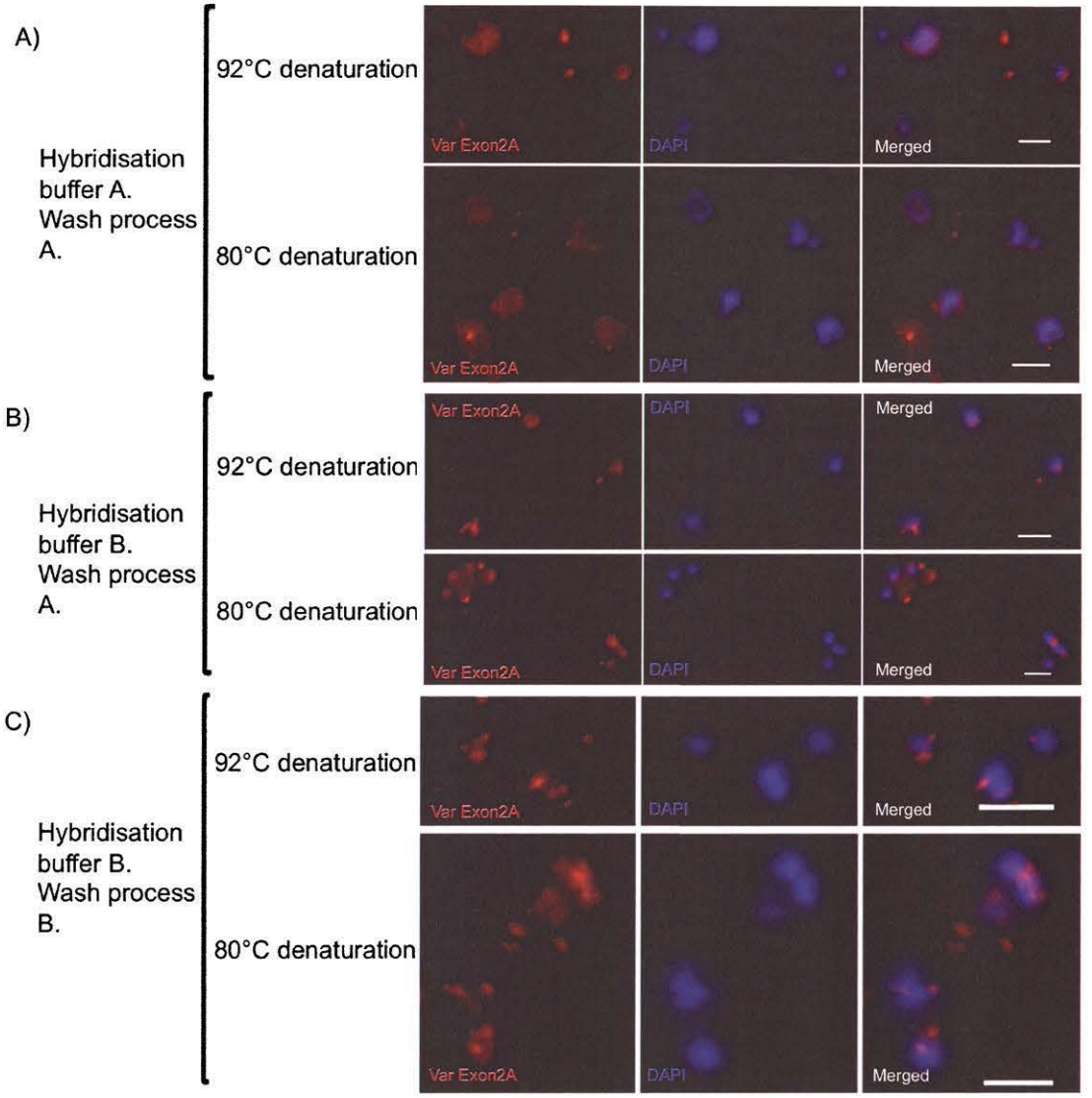

Figure 2.15: Optimisation of hybridisation and wash conditions for DNA-FISH. Representative images of FISH results of the *var* exon2A region under different hybridisation and washing conditions. FISH was carried out with A) a 2x SSC, 50% formamide, 10% dextran sulphate buffer (hybridisation buffer A), or B) a 2x SSPE, 50% formamide, 10% dextran sulphate buffer (hybridisation buffer B), followed by washing at 50°C for 30 minutes with wash buffer, and a series of wash steps in SSC buffers of increasing concentration, at 37°C or room temperature (process A). C) FISH results using hybridisation buffer B, followed by wash process B: 30 minutes at 37° with wash buffer and a series of 10 minute washes at 50°C in SSC buffer of increasing concentration. In each case, samples were denatured at either 92°C for 5 minutes or 80°C for 30 minutes. Hybridised FISH probe was detected with streptavidin-conjugated ATTO565 (red). Nuclei were detected with DAPI (blue). Scale bars =3 μm.

The effect of different blocking and washing treatments on the specificity of labeling of hybridised FISH probe with streptavidin-conjugated fluorophore was also tested. Various blocking conditions were tested (Figure 2.16), which indicated that the use of a Tween solution in washing increased the level of fluorescence in the CY3 channel in particular, which appears to be due to the deposition of autofluorescent debris (Figure 2.16A).

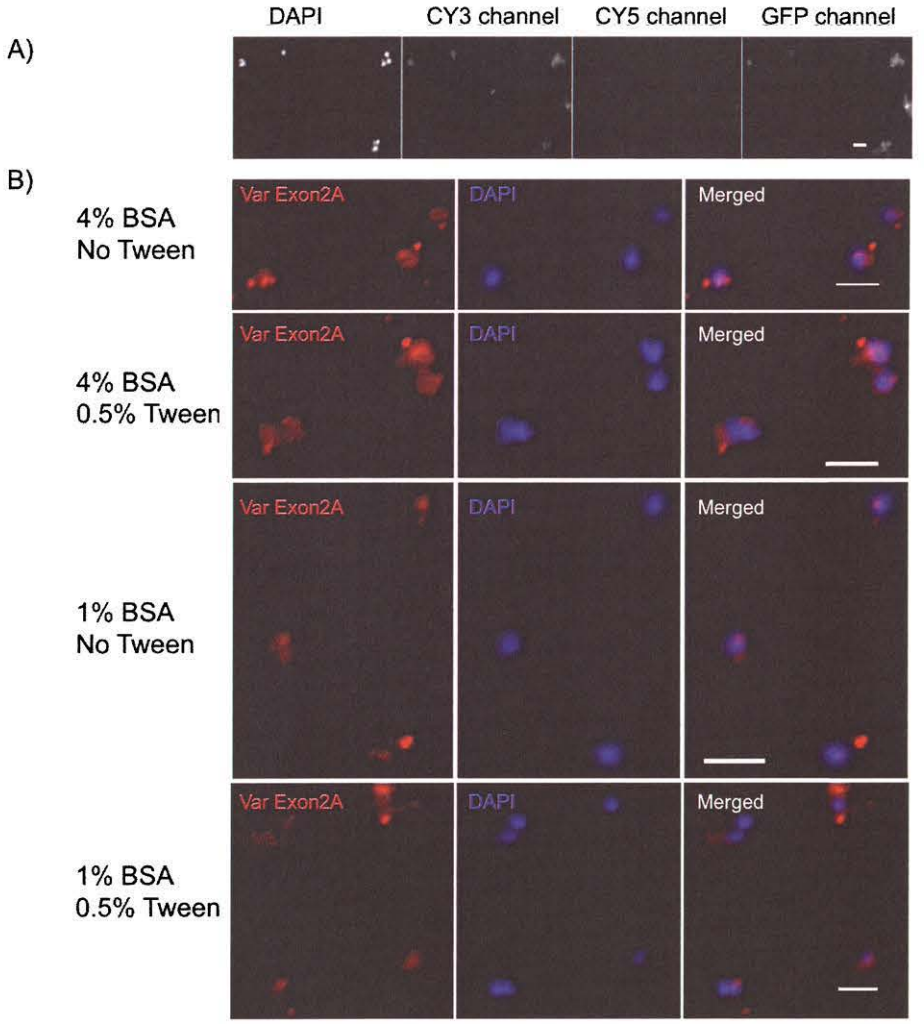

Figure 2.16: Testing the effect of BSA blocking and Tween washing on labeling with streptavidin-conjugated fluorophores for DNA-FISH detection. A) Representative images of a "blank" labeling reaction, in which no probe or fluorophore was used. Following a mock hyridisation and labeling process, the parasites were washed with 0.5% Tween in PBS. B) Representative images of streptavidin-conjugated ATTO565 dectection of the hybridised *var* exon2A FISH probe (red), under different blocking and washing conditions, as indicated. Nuclei were detected with DAPI (blue). Scale bars =3 μm.

Even though little difference in signal specificity or background signal can be seen between the samples washed with Tween or those washed simply in PBS (Figure 2.16B), further use of Tween in washing was avoided to limit the possible introduction of debris into samples. Although signal foci in samples blocked with 1% BSA was less distinct compared to 4% BSA treatment, the latter also resulted in increased background signal. Thus fluorescent labeling of hybridised FISH probes in all subsequent FISH experiments was carried out using a 1% BSA blocking solution, and washed only in PBS.

2.3.5 Establishment of single molecule FISH (smFISH)

We previously developed a smFISH protocol for the detection of nascent gene transcripts in trophozoites (Griffiths, 2009). This protocol (described in section 2.2.10.2) was applied in pair-wise experiments probing for more than one transcript at a time, which resulted in the detection of co-localised or very closely associated signal foci that were in turn co-localised with the nuclear volume or the nuclear periphery (Figure 2.17). However, the protocol could not consistently produce nuclear localisation or co-locailisation of signal foci, necessitating additional optimisations as described below.

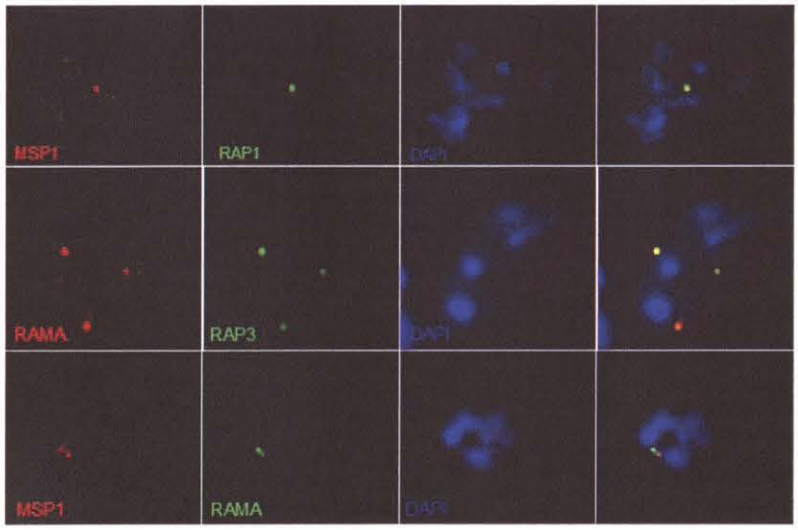

Figure 2.17: smFISH results obtained in trophozoites with original smFISH protocol. Representative images of single RAP1, RAP3, MSP1 or RAMA RNA foci obtained in trophozoite nuclei, and their co-localisation with transcripts from other genes.

2.3.5.1 smFISH optimisation

smFISH probes against the ring-stage expressed target genes CTP synthetase (CTPSyn; PF14_0100), adenyl succinate synthetase (AdSucSyn; PF13_0287) and inosine monophosphate dehydrogenase (IMP-DHG; PFI1020c) were newly designed using the online design tool on the single molecule FISH web page (section 2.2.10.1; Appendix A.3). Results of the conjugation and purification of each of the smFISH probe sets to the fluorescent dyes ATTO495 and ATTO647N (as described in section 2.2.10.1) are presented in Appendix A.4.

Using smFISH probes against trophozoite-expressed genes RAP1, RAP3 and RAMA, different permeability and hybridisation stringency conditions were tested (Figure 2.18). Both Triton X-100 and ethanol permeabilisation showed poor quality signal, but almost full nuclear-association was observed in the Triton X-100 treated sample (Figure 2.18A). Further smFISH experiments were carried out using the detergent permeabilisation.

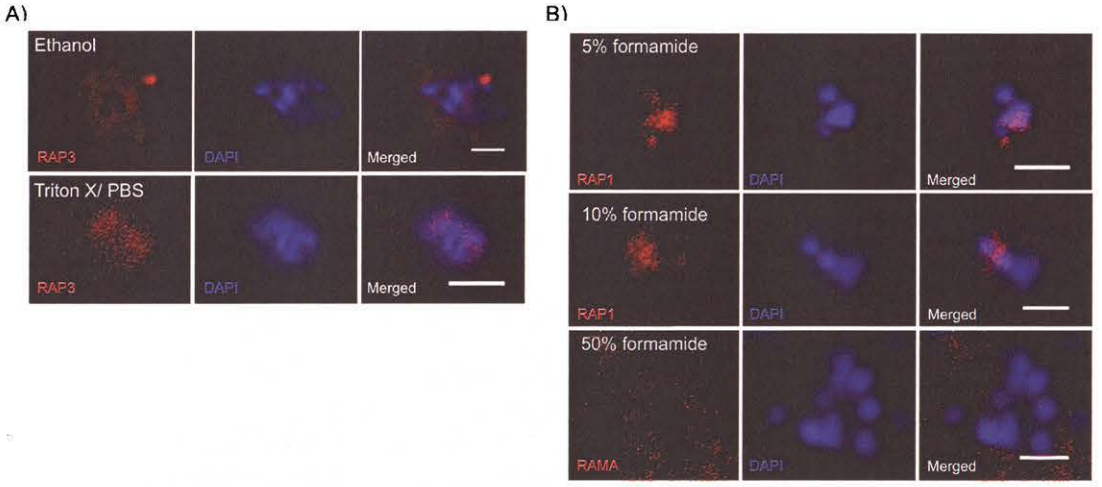

Figure 2.18: Testing permeabilisation and hybridisation stringency conditions for smFISH in late-stage parasites. A) smFISH on fixed parasites permeabilised in 70% ethanol overnight, or stored in PBS overnight and permabilised with 0.1% Triton X-100 for 5 minutes. RAP3-AlexaFluor594 probes (red) were used at a hybridisation stringency of 10% formamide. B) smFISH in Triton X-100 permeabilised parasites, with hybridisation and wash buffers containing either 5%, 10% or 50% formamide. RAP1-AlexaFluor594 or RAMA-CY3 probes (red) were used. The parasite nuclei were stained with DAPI (blue). Scale bars =3 μm.

High stringency (50% formamide) hybridisation resulted in almost no nuclear-associated probe signal, which improved at 10% formamide where a small amount of

smFISH probe signal was observed associated with the nuclear stain. This signal appears more specific with 10% formamide than at the lowest stringency (5% formamide). Subsequent smFISH experiments were carried out at a stringency of 10% formamide.

All previous smFISH experiments were carried out in late-stage parasites and here the protocol was adapted to focus on ring-stage parasites by changing the washing process and hybridisation buffer (Figure 2.19). Probe signals appear to be comparable between the ring-stage and trophozoite-stage samples, with strong nuclear-associated signal in each case. Use of simpler wash steps produced slightly brighter signals, but in each case had little effect on signal specificity (Figure 2.19A and B). Additionally, optimisation of hybridisation conditions using a buffer containing 2X SSPE instead of 2X SSC resulted in marginally more intense probe signal, with some nuclear co-localisation (Figure 2.19C).

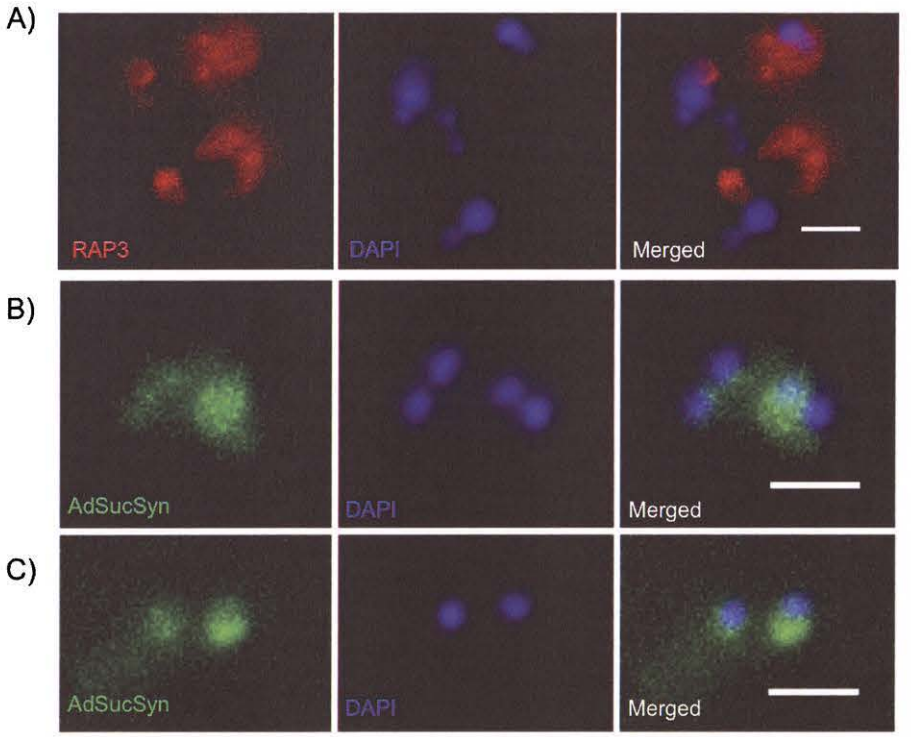

Figure 2.19: smFISH in early and late-stage parasites, using different hybridisation buffers and a shorter wash process. Representative results of smFISH in (A) trophozoites and (B) rings, using a hybridisation buffer containg 2X SSC. RAP3-AlexaFluor594 probes (red) were used in A, AdSucSyn-ATTO495 probes (green) were used in B. C) Representative results of smFISH in rings, using a hybridisation buffer containing 2X SSPE and AdSucSyn-ATTO495 probes (green). Each sample was washed twice in wash buffer (10% formamide, 2X SSC) before mounting. Parasite nuclei were stained with DAPI (blue). Scale bars =3 μm.

2.3.5.2. Application of the adapted smFISH protocol to ring-stage parasites using different probes

smFISH experiments were subsequently carried out with ring-stage parasites using probes prepared against AdSucSyn, CTPSyn and IMP-DHG (Figure 2.20). With the exception of CTPSyn-ATTO647N (with perinuclear signals), signal detected with all probes, labeled with either ATTO495 or ATTO647N, appeared largely diffuse, occupying a large part of the nuclear volume or a perinuclear region with some autofluorescence of the parasite cytoplasm. Due to the diffuse, poor-quality signal obtained with each probe, and the high levels of non-specific signal detected, the adapted smFISH protocol could not be used for reliable fluorescent detection of gene transcripts.

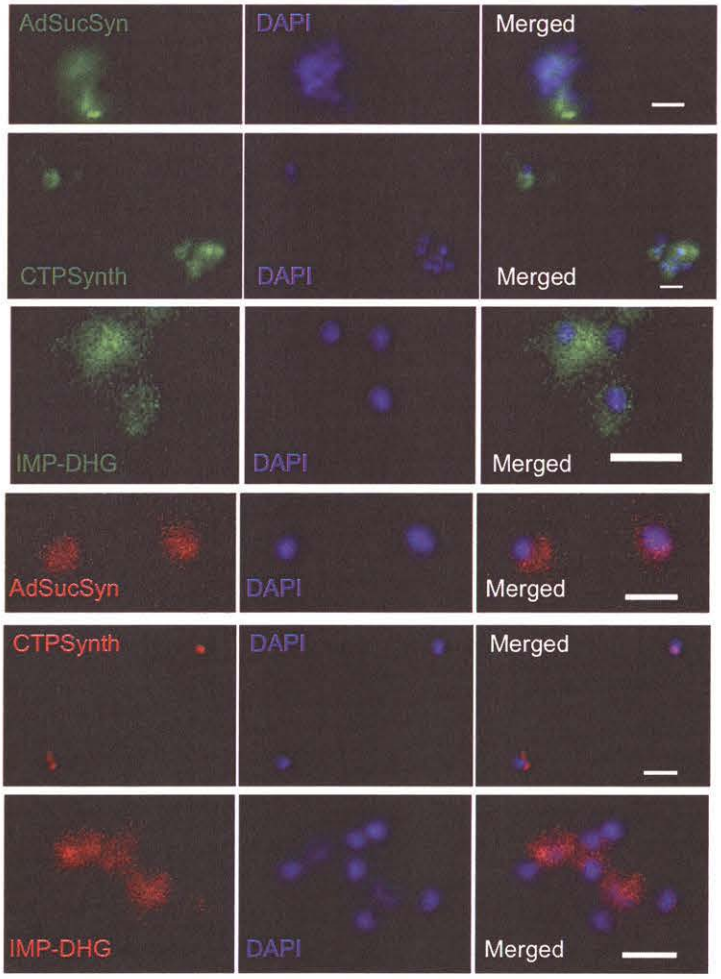

Figure 2.20: smFISH results obtained in ring-stage parasites. Representative results of smFISH images using AdSucSyn, CTPSyn and IMP-DHG probes, conjugated to ATTO495 (green) and ATTO647N (red). The parasite nuclei were stained with DAPI (blue). Scale bars =3 µm.

2.3.6. Application of STORM imaging to *P. falciparum*

The suitability of STORM for use in *P. falciparum* was tested using anti-PfMyb2 and anti-H3K9ac IF labeling. Figure 2.21 shows selected results comparing the STORM reconstruction image to that taken with wide-field epifluorescent imaging.

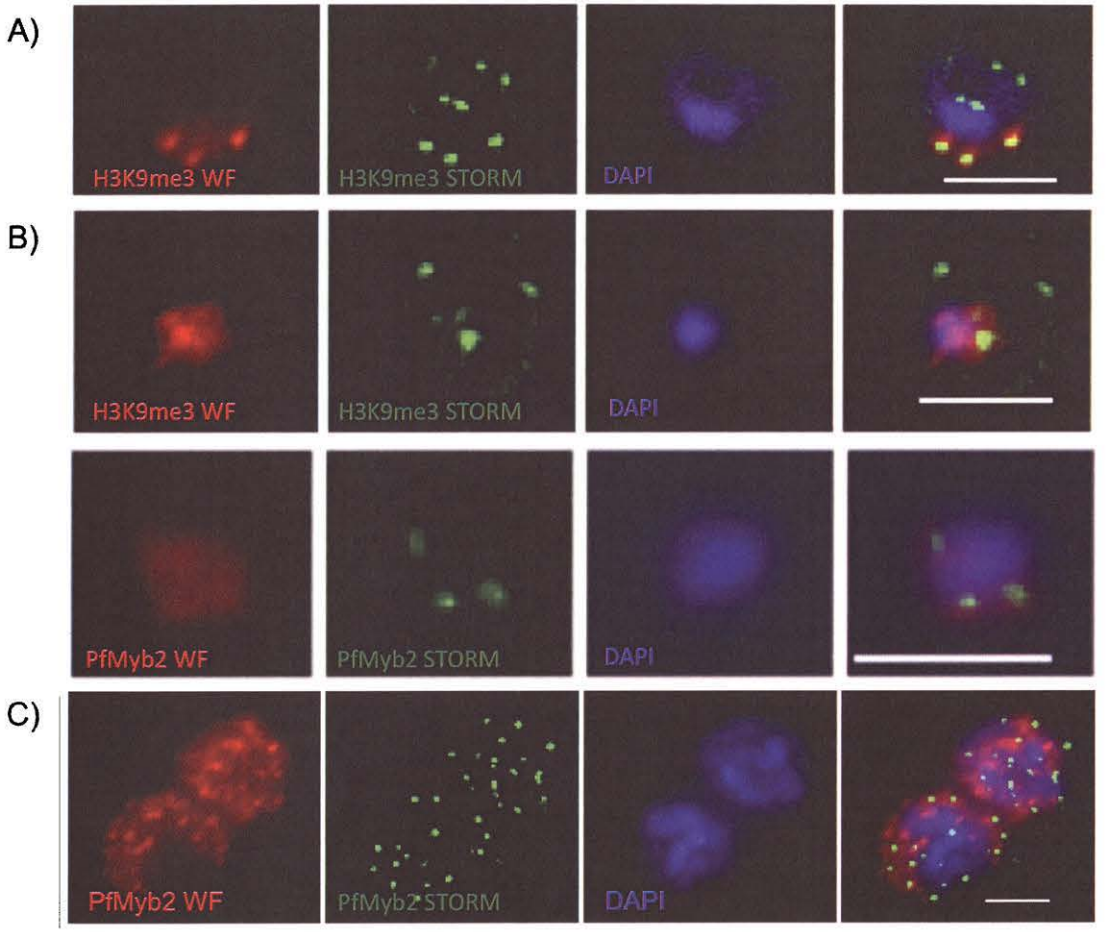

Figure 2.21: STORM imaging of *P. falciparum* nucleus. Representative results of super-resolution imaging of H3K9me3 and PfMyb2. Montages show the wide-field image (WF) of H3K9me3 or PfMyb2 (red) overlaid with the STORM reconstruction image (green) and DAPI signal (blue). Scale bars =3 μm. STORM reconstruction resolution =80-100 nm.

During STORM image acquisiton, the fluorophores in each sample were stimulated to cycle through the light and dark states, but they did so at sub-optimal rate, such that a high level of background signal remained in each sample throughout the imaging protocol. STORM reconstructions of the acquired images produced granular representations of the relevant label, with some discrepancies evident between the

wide-field images and the STORM reconstructions. In some cases, such as multiple perinuclear H3K9me3 foci (Figure 2.21A), although the two images correlate closely to each other, the STORM reconstruction shows some regions of signal that are not detected in the wide-field image. In the case of more diffuse target labeling (Figure 2.21B), the majority of the signal shown in the wide-field image is not detected by the STORM technique. The STORM reconstruction rather reveals the organisation of a few select nuclear-associated signal foci, consisting of a limited number of single objects. Striking labeling patterns (Figure 2.21C) were observed for mature-stage parasites, in which STORM reconstructions show a large number of single signal foci distributed between the nuclei of the schizont, corresponding to the surface labeling of PfMyb2 detected. Interestingly, even in such cases, full co-localisation of the wide-field and STORM signals was seldom detected; STORM foci appear consistently spatially detached from the wide-field image.

2.4. Discussion

Fluorescent microscopy offers a rich platform from which to investigate the spatial organisation of factors of interest, and to tease out functional information regarding relative organisation within the *P. falciparum* parasite nucleus. Work in this chapter focused on the establishment and optimisation of a number of fluorescent labeling techniques for the detection of nuclear molecules of interest in *P. falciparum* parasites, with the requirement that they be sensitive, specific, reliable and reproducible if they are to be used in a high-content imaging approach for the study of nuclear organisation.

Sample preparation plays an essential role in any fluorescent microscopy assay of *P. falciparum* (Figure 2.2A) to preserve sample integrity and allows the establishment of fluorescent assays with minimal autofluorescence or signal interference from the sample itself. The optimal conditions determined in this chapter for parasite washing and RBC lysis conditions differ from those in the protocol provided by Mancio-Silva (personal correspondence, 2009), but are in agreement with conditions recommended by Contreras-Dominguez *et al.* (2010) for the improved preservation of nuclear

structure (Figure 2.3). In contrast, the extended fixation time reported by Contreras-Dominguez *et al.* (2010) to better preserve the sample was shown here to degrade samples (Figure 2.4A). These discrepancies may be due to a number of reasons, such as differences in buffer composition or pH, or the age of fixative used (Eltoum *et al.*, 2001). The inclusion of glutaraldehyde in fixation is often avoided in fluorescent microscopy due to it frequently contributing autofluorescence to the sample, and is contrary to both the above protocols. In this chapter, however, no additional autofluorescence is observed with the very low concentration glutaraldehyde used, and the superior sample preservation attained is essential for the integrity of results from harsher labeling protocols such as FISH (Figure 2.4B).

Direct IF was tested as an approach for the labeling of specific nuclear targets that would allow multiplex target labeling with a greater number of antibodies, as well as allow greater resolution when imaging with STORM. However, the loss of antibody specificity following antibody-fluorophore conjugation reactions (which may be due to a number of reasons including poor antibody-fluorophore conjugation efficiency, antibody damage or change in binding specificity due to the presence of the label) (Figure 2.11) meant that the use of directly labeled primary antibodies could not be implemented here. Although this limited our capacity for multiplexed labeling, indirect IF labeling was successfully established, as per Mancio-Silva *et al.* (2008a).

When used in conjunction with the sample preparation protocol established in this chapter, indirect IF allowed the specific and sensitive labeling of H3K9me3, H3K9ac, PfMyb2 and RNAPII, for the detection and differentiation of nuclear regions of transcriptional repression and activation (Figure 2.7). H3K9me3 and H3K9ac labeling each produced the expected signal distributions as based on published labeling data (Ralph *et al.*, 2005; Volz *et al.*, 2010). Neither PfMyb2 nor RNAPII IF labeling has been previously shown in the literature, but their detected perinuclear signals may be similar to published BrUTP incorporation data (Mancio-Silva *et al.*, 2010), strengthening the expectation that these two labels might associate with regions of active transcription and RNA processing (Figure 2.2B). Thus the establishment of PfMyb2 and RNAPII labeling here provides new markers for the spatial organisation of nuclear factors potentially involved in transcriptional activity. These indirect IF assays produced labeling results in most cases clearer than what has been reported before (i.e. Issar *et al.*, 2009, Lopez-Rubio *et al.*, 2009, Volz *et al.*, 2010), and

labeling of each of the established nuclear protein targets used could thus be carried out with the appropriate secondary antibodies to allow dual labeling assays for a high-content imaging approach as described in Chapter 3. In addition, each of these IF labels displayed a variability in its nuclear labeling patterns, the extent of which will be addressed in Chapter 3.

In addition to IF labeling, the establishment of FISH detection of *var* loci allows the nuclear detection of known genomic regions of transcriptional repression. The optimised conditions correspond to those used by Mancio-Silva *et al.* (2008b), producing comparable FISH results for *var* labeling to those shown in the literature (Ralph *et al.*, 2005; Mancio-Silva *et al.*, 2008b) (Figures 2.2C and 2.16). This protocol is thus suitable for application in dual labeling and high-content imaging in Chapter 3, allowing the labeling patterns of other target molecules to be related to this extensively studied gene family.

BrUTP incorporation labeling and smFISH assays both have great potential to reveal information regarding the spatial organisation all active transcription, and of specific gene loci and their transcripts as they are actively transcribed, respectively. Specifically, they may reveal whether or not particular gene loci, particulary non-antigen encoding genes, and their transcripts are confined to specific regions of transcriptional activity or repression within the parasite nucleus depending on their transcriptional activity. However, despite the fact that both BrUTP incorporation labeling and smFISH had been previously established for use in *P. falciparum* parasites (Griffiths, 2009; Mancio-Silva *et al.*, 2010), here neither assay satisfactorily reproduced those labeling results even after further optimisation of various experimental conditions (Figures 2.12 and 2.20). Although much scope remains for further optimisation of these protocols for use in *P. falciparum*, neither technique is suitable for a high-content imaging approach at this stage. Work on these assays was thus halted in favour of progressing with the established labeling assays that do provide sensitive and specific detection of other nuclear molecules of interest.

Similarly, both NPC and nucleolar labeling has been demonstrated for *P. falciparum* in the literature (Issar *et al.*, 2009; Mancio-Silva *et al.,* 2010), although this was achieved with plasmodial-specific antibodies. A similar parasite-specific anti-PfNup1 antibody was tested here, but although some clear NPC signal, consistent with the

reported nuclear distribution of NPCs in the parasite (Weiner *et al.*, 2011) (Figure 2.8A), was initially obtained, the rapid loss of antibody specificity for the nuclear target, perhaps due to antibody instability under the storage conditions used, rendered this assay ineffective. Likewise, the lack of sufficient cross-reactivity between commercial anti-fibrillarin antibodies and the parasite protein prevented the establishment of a specific nucleolar assay in the parasite (Figure 2.9). The detection of these two nuclear landmarks would have been required for the establishment of a co-ordinate system in a nuclear mapping strategy as demonstrated by Berger *et al.* (2008). Although, without these labels, such a strategy is no longer available in this work, an alternative high-content imaging approach is adopted to study the variability detected in the nuclear distribution of the targets in Chapter 3.

The establishment of STORM in *P. falciparum* opens up opportunities for the study of the investigation of sub-diffraction organisation of factors involved in nuclear architecture and *Plasmodium* biology. STORM imaging in *P. falciparum* has, to my knowledge, not yet been demonstrated in the literature. This may be due to challenges unique to *P. falciparum* microscopy. The slow blinking of fluorophores in the IF-labeled parasite samples during STORM aquisitions limits the detection and localisation of a significant proportion of the sample fluorophores (Figure 2.21). Although a number of imaging or sample conditions may affect fluorophore blinking, one potential explanation for poor blinking in the parasite may be that extended illumination with high intensity light, as required for STORM, leads to a pH change in the parasite intracellular environment. Wissing *et al.* (2002) demonstrated that illumination of live parasites resulted in cytosol acidification by damage to the food vacuolar membrane. Although not shown in the available literature, if a similar acidification process occurred in fixed parasites, the subsequent change in redox potential within the sample would account for the reduced fluorophore cycling between light and dark states (Heilemann *et al.*, 2009), producing sub-optimal STORM results. Further optimisation of the buffering system in the imaging medium can yet be carried out for STORM in *P. falciparum*. That said, in its current form this technique still holds potential for the elucidation of finer, sub-diffraction organisations or target molecules within the nucleus. For example, the distinct foci detected by STORM within the diffuse wide-field signal may represent more condensed clusters within the broader distribution of target molecules. Thus, despite

the sub-optimal fluorophore modulation, STORM imaging may serve a complementary role to a high-content imaging study of *P. falciparum* nuclear architecture for the uncovering of such features and their function.

The need for extensive optimisation of each of the protocols used in this chapter, and the experimental barriers to establishing certain assays such as BrUTP incorporation and smFISH, highlights some of the technical challenges of working with *P. falciparum.* It is not always possible to simply adapt protocols established in another organisms for use in the complex parasite and even assays previously established for the parasite in other labs- particularly microscopy assays, where artifacts may be easily introduced and labeling results may be subjectively interpreted- require verification and optimisation of experimental conditions to ensure the validity and specificity of the signals observed.

2.5. Conclusion

In this chapter, several fluorescent labeling techniques have been tested for use in *P. falciparum,* and specific nuclear labeling assays for selected potential markers for regions of transcriptional activation and repression have been established. Firstly, sample preparation and fixing was optimised for efficient sample preservation with minimal autofluorescence or debris, suitable for use with all subsequent labeling assays. Secondly, IF labeling was established allowing specific and sensitive indirect labeling of H3K9me3, H3K9ac, PfMyb2 and RNAPII, and thirdly, DNA-FISH was established. Lastly, STORM imaging was applied as a new technique in *P. falciparum.*

In Chapter 3, the optimised techniques described above will be applied and each of the labeling assays established in this chapter will be used in high-content imaging assays. This allows the use of computational image analysis using a classification approach to investigate the relative organisation of each marker and variability in nuclear organisation.

Chapter Three

High-content microscopy of nuclear organisation and dynamics in *P. falciparum*

3.1. Introduction

P. falciparum makes use of several mechanisms for tight transcriptional regulation, with epigenetic factors and spatial organisition within the nucleus playing an important role in the process (Ralph *et al.,* 2005; Lopez-Rubio *et al.*, 2009; Salcedo-Amaya *et al.*, 2009). Current literature lacks extensive studies of the relative organisation of each of these factors within the parasite nucleus. Without the ability to image large numbers of dual labeled nuclei, simplistic models of the parasite nuclear organisation have been put forward featuring a rather static organisational system (ie Lopez-Rubio *et al.*, 2009; Volz *et al.*, 2010).

There is, however an implicit need for dynamic regulation and organisation of gene loci and transcriptional activity on a spatial level. As observed with the transcription dependent relocalisation in the case of *var* loci, the bulk of gene loci must be able to move in and out of a limited number of transcription foci (Ralph *et al.*, 2005; Mancio-Silva *et al.*, 2010). Requisite chromatin remodeling for such events, as well as shifting histone modifications during progression of the parasite's IDC (Salcedo-Amaya *et al.*, 2009) all point towards a significantly dynamic nuclear organisation, albeit one that has not yet been directly described in the literature, due in part to under-sampling of the organism such that only a limited view of spatial organisation is detected. In the absence of live-cell imaging capabilities for *P. falciparum* parasites, we have proposed that the labeling and imaging of the nuclear organisation of many fixed nuclei may reveal any significant global shifts in nuclear architecture as variable labeling patterns within a single IDC stage and sample.

In chapter two, a number of fluorescent labeling techniques were established and optimised, allowing for specific labeling of H3K9me3 and H3K9ac (transcriptionally repressive and activating markers, respectively) (Lopez-Rubio *et al.*, 2007; Lopez-Rubio *et al.*, 2009, Salcedo-Amaya *et al.*, 2009), PfMyb2 transcription factor and elongating RNAPII, as well as the bulk of the *var* gene family loci. In this third chapter, high-content imaging has been used to determine which of these markers

might be most instructive for the general distributions of transcriptionally active and repressive regions within the nucleus. Here, the nuclear labeling patterns of each marker, individually, and subsequently in conjunction with additional markers of transcriptional activation and repression, have been assessed by extensive single- and dual labeling assays of each of these markers. Large data sets were generated by the use of large samples of synchronous *P. falciparum* parasite cultures, representing parasites from multiple time-points throughout the ring-stage of the parasite IDC, and bespoke computational image analysis was used to generate quantitative data of observed trends in nuclear organisation.

3.2. Materials and Methods

3.2.1. *P. falciparum in vitro* cultures and sample fixation.

P. falciparum cultures were maintained as described in section 2.2.1. Tightly synchronised cultures were obtained by routine treatment of ring-stage cultures to three sorbitol synchronisation processes, spaced 4 hours apart. Samples of ring-stage *P. falciparum* cultures were chemically fixed using the optimised fixation protocol described in section 2.2.2.

3.2.2. Immunofluorescence

Coverslips were cleaned and coated with 0.01% (w/v) PLL, as described in sections 2.2.3 and 2.2.4. Indirect IF labeling was carried out as described in section 2.2.5, using many of the same antibodies (Table 3.1). When a biotinylated secondary antibody was used it was labeled using 0.05mg/ml ATTO565-, ATTO647- or ATTO647N- conjugated streptavidin. Dual labeling IF was carried out by incubating samples with both appropriate primary antibodies simultaneously, followed by simultaneous incubation with appropriate secondary anitbodies if they do not cross-react (i.e. goat-anti-mouse antibodies with either goat-anti-rabbit or rabbit-anti-chicken antibodies). Sequential incubations were used with secondary antibodies that

would cross react (i.e goat-anti-rabbit antibodies were used before rabbit-anti-chicken antibodies).

Table 3.1: Primary antibodies and corresponding secondary antibodies used in IF labeling of nuclear targets. The appropriate secondary antibodies used for detection of the indicated primary antibody are listed next to each primary antibody.

Primary Antibodies				**Secondary Antibodies[3]**		
Antigen	**Host**	**Supplier**	**Dil. used[2]**	**Host**	**Reactivity**	**Label**
H3K9me3	Rabbit	Millipore	1:500	Goat	Rabbit IgG[a]	AlexaFluor532
				Goat	Rabbit IgG	ATTO488
				Goat	Rabbit IgG	ATTO647N
H3K9ac	Rabbit	Millipore	1:2000	Goat	Rabbit IgG[a]	AlexaFluor532
				Goat	Rabbit IgG	ATTO488
				Goat	Rabbit IgG	ATTO647N
RNAPII	Rabbit	Cell Signalling	1:50	Goat	Rabbit IgG	ATTO647N
				Goat	Rabbit IgG	ATTO488
				Goat	Rabbit IgG	ATTO647N
H3K9me3	Mouse	Abcam	1:100	Goat	Mouse IgG	ATTO488
H3K9ac	Mouse	Sigma Aldrich	1:750	Goat	Mouse IgG	ATTO488
PfMyb2	Chicken	Non-commercial[1]	1:100	Rabbit	Chicken IgY	TMR
				Rabbit	Chicken IgY	FITC
				Rabbit	Chicken IgY	Biotin

(1) Coetzer lab, University of Witwatersrand
(2) Dil. used: Dilution used
(3) Each secondary antibody was used at 1:500 dilution. Secondary antibodies denoted by ([a]) were supplied by Invitrogen, all other secondary antibodies were supplied by Rockland.

3.2.3. DNA-FISH and IF-DNA FISH

DNA-FISH labeling of *var* genes was carried according to the optimised protocol described in section 2.2.9. Hybridised biotinylated FISH probes were labeled using 0.05 mg/ml ATTO565-, ATTO647- or ATTO647N-conjugated streptavidin. Dual labeling with IF and FISH was carried out as by sequential IF labeling, followed by brief sample fixation, then FISH labeling, as in Mancio-Silva *et al.* (2008a). IF is carried out prior to FISH labeling as the formamide used during FISH hybridisation and washing may damage the epitopes that are recognised by antibodies, such that they cannot bind their target molecules. Fixation is required between the IF and FISH protocols in order to retain the antibody bound in the sample; the high temperatures used in DNA-FISH can otherwise denature antibodies such that they no longer bind to their target molecules and are lost during washing for FISH. IF was carried out as

described in sections 2.2.5 and 3.2.2, followed by fixation of the sample with 4% PFA and 0.025% glutaralderhyde in 1x PBS at 4°C for 30 minutes. Following three wash steps with 1x PBS, DNA-FISH was carried out as described in section 2.2.9 on the same samples.

3.2.4. Epifluorescent Microscopy

Imaging was carried out using a custom built Nikon Eclipse Ti inverted fluorescent microscope, with a 100x, 1.49 NA oil immersion objective. Images were captured using an Andor 897 iXion EMCCD camera (Andor, Belfast, UK). The microscope was controlled using μManager open source microscope management software (NIH and UCSF, USA). A 50-millisecond exposure time was used for DAPI. Exposure times ranged between 200 milliseconds and 1.5 seconds for other signals. Semi-automated image acquisition was set up for a high number of samples. This involved a mosaic of images being acquired across a manually selected region of the sample coverslip, with a 10 μm overlap between fields of view. Each field of view was captured as a series of images acquired on multiple focal planes through the sample, across a range of 2-10 μm in the axial plane. A 0.2 μm piezo step-size was used for these z-stacks.

3.2.5. Computational Image Analysis

Manual image processing and inspection was carried out as described in section 2.2.13. Further analysis was carried out by a computational approach. A supervised classification algorithm, written in MATLAB, was developed by Rethabile Kuthlang (Mhlanga lab, CSIR, Pretoria). It was used to assign signals detected by the algorithm to different classes, determined by the user. Briefly, in each z-stack image, nuclei are detected in different focal planes by a hierarchical K-means algorithm. Nuclear target signals were detected using spot-detection algorithms based on discrete wavelet transforms and assigned to user-determined classes. The algorithm was also able to determine signal correlations and co-labeling between channels, such that population distributions and significant spatial organisation trends and changes with time could be determined. The algorithm output was manually inspected for a small subset of

imaging data, to confirm the correct detection and classification for each class. Further information regarding this processing is available in Appendix B.1. STORM imaging and analysis was carried out as described in section 2.2.14.

3.2.6. Statistical analysis

Analysis of time course data made use of two statistical tools. Chi-square analysis was used as a measure of significance of the changes in nuclear label distribution across the ring-stage. Euclidean norm values were used as measures of multi-dimensional "closeness" between two sample sets. Norms were determined between each pair of label distributions obtained for each nuclear label, such that the closeness of the data at each time-point to that at each other time-point, as well as the data representing the full span of the ring-stage, was calculated. Based on closeness values of subsets of labeling data from earlier experiments, known to represent the same sample populations or different populations, threshold values of the Euclidean norm were determined for "close" (not significantly different), as less than 0.2; moderately different ("not close") data sets, indicated by norm values between 0.2 and 0.4; as well as grossly different data sets, determined by norm values greater than 0.4.

3.3. Results

3.3.1. H3K9me3 and H3K9ac labeling patterns are variable within the ring-stage nucleus.

IF labeling of the repressive histone mark H3K9me3 was carried out in ring-stage parasites, maintained with a synchronisation window of ~6 hours such that samples were considered representative of a mixed-age population of parasites spanning the bulk of the ring-stage of the IDC. Computational image analysis registered and processed 3399 of 4000 nuclei, indicating highly reproducible variation in the staining pattern of H3K9me3. This included 1) one or two perinuclear foci; 2) three or more foci distributed around the nuclear periphery; or 3) diffuse nuclear-internal signals occupying either a small portion or the full region of the nuclear signal (Figure 3.1A).

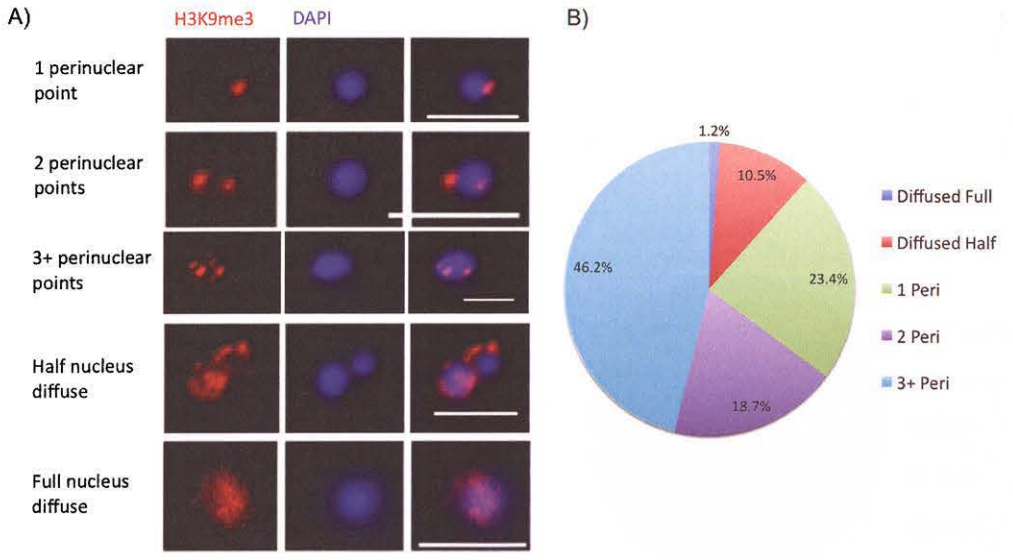

Figure 3.1: High-content IF assay of H3K9me3 results in variable labeling patterns. A) Representative images from high-content anti-H3K9me3 (red) imaging. Nuclei were labeled with DAPI (blue). Scale bars =3 μm. IF labeling of 6 biological replicates was carried out as 6 technically independent labeling assays for each label. Images of over 4000 nuclei were acquired. Images from all replicates were analysed as two subsets to determine average values for (B) a pie chart presenting the percentages of sampled ring-stage nuclei displaying each label distribution pattern for H3K9me3. $n_{(H3K9me3)}$=3399 nuclei.

H3K9ac labeling was optimally detected for 3295 out of over 4000 nuclei imaged and also showed a similar variation as above. Adopting the same classification approach as with H3K9me3, H3K9ac labeling patterns could be grouped by the same categories as used with H3K9me3, with either one, two, or multiple (three or more) perinuclear signal foci, or as diffuse signal occupying a sub-portion or full volume of the nuclear interior (Figure 3.2A). Imaging data for both H3K9me3 and H3K9ac were subjected to a bespoke supervised-learning image analysis algorithm, as described in section 3.2.5, such that the algorithm itself was able to detect and automatically classify the thousands of nuclei into the determined categories (Figures 3.1B and 3.2B).

H3K9me3 labeling is predominantly detected as multiple perinuclear foci (46%), while together, one and two perinuclear points constitute labeling for another 42% of the population. Likewise, the greatest proportion of H3K9ac signal is made up of

three or more detected foci (38%). Diffuse signals throughout the nuclear volume constitute only a small proportion of detected signals for both H3K9me3 and H3K9ac.

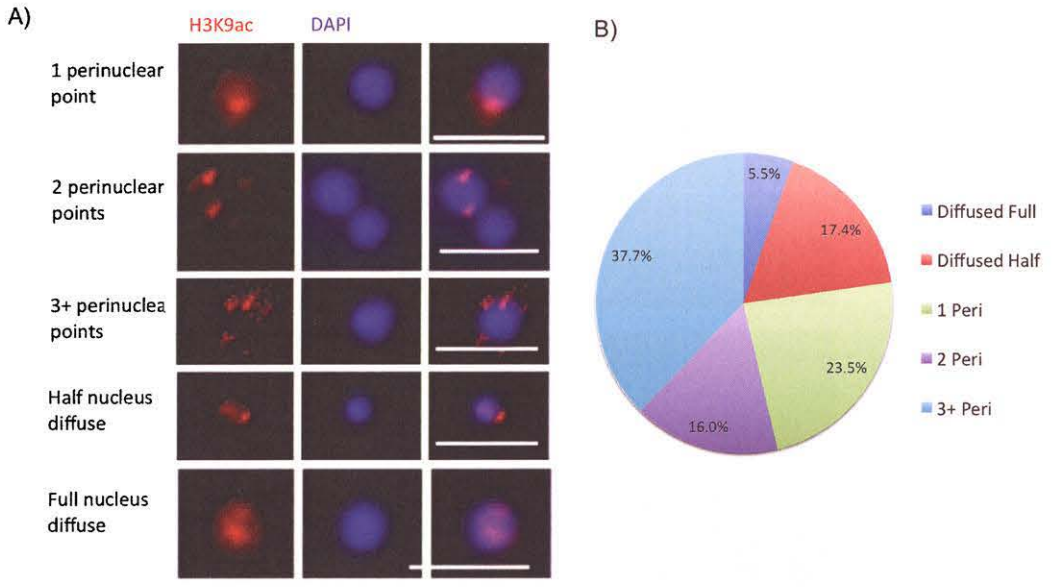

Figure 3.2: High-content IF assay of H3K9ac results in variable labeling patterns. A) Representative images from high-content anti-H3K9ac (red) imaging. Nuclei were labeled with DAPI (blue). Scale bars =3 µm. IF labeling of 6 biological replicates was carried out as 6 technically independent labeling assays for each label. Images of over 4000 nuclei were acquired and analysed as two subsets to determine average values for (B) a pie chart presenting the percentages of sampled ring-stage nuclei displaying each label distribution pattern for H3K9ac. $n_{(H3K9ac)} = 3295$ nuclei.

In order to provide biological context to the observations above, the two histone marks, acetylation and methylation should occupy differing and in general non-overlapping regions in the nucleus. The relative spatial organisation of H3K9me3 and H3K9ac within the nucleus was investigated by carrying out dual labeling of the histone modifications in ring-stage parasite samples. As expected based on the variable labeling detected for each marker on its own, the dual labeling distributions showed a large degree of variability (Figure 3.3). H3K9me3 was most frequently detected as perinuclear foci, with little signal overlap with either diffuse H3K9ac labeling (Figure 3.3A) or more punctate perinuclear H3K9ac signal (Figure 3.3B). While more extensive signal overlap was observed in the small number of nuclei where both labels were diffuse (Figure 3.3C), H3K9me3 and H3K9ac signals were observed as distinct from each other in the majority of other cases. The frequent

detection of H3K9ac and H3K9me3 signal in spatially distinct regions strengthens confidence in the variable patterns detected as true histone modification signal and shows that the activating and repressing marks are independenetly localised.

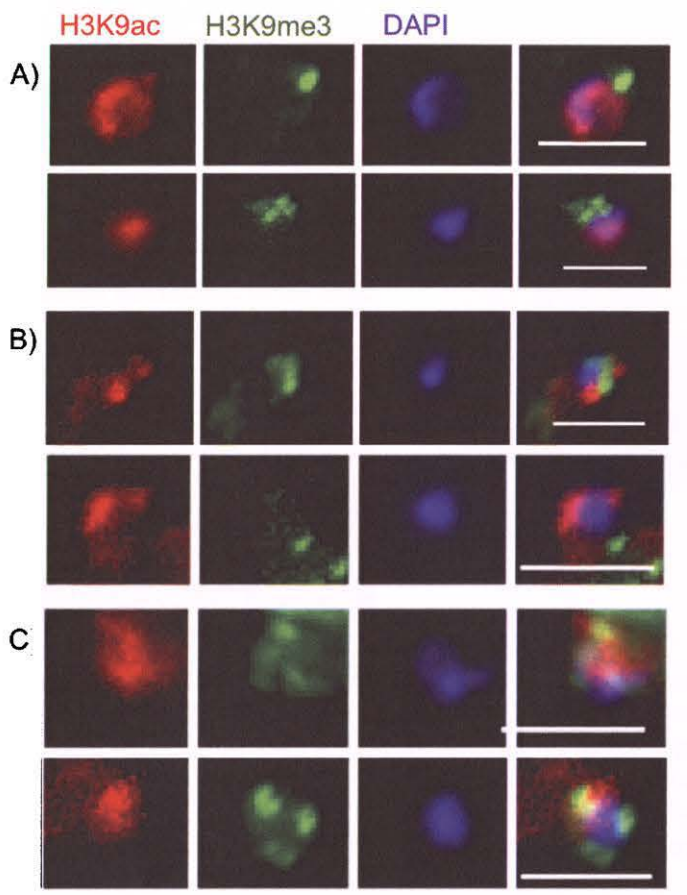

Figure 3.3: IF dual labeling of H3K9me3 and H3K9ac. Representative figures of dual labeling IF assays for H3K9me3 (green) and H3K9ac (red) in ring-stage nuclei. Nuclei were labeled with DAPI (blue), showing distinct signals in which H3K9ac is diffuse (A) or perinuclear (B), and C) signals with more extentsive overlap. Figures are representative of results obtained from 6 replicate experiments. Scale bars =3 μm.

3.3.2. Variable PfMyb2 labeling within the ring-stage of the parasite can be sorted into discrete classes.

The consistently high intensity signals obtained for PfMyb2 identify the labeling of the putative transcription factor as a suitable additional marker, with H3K9ac, for regions of active transcription potential, to be used for further investigation via high-content imaging and computational image analysis. PfMyb2 IF labeling was carried out on large sample sets of mixed-age ring-stage parasites, maintained with a

synchronisation window of ~6 hours. As with H3K9me3 and H3K9ac, the variable label patterns could be assigned to one of a number of qualitatively distinct classes or groups (Figure 3.4).

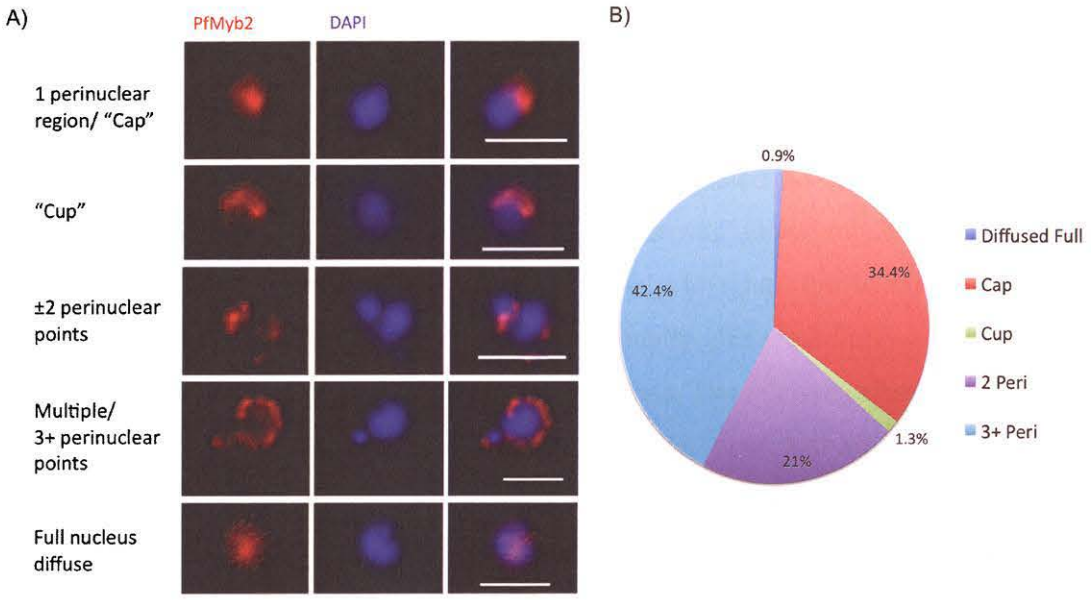

Figure 3.4: High-content IF assays of PfMyb2 results in variable labeling patterns. A) Representative images from high-content anti-PfMyb2 (red) imaging. Nuclei were labeled with DAPI (blue). Scale bars =3 μm. B) Pie chart presenting the percentages of the sampled ring-stage population of nuclei displaying each label distribution pattern for PfMyb2. Images for ~5000 nuclei were acquired during 10 technically independent labeling assays of 6 biological replicates. Images were pooled into two subsets and analysed to calculate the average values given. $n_{(PfMyb2)} = 4618$ nuclei.

Computational analysis registered and processed 4618 of ~5000 nuclei, displaying PfMyb2 signal as 1) a single perinuclear region, less condensed than the perinuclear foci observed for H3K9me3 or H3K9ac (termed "cap"), 2) a curved perinuclear signal (termed "cup"), 3) two or more perinuclear foci, or 4) diffuse signal occupying the full region of the nuclear signal (Figure 3.4A). It is worth noting that independent RNAPII labeling also displays similar labeling patterns, such as the "cup" and "cap" classes (shown in Appendix B.2, Figure B-1).

Computational analysis, as described in section 3.2.5, was used to automatically detect and classifiy the imaged nuclei into the label patterns determined (Figre 3.4B). The majority of PfMyb2 is detected as multiple perinuclear foci (over 42%), twice the proportion of nuclei with two perinuclear foci (21%). Another 34% of the population

displayed the cap pattern. Very few nuclei displayed the "cup" or diffuse labeling patterns (~1% each).

3.3.3. Dual labeling of H3K9me3 and H3K9ac with additional markers of transcriptional repression and activation reveals independent labeling patterns.

3.3.3.1. Dual labeling of H3K9me3 and H3K9ac with *var* loci

Following dual labeling of the acetylated and methylated histone H3K9 with each other, the spatial localisation of each histone mark was related to additional markers of transcriptional repression and potential activity to relate the variability detected with each label with that of other labels. Additionally, this would allow the continued investigation into nuclear spatial organisation trends. The relative organisation of both histone marks to that of constitutively repressed *var* gene loci was investigated by carrying out serial IF-DNA FISH labeling experiments against the *var* exon2 region and either H3K9me3 or H3K9ac, as described in section 3.2.3, in mixed-age ring-stage parasites.

Figure 3.5A shows representative images of the variable co-localisation trends obtained from the dual labeling of H3K9me3 and *var* exon2. The two signals were most frequently detected spatially distinct from each other, either 1) greatly separated (Figure 3.5A-1), 2) abutting and interweaving (Figure 3.5A-2) or 3) in a limited number of nuclei partial or full co-localisation between the two labels was detected (Figure 3.5A-3). Co-labeling with H3K9ac and *var* exon2 shows more regularly diffuse labeling for H3K9ac than was observed for H3K9me3 (Figure 3.5B). H3K9ac and *var* signals show 1) partial overlap (most often when H3K9ac signal is diffuse) (Figure 3.5B-1), 2) distinct perinuclear signals (Figure 3.5B-2) or 3) diffuse and overlapping signal, in a very small number of nuclei (Figure 3.5B-3).

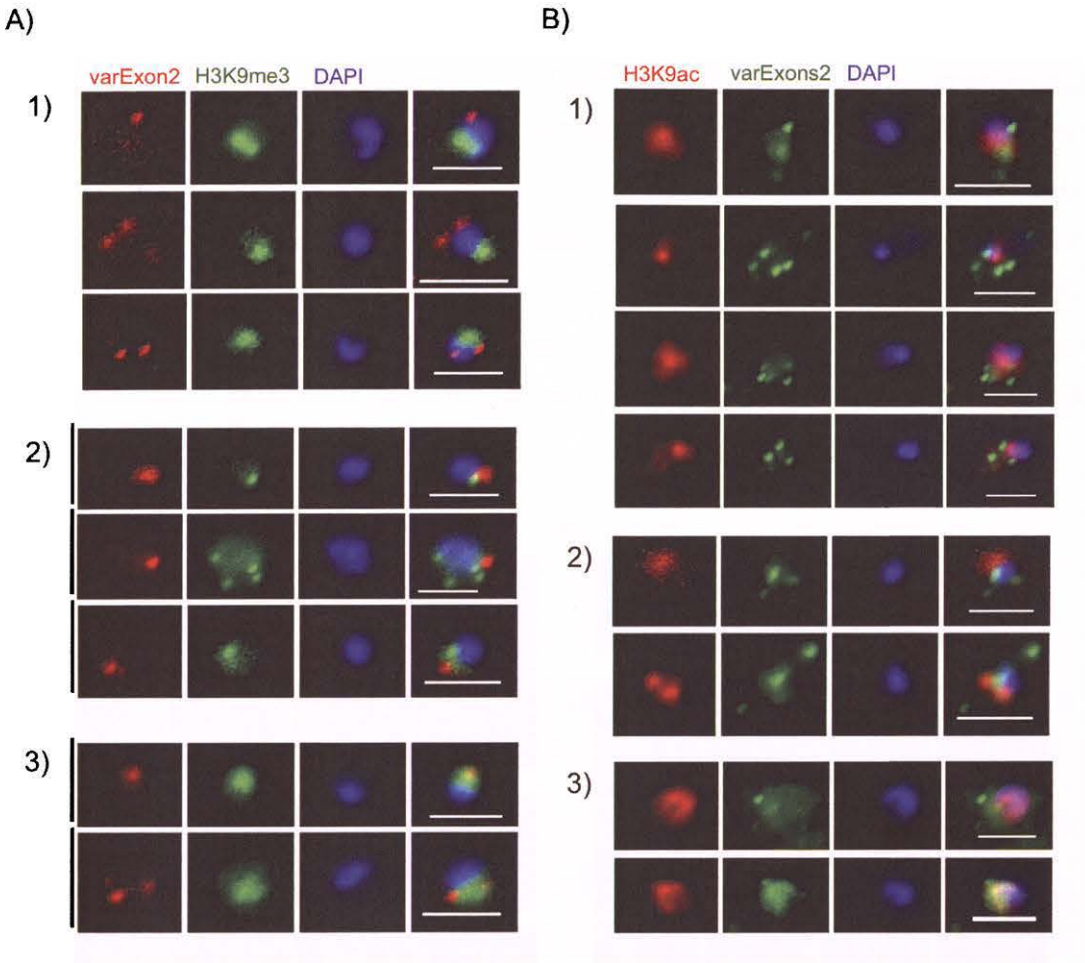

Figure 3.5: IF-FISH dual labeling of H3K9me3 and H3K9ac with *var* gene loci. A) Representative figures of dual labeling assay for H3K9me3 (green), showing 1) spatially discrete, 2) abutting or interweaving, or 3) full or partial co-localisation with the exon2 regions of *var* gene loci (red). B) Representative figures of dual labeling assay for H3K9ac (red) with the exon2 regions of *var* gene loci (green), showing 1) partial signal overlap between the diffuse H3K9ac and perinuclear *var* signals, 2) distinct perinuclear H3K9ac foci or 3) extensive signal overlap. Nuclei were stained with DAPI (blue). Figures are representative of results obtained from 4-5 replicate experiments. Scale bars =3 μm.

3.3.3.2. Dual labeling of H3K9me3 and H3K9ac with regions of active transcription.

In order to relate the acetylation and methylation marks to regions of the nucleus where the transcription machinery is actively engaged in making mRNA, mixed-age ring-stage parasites were labeled with antibodies for elongating RNAPII and the putative transcription factor PfMyb2 in different combinations with H3K9me3 and H3K9ac (Figure 3.6).

H3K9me3 and PfMyb2 signal localisation varied greatly, showing 1) perinuclear signals with full or partial co-localisation (Figure 3.6A-1), 2) distinct but interlocking perinuclear foci (Figure 3.6A-2) or 3) diffuse signal for either label that remains discrete and independent (Figure 3.6A-3). A similar range of pattern arrangements was observed with dual labeling of H3K9me3 and RNAPII (Figure 3.6B), with the majority of sampled nuclei displaying co-labeling signals of non-overlapping, independently patterning foci (Figure 3.6B-2). This relative localisation variability indicates that H3K9me3 nuclear organisation is independent of both PfMyb2 and RNAPII.

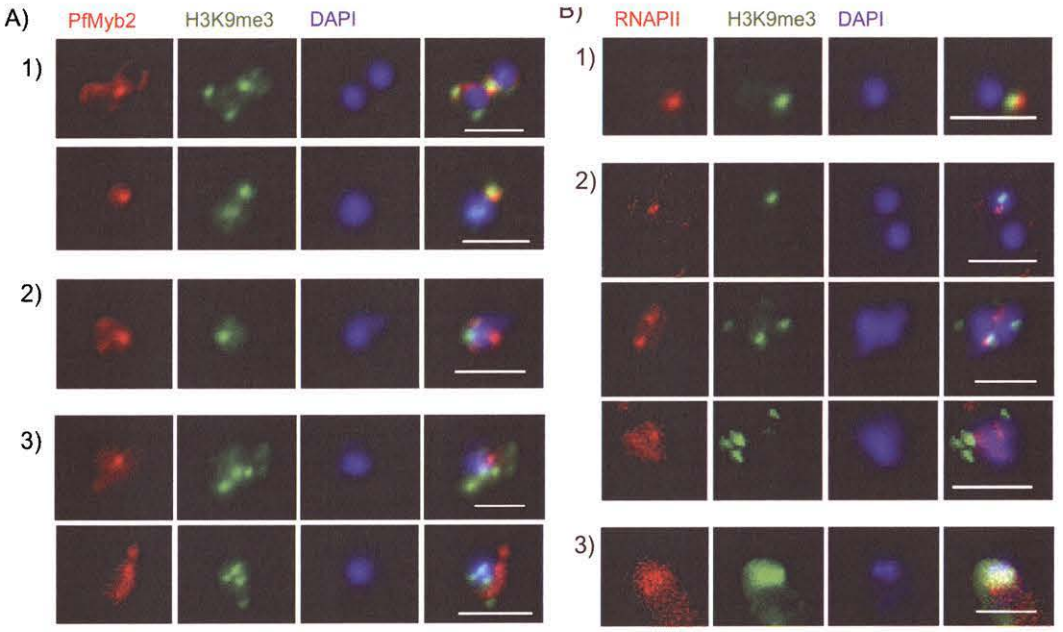

Figure 3.6: IF dual labeling of H3K9me3 with markers of transcriptional activity, PfMyb2 and RNAPII. Representative figures of dual labeling assays for H3K9me3 (green) with A) putative transcription and splicing factor PfMyb2 (red), and B) elongating serine-2-phosphorylated RNAPII (red). Nuclei were stained with DAPI (blue). In A) punctate or diffuse signals may partially or fully co-localise (1) or remain spatially distinct (2 and 3). In B) punctate signals may co-localise (1), remain spatially distinct (2) or diffuse signals overlap more extensively (3). Figures are representative of results obtained from 6 and 2 replicate experiments for A and B, respectively. Scale bars =3 μm.

Dual labeling of H3K9ac with each of the active transcription markers is shown in Figure 3.7, as well as co-labeling of RNAPII with PfMyb2. The nuclei dual labeled with H3K9ac and PfMyb2 displayed 1) often diffuse signals, with almost complete co-localisation (Figure 3.7A-1), 2) multiple perinuclear foci or diffuse regions with partial signal overlap (Figure 3.7A-2) or 3) adjacent but discrete diffuse or perinuclear

regions (Figure 3.7A-3). These trends indicate that H3K9ac and PfMyb2 may occasionally associate together, but are largely independently localised. Dual labeling results of H3K9ac with RNAPII, shown in Figure 3.7B, produced similar relative spatial arrangements to those seen with H3K9ac and PfMyb2, suggesting that H3K9ac and RNAPII are largely independently localised although they may occasionally be associated.

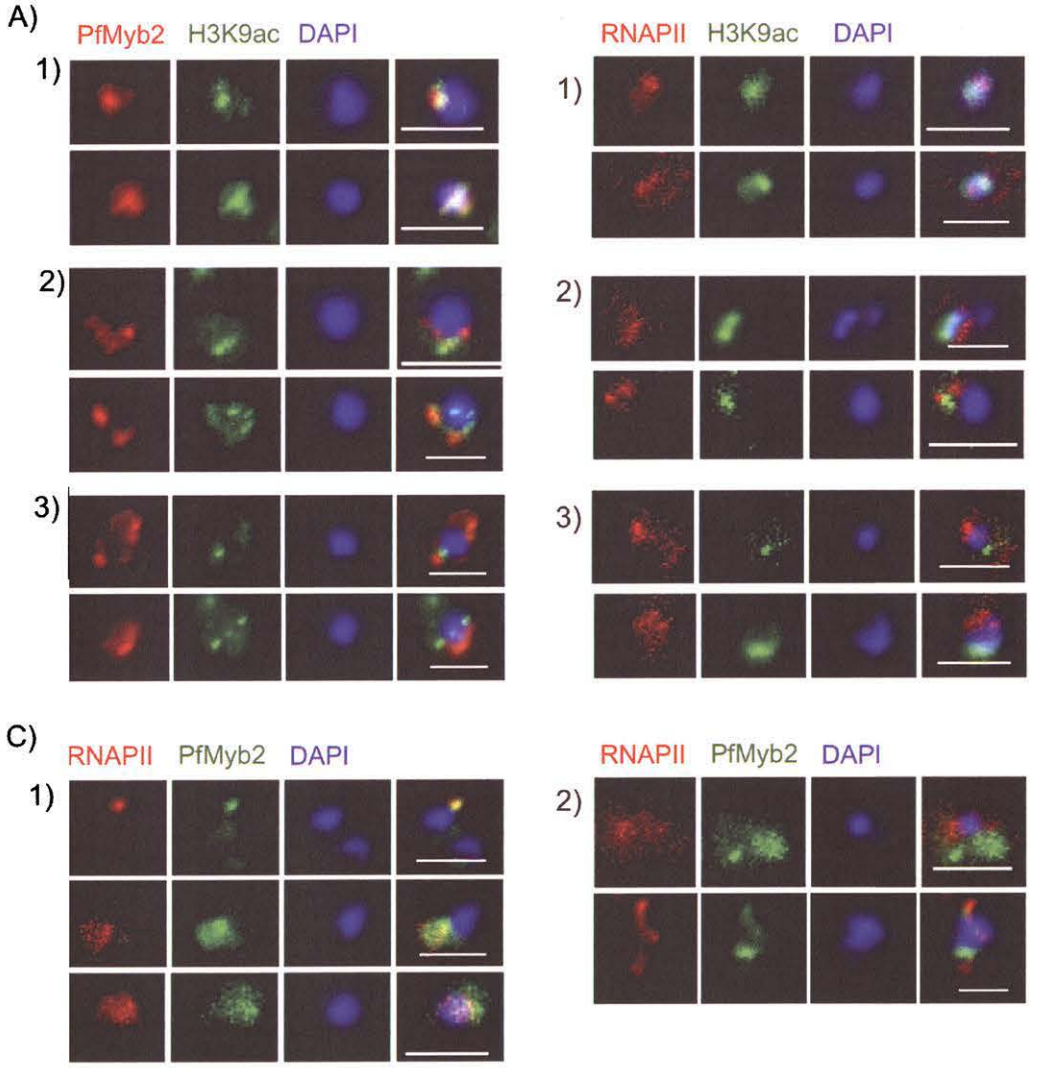

Figure 3.7: IF dual labeling of H3K9ac and markers of transcriptional activity, PfMyb2 and RNAPII in combination with each other. Representative figures of dual labeling for A) H3K9ac (green) with putative transcription and splicing factor PfMyb2 (red), and B) H3K9ac (green) with elongating serine-2-phosphorylated RNAPII (red), in which signals either fully (1) or partially (2) co-localised, or remained spatially distinct (3). C) Representative figures of dual labeling for RNAPII (red) with PfMyb2 (green), showing 1) signal co-localisation and 2) spatially distinct signal. Nuclei were stained with DAPI (blue). Figures are representative of results obtained from 6, 2 and 3 replicate experiments for parts A, B and C, respectively. Scale bars =3 μm.

Co-labeling of PfMyb2 with RNAPII was also carried out (Figure 3.7C). Signals for the two labels showed 1) a high level of signal overlap, particularly as the majority of nuclei displayed diffuse signals (Figure 3.7C-1), or 2) distinct, often adjacent, perinuclear labeling (Figure 3.7C-2). These trends suggest a higher degree of association for RNAPII and PfMyb2, although their frequent distinct localisations indicate functional differences between the markers.

3.3.3.3. Dual labeling of regions of active transcription with *var* loci

Following detection of the frequent spatial associations between PfMyb2 and RNAPII within the nucleus, further dual labeling IF-FISH experiments were carried out in order to determine the relative arrangements of these potential markers of transcriptional activity with the repressed *var* gene loci (Figure 3.8).

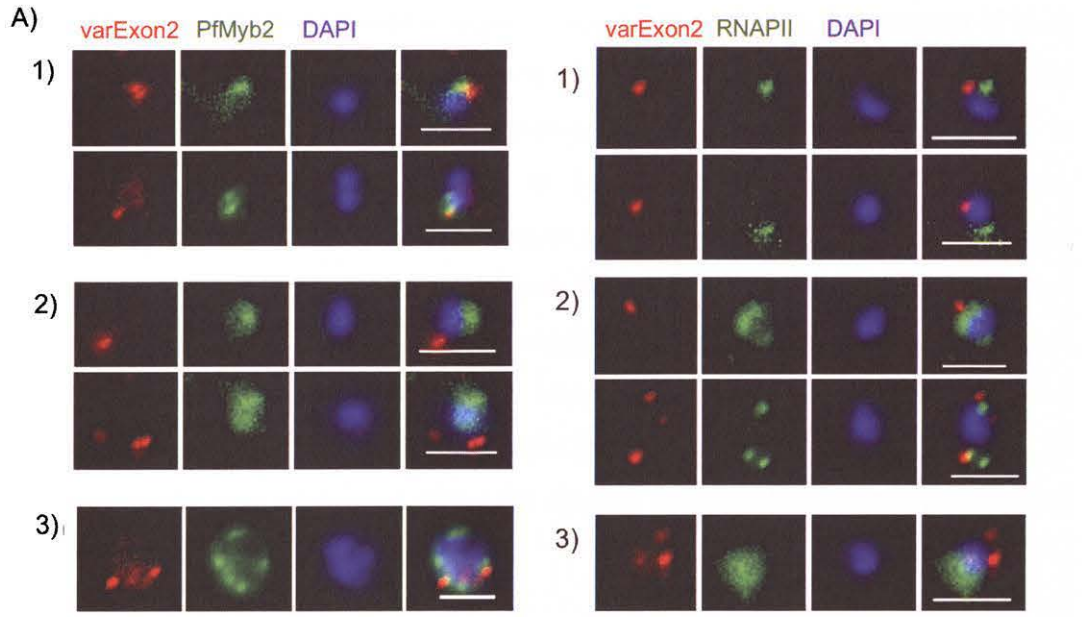

Figure 3.8: IF-FISH dual labeling of *var* gene loci with markers of transcriptional activity, PfMyb2 and RNAPII. Representative figures of dual labeling assays for A) PfMyb2 (green) with the exon2 regions of *var* gene loci (red), showing 1) signal co-localisation, 2) distinct signals, 3) co-localisation with diffuse PfMyb2 signal; and B) RNAPII (green) with the exon2 regions of *var* gene loci (red), showing 1) distinct signals, 2) adjacent signals with and without co-localisation, and 3) partial co-localisation with diffuse RNAPII signal. Nuclei were stained with DAPI (blue). Figures are representative of results obtained from 3-4 replicate experiments. Scale bars =3 μm.

Here, PfMyb2 signal is detected primarily as single perinuclear regions. Such PfMyb2 signals show either 1) full or partial co-localisation (Figure 3.8A-1) or 2) spatially distinct localisation (Figure 3.8A-2), with *var* perinuclear foci. 3) Diffuse PfMyb2 signal shows partial overlap with *var* foci at the nuclear periphery (Figure 3.8A-3). The majority of RNAPII signal shows 1) distinct localisation from *var* foci (Figure 3.8B-1), or 2) adjacent labeling that may remain distinct or partially overlap with *var* signal (Figure 3.8B-2). 3) More diffuse RNAPII signal may also partially overlap with var foci when it extends to the nuclear periphery (Figure 3.8B-3). The variable labeling patterns indicate that PfMyb2 and RNAPII are both organised independent of *var* localisation.

3.3.4. Computational image analysis of co-localisation assays of H3K9me3 and H3K9ac with PfMyb2

The existence of multiple possible organisational classes raises the question if there may be specific associations between particular spatial patterns of one label and that of other labels, such that specific combinations of label classes may occur in individual nuclei at particularly high or low frequencies within a population. Similarly, specific pairs of co-labeling classes may occur with a greater level of signal overlap or co-localisation than other pairs. H3K9me3, H3K9ac and PfMyb2 were selected as the nuclear targets most consistently labeled with high quality signal, and thus suitable for further computational image analysis. Results of dual labeling experiments of PfMyb2 with either H3K9me3 or H3K9ac were assessed by computational image analysis to detect the specific spatial patterns displayed for each label in individual nuclei (Figure 3.9).

Each of the histone modification labeling patterns were detected in combination with the full range of PfMyb2 label patterns, at varying frequencies that appear to broadly correspond to the frequency at which each independent label was detected in Figures 3.1-3.3 (Figures 3.9A and B). The multiple perinuclear foci pattern is dominant for both histone modifications, and is most frequently found in combination with multiple perinuclear PfMyb2 foci, followed by cap and two perinuclear foci labeling. One and two perinuclear H3K9me3 or H3K9ac foci occur most frequently in combination with PfMyb2 cap labeling, while diffuse half signal for both histone modifications is

primarily detected with multiple perinuclear PfMyb2 foci. In each case, detection of a histone modification class with each of the other PfMyb2 classes still constitutes a significant proportion of the nuclei detected with H3K9ac or H3K9me3 class.

Computational image analysis of co-localisation trends for each co-labeling pair determined the percentage of signal overlap between the two labels, and grouped the results obtained for each co-labeled nucleus into 5 categories: 0% co-localisation, where signals may be adjacent of fully distinct with no contact between the signals; 0.1% to 10% co-localisation, which describes signals that are adjacent, in contact and overlapping to a small degree, 10.1%-30% overlap constitutes partial co-localisation, while 30.1%-60% signal overlap and 60.1% to 100% overlap represents half and full co-localisation, respectively.

The majority of co-labeling for each labeling pair assessed occurs with no co-localisation, with the exceptions of diffused half H3K9me3 or H3K9ac with 2 or more perinuclear PfMyb2 labels (Figure 3.9C and D). The data for such a combination of H3K9me3 and PfMyb2 labeling is under-sampled and was not further assessed. However, the co-localisation for diffused half H3K9ac signal and 2 or multiple PfMyb2 signals is greatly skewed in favour of adjacent and partially overlapping signals. In general, half or full signal co-localisation is detected more frequently in label pairs combining condensed signal such as one or two perinuclear foci, with more extensive label classes, such as multiple perinulcear foci, cap signal, or diffuse signal.

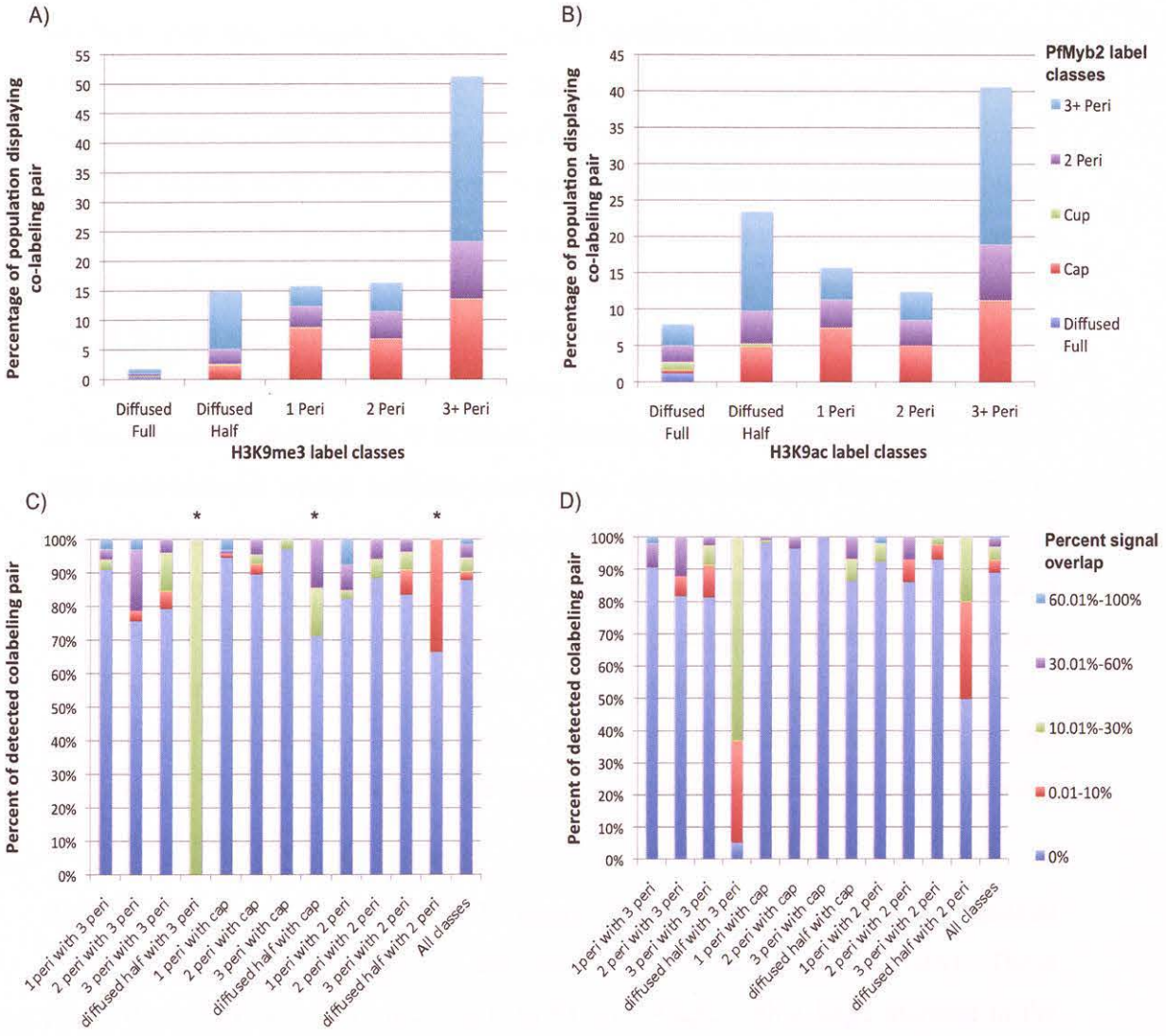

Figure 3.9: Distributions and co-localisation of PfMyb2 and H3K9me3 or H3K9ac class pairs in co-labeled samples. A and B: Histograms showing the frequency of the co-occurrence of particular (A) H3K9me3 or (B) H3K9ac label classes with each of the PfMyb2 label classes, in single nuclei. Charts are representative of pooled data from 6 replicate experiments. n(H3K9ac with PfMyb2) = 1969 nuclei, n(H3K9me3 with PfMyb2) = 2027 nuclei. C and D: Bar charts representing the degree of co-localisation of particular H3K9me3 (C) or H3K9ac (D) and PfMyb2 co-labeling pairs found to occur at higher frequencies. Percentage overlap was calculated as the percent of area of the label signal with a smaller area that was overlapping with signal from the other label. n(H3K9ac with PfMyb2) = 603 nuclei, n(H3K9me3 with PfMyb2) = 560 nuclei. Asterix (*) indicates bars representing fewer than 10 data points.

3.3.5. Time course ring-stage sampling and labeling of H3K9me3, H3K9ac and PfMyb2

Multiple different, independent and mutually exclusive nuclear organisations have been demonstrated for each the nuclear labels. One possibility that could account for such variability is that the different organisations are transient arrangements within a dynamic nuclear architecture. A single high-resolution time course experiment, using tightly synchronised parasites (4 hour synchronization window) was carried out to investigate the possibility of nuclear labeling diversity being dependent on time or the age of the parasite. Ring-stage parasites were isolated at three-hour intervals, starting ~2 hours post invasion (hpi) and continuing until ~20 hpi. Following labeling of each of the time-point samples for H3K9me3, H3K9ac and PfMyb2; fluorescent imaging and computational image analysis allowed the determination of the proportions of populations at each time-point displaying each of the labeling classes for each nuclear marker (Figure 3.10). Chi-square analysis of each time course data set was used to determine if the shifts detected in nuclear label distributions across the ring-stage could not be due to chance. In addition, the Euclidean norm, a measure of multi-dimensional "closeness", was determined between the label distributions obtained for each nuclear label at each pair of time-points. Each of these Euclidean norm values is given in Appendix C.1.

At early ring-stage, the majority of the sample population displays H3K9ac signal as either diffused half labeling or one perinuclear focus (Figure 3.10A). These proportions show a mildly significant shift from 14 hpi, with a large increase in the proportion of full diffuse labeling, at the cost of single perinuclear foci. These population distributions keep close to each other for the remaining time-points. It is interesting to note, however, that after occurring in a consistent proportion of parasites throughout earlier time-points, multiple perinuclear foci labeling is barely detected at 20hpi. The Euclidean norm between the samples at 2 hpi and 20 hpi (0.29) indicates a moderately significant difference in class distributions across the course of the ring-stage.

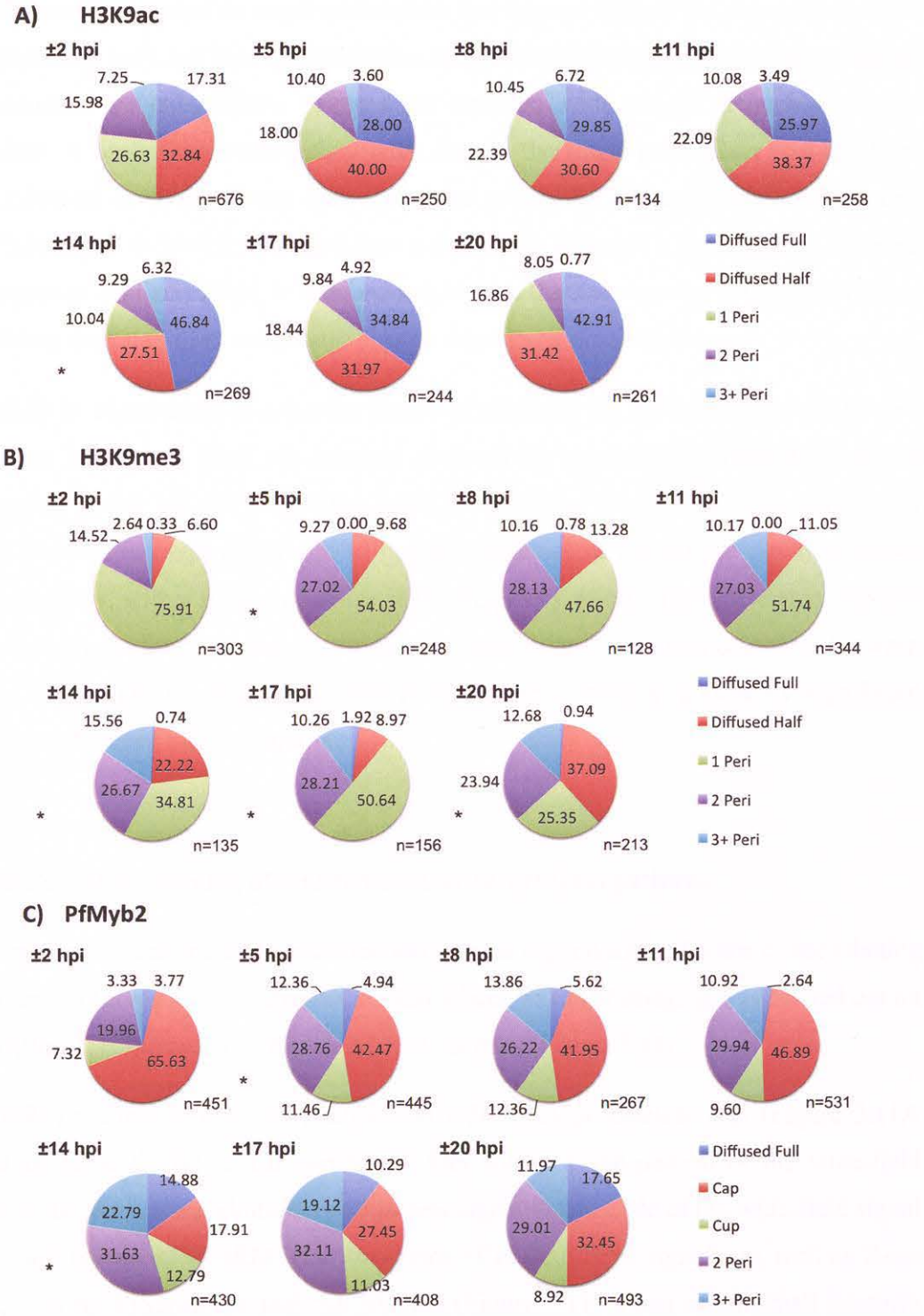

Figure 3.10: Time course labeling results for H3K9me3, H3K9ac and PfMyb2. Pie charts show the detected proportions of the sample populations displaying each of the labeling patterns indicated for A) H3K9ac, B) H3K9me3 or C) PfMyb2 at each time-point, as indicated. Time-points are given as the approximate hours post invasion (hpi). n represents the number of nuclei detected and processed by the algorithm for each of the labels at each time-point. $X^2_{(H3K9me3)}$ =224, $P < 0.001$. $X^2_{(H3K9ac)}$ =157, $P < 0.001$. $X^2_{(PfMyb2)}$ =157, $P < 0.001$. Asterix in between pie charts indicates a Euclidean norm for the two time-points of between 0.2 and 0.4.

H3K9me3 is detected as single perinuclear foci in over 75% of the youngest sampled parasites (2 hpi), but this representation decreases moderately by 5 hpi and multiple perinuclear or half diffuse patterns are detected with greater frequency (Figure 3.10B). A further moderately significant drop in the single perinuclear foci at 14 hpi is followed by a significant increase in the proportion of nuclei labeled with half diffuse signal at 20 hpi. The euclidean norm (0.61) indicates a gross change between samples at 2hpi and 20hpi. It is interesting to note that the very low rate of full diffuse labeling detection does not greatly change throughout the time course.

A shift in distribution of a similar nature is observed for PfMyb2 as for H3K9me3 (Figure 3.10C). At 2hpi, cap-labeling accounts for over 65% of PfMyb2 signal in sampled nuclei, but this proportion drops to 45% from 5 hpi as multiple perinuclear foci increase in frequency. From 14 hpi the frequency of full diffuse signal increases significantly, with a further decrease in the frequency of cap signal detection. Despite the seemingly drastic change in the relative proportions of signals displayed between 2hpi and 20hpi, the Euclidean norm (0.38) indicates only a moderately significant distance between the two samples.

3.3.6. STORM imaging of selected nuclear target label patterns

In order to investigate the sub-diffraction nuclear organisation of some of the labeling patterns observed for the different nuclear labels, STORM imaging was carried out on H3K9me3, H3K9ac and PfMyb2–labeled samples (Figure 3.11).

STORM reconstructions of H3K9ac and H3K9me3 perinuclear foci (Figure 3.11A and B, respectively) reveal correlating foci within a sub-portion of the wide-field signal. In some cases additional perinuclear signal foci outside of the wide-field signal area are revealed. STORM reconstructions of more diffuse signals, as well as those acquired for PfMyb2 cap and cup labeling (Figure 3.11C), can reveal small numbers of foci within the wide-field signal, as well as one or a few very small and faint signals detected outside of the wide-field image, at the nuclear periphery. These additional foci are often at a polar opposite from the wide-field image, or evenly spaced around the nuclear periphery.

The foci seen in these reconstructions provide information regarding the organisation of the nuclear targets within their wide-field foci. The individual molecules within these condensed foci cannot be quantified by the current approach.

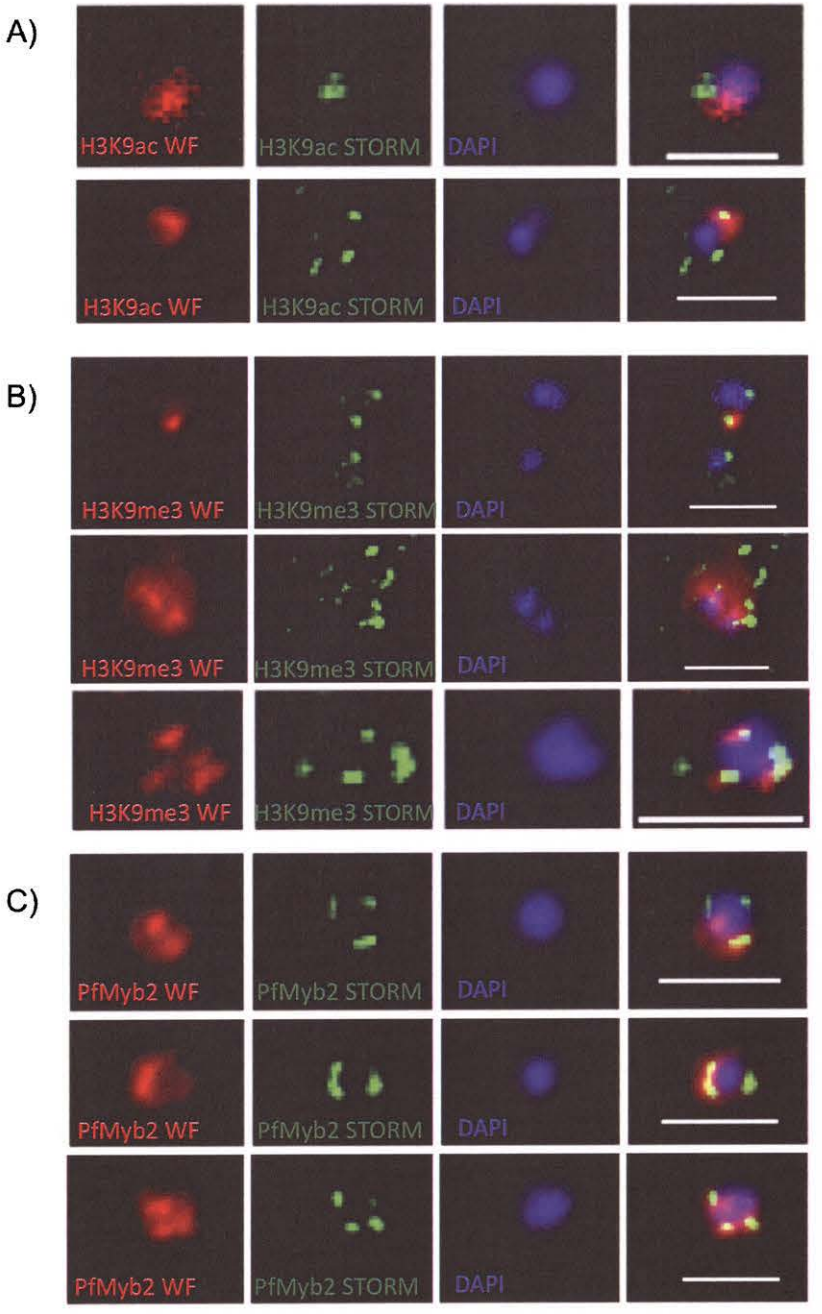

Figure 3.11: STORM imaging results. STORM imaging results are shown for selected signal patterns for A) H3K9ac, B) H3K9me3 and C) PfMyb2 IF labels. Reconstructions (green) of the indicated label are shown in conjunction with the wide-field images (red) and DAPI-labeled nuclei (blue). Approximate resolution of reconstructions =80-100 nm. Scale bars =3 μm.

3.4. Discussion

Applying the fluorescent labeling techniques and assays established in Chapter 2, in this chapter we have demonstrated the ability to sensitively and specifically label a very large number of fixed parasites and image them using a high-content fluorescent microscopy platform. This has allowed the study of the relative spatial organisation of selected markers of regions of transcriptional activity or repression and, coupled with bespoke computational image analysis, the investigation of the potential for greater dynamics in the nuclear architecture than currently presented in the literature.

Dual labeling assays revealed a number of trends in the relative organisation of the markers of transcriptional activity and repression. The variable relative localisation patterns observed between most of the nuclear targets indicated that in general, each of the targets were independently spatially organised from each of the others (with the exception of PfMyb2 and RNAPII labeling) as well as providing the first indications that *P. falciparum* nuclear organisation may not be as rigid and stereotyped as initially assumed. The spatially distinct labeling observed for repressive markers (H3K9me3 or *var* loci) with active markers (H3K9ac, PfMyb2 or RNAPII) (Figures 3.3, 3.5B, 3.6 and 3.8) provides a clear demonstration of the distinct compartmentalisation of euchromatin and heterochromatin, which has only previously been shown for *P. falciparum* by EM (i.e. Ralph *et al.*, 2005; Weiner *et al.*, 2011).

In contrast, the unexpected lack of association of signals for transcriptional repression markers H3K9me3 and *var* is in direct contradiction of the association of H3K9me3 with repressed *var* loci previously reported (Lopez-Rubio *et al.*, 2009). One may reason, however, that the result observed here is likely artefactual, due to over-stabilisation of the parasite telomeres by the binding of anti-H3K9me3 antibody combined with the additional cross-linking used in the IF-FISH assay. If this prevented access to the repressed var loci by the FISH probes, only binding of the probe to the single dissociated, H3K9me3-depleted *var* locus would be detected, which corresponds to the labeling results observed in this chapter (Figure 3.5A).

The high level of signal overlap observed with PfMyb2 and the actively transcribing form of RNAPII (Figure 3.7C), coupled with similar organisation patterns between the labels suggests some functional relationship between them. This strengthens the case for a possible role of PfMyb2 as a factor involved in active transcription and

RNA processing, although the lack of complete co-localisation indicates that PfMyb2 localisation cannot be directly interpreted as a region of active transcription. In a related manner, the putative PfMyb2 target genes, *Pfcrk-1* and *Pfmap1*, are not greatly expressed until the late ring-stage and mature parasite stages (Bozdech *et al.*, 2003, Baker, 2008). This suggests that, while in late ring-stage parasites a portion of nuclear labeling may be attributed to binding of PfMyb2 to these target genes, this does not account for the bulk of nuclear labeling patterns of PfMyb2 in the greater part of the ring-stage, which are most likely independent of interactions with these genes.

It may be that the PfMyb2 signal that is found spatially distinct from the elongating RNAPII is involved in some other unrelated, as yet unspecified, function, or that PfMyb2 may be associating with regions of poised transcription machinery, in addition to the actively transcribing RNAPII. If this were the case, then PfMyb2 could be considered a marker for transcription potential rather than just transcription activity. Alternatively the distinct PfMyb2 compartments may be regions of sequestration of excess or inactive protein, stored for when it is needed again. None of these functions for PfMyb2 have yet been demonstrated in the literature, and additional biochemical and molecular evidence would be needed to confirm the role of PfMyb2 relative to its nuclear localisation.

In contrast, computational image analysis showed that the signal for active histone modification H3K9ac displays no greater colocalisation or association with PfMyb2 signal than is observed with repressive H3K9me3 and PfMyb2 (Figure 3.9). This strengthens the case for independent nuclear organisation of different nuclear factors; in addition, the lack of significant co-localisation between H3K9ac and PfMyb2 may indicate a very limited role H3K9ac in transcriptional of activiation. This corresponds to the suggestion by Salcedo-Amaya *et al.* (2009) that H3K9ac may simply be involved in the establishment of euchromatin, while other factors may be more directly involved in transcriptional activation.

The frequent perinuclear localisation of PfMyb2 and RNAPII signals, as indicators of potential transcriptional activity, is indicative of the perinuclear organisation of regions of transcriptional activity, distinct from the nuclear-interior labeling of H3K9ac. These labeling results correspond to a model of parasite nuclear organisation in which transcription is spatially confined to the nuclear periphery, as previously

indicated (Mancio-Silva *et al.*, 2010), particularly as the active markers are often observed to interweave between each H3K9me3 and *var* loci at the nuclear periphery.

While the analysis of individual labeled nuclei allowed each of these nuclear organisational trends to be teased from the data, the greater power of the dual labeling and high-content imaging approach lies in the ability to assess labelings in very large sample sets. Analysis of hundreds to thousands of parasite nuclei revealed much more diverse nuclear labeling patterns than expected based on the previous literature (Lopez-Rubio *et al.*, 2009; Salcedo-Amaya *et al.*, 2009; Volz *et al.,* 2010). This variable nuclear labeling points towards an overall variability in the nuclear organisation of *P. falciparum,* in strong contrast to the stereotyped nuclear model often presented in the literature (i.e. Ralph *et al.,* 2005; Lopez-Rubio *et al.,* 2009; Volz *et al.,* 2010).

The possibility that the observed variability was artefactual was considered. However, one may reason that, if diverse labeling results were due to artefactual or non-specific signal, one could expect a limited set of labeling scenarios: 1) variable labeling detected in only a small number of samples, produced by an infrequent sample-dependent artefact; 2) a full spectrum a different labeling results with no discernable pattern or trends, produced by a random non-particular artefact of sample preparation, labeling or imaging, or by non-specific binding of antibodies to a random array of molecules in the sample; or 3) a single very specific and consistent labeling pattern, produced by a consistent artefact disrupting the sample in some particular way during handling, or by antibody cross-reactivity to one or more particular molecules or altered structures in the sample.

In contrast, H3K9me3, H3K9ac and PfMyb2 labeling across a large number of samples was consistently detected as a limited set of diverse patterns, such that could each be assigned to one of five discrete labeling classes (Figures 3.1, 3.2 and 3.3). Such observed signals are more likely to be specific antibody labeling of the targets, as the targets occupy variable sub-nuclear localisations, than to be aretfacts. In addition, correlation of much of the relative localisation data for each marker with the current literature, as discussed above, bolsters the biological relevance of the labeling patterns obtained.

The consistent variability in the labeling patterns studied implies the existence of some underlying biological mechanism to account for and regulate such diversity. Quantitative analysis of co-labeling data revealed no relationship between the patterns adopted by each the assayed H3K9me3, H3K9ac and PfMyb2 targets (Figure 3.9), implying some other mechanism of regulation of the nuclear organisation, such as environmental factors or age-dependent dynamic organisation.

The possibility of parasite nuclear organisation being transient or dynamic in an age-dependent manner was assessed by a high-resolution time course experiment carried out with H3K9me3, H3K9ac or PfMyb2 labeling. The statistically significant shifts observed in the sample population distributions for each label indicate that the sampled parasites do indeed display a time-dependent shift (Figure 3.10). The gradual shift of H3K9ac signal from perinuclear towards diffuse labeling is in accordance with the diffuse H3K9ac labeling shown by Volz *et al.* (2010), and the genomic distribution of H3K9ac throughout the majority of the protein coding regions (Salcedo-Amaya *et al.,* 2009). The shift of H3K9me3 and PfMyb2 labeling from the dominant single perinuclear signal or cap pattern to greater proportions of multiple perinuclear foci may correlate with the previously published literature regarding H3K9me3 distribution (Lopez-Rubio *et al.*, 2009), and the perinuclear PfMyb2 labeling data shown in this chapter (Figures 3.6 and 3.7).

Some striking differences are observed in the relative distributions of H3K9me3, H3K9ac and PfMyb2 label patterns in mixed-age ring-stage samples (Figures 3.1-3.2, 3.4) and those assessed across the IDC ring-stage (Figure 3.10). This may be due to a number of factors. For example, if sample preparation, when carried out on a smaller or larger scale (for tightly synchronised ring-stage and mixed-age parasites, respectively) were found to favour a certain parasite age or nuclear organisation, this may result in over-representation of associated nuclear label patterns in one data set but not the other, thus skewing the relative pattern frequencies detected in each case. Alternatively, these differences may be indicative of an alternative component of variable nuclear organisation, namely that it may be heritable. In such a case, a *P. falciparum* culture may display shifted population distributions of the different labeling patterns, due perhaps to being maintained in *in vitro* culture for a longer period, or to changes in environmental conditions, which may trigger changes in transcriptional activity and associated nuclear organisation of domains of

transcriptional activity and repression. Such a heritable model of nuclear organisation need not be exclusive of developmentally-linked variability in nuclear organisation, accounting both for the differences in relative proportions of label patterns in mixed-age ring-stage parasite and time-course samples, as well as for the shifts in nuclear organisation observed across the time-course.

The application of STORM to *P. falciparum* may aide in the understanding of the functional organisation of some of the labeling patterns detected for the nuclear markers assayed in this chapter. The discrete number of tightly clustered foci detected by STORM within the diffuse wide-field H3K9me3 signal (Figure 3.11), suggest that functional heterochromatic bundles may be retained within such a distribution, irrespective of whether it is a transient state or can be explained in some other way. The asymmetry of perinuclear distribution observed with STORM imaging of single or two perinuclear foci may represent individual molecules shifting around the nuclear periphery. However, the direction and dynamics of such a migration cannot be inferred from STORM data alone and further investigations would be necessary to confirm such a spatial rearrangement.

Although the diversity of nuclear organisation is clearly established here, only a single time course experiment was carried out to determine age-dependent dynamics. As such the trends shown here need further confirmation and statistical validation. In addition, plausible alternative explanations to age-dependent dynamic organisation, which may account for the observed variability, should also be investigated. While a number of the organisational patterns observed for H3K9me3, H3K9ac or PfMyb2 labeling may be difficult to reconcile with the current models of nuclear organisation for transcriptional regulation (i.e. Lopez-Rubio *et al.*, 2009; Salcedo-Amaya *et al.*, 2009; Volz *et al.,* 2010), such as diffuse H3K9me3 labeling and perinuclear H3K9ac signal, one cannot postulate on the possible function of these individual labeling patterns without a better understanding of the function of the detected nuclear variability in parasite biology as a whole.

Nevertheless, the data shown in this chapter, as a whole, very strongly demonstrate that the nuclear architecture of *P. falciparum*, and in particular the spatial organisation of euchromatic and heterochromatic regions with associated *var* gene loci and transcriptional regulatory factors, is highly variable, being able to adopt one of several

non-random organisations. Such variability has never before been demonstrated in the literature and is in stark contrast to the stereotypical perspective of *P. falciparum* nuclear organisation most frequently given in the literature, particularly in regard to *var* gene loci and histone modification organisation (i.e. Ralph *et al.*, 2005; Lopez-Rubio *et al.*, 2009). However, it does correlate to recent publications showing broader dynamics of nuclear organisation throughout the IDC of the parasite life cycle (Weiner *et al.*, 2011; Salcedo-Amaya *et al.*, 2009). The detection of this variability in nuclear organisation was only possible because of the high-content and computational analysis approach used, which allowed the assessment of very large numbers of nuclei. These findings clearly demonstrate the complexity of *P. falciparum* biology, and that the role of nuclear architecture in transcriptional regulation in the parasite may be more intricate than previously observed or expected.

3.5. Conclusion

High-content fluorescent microscopy assays and computational image analysis were used to study relative spatial organisation of H3K9me3, H3K9ac, PfMyb2, RNAP and *var* loci in ring-stage *P. falciparum.* Each nuclear target showed distinct and highly variable localisation trends, independent of each of the other targets. Exceptions to this were the putative transcription factor PfMyb2 and elongating RNAPII, which displayed close correlation and co-localisation of signals, indicating a functional relationship between the two molecules. This may provide strong complementary confirmation of the role of PfMyb2 in RNA processing, something as yet unpublished.

In contrast to the stereotyped *P. falciparum* nuclear model available in the current literature, the data from this chapter clearly demonstrates extensive variability in the spatial organisation of domains of transcriptional regulation within the nucleus. Such variation in the nucleus of a single IDC stage of the parasite has not been demonstrated or suggested in the literature prior to this point, to our knowledge. A single time course experiment suggests that such variable organisation may be transient and dependent on the age of the parasite, although further confirmation of

Chapter Four

Concluding Discussion

The *P. falciparum* parasite is particularly dependent on tight transcriptional regulation for its controlled progression through the IDC, pathogenesis and establishment of persistent infection by evasion of the human host's immune system. Such tight regulation appears to be achieved by the use a combination of regulatory mechanisms including transcription factors (De Silva *et al.,* 2008; Flueck *et al.*, 2010), epigenetic modulators (Cui and Miao, 2010), chromosomal organisation and the spatial localisation of specific gene loci (particularly *var* genes) with either transcriptionally permissive or repressive compartments (Ralph *et al.*, 2005; Lopez-Rubio *et al.*, 2009; Mancio-Silva *et al.*, 2010). Limitations of the sampling and imaging approaches used for studying the parasite have, however, left us with an incomplete understanding of the complexities of these mechanisms in the *P. falciparum* parasite, including their spatial organisation and interactions. Until recently models of parasite nuclear organisation have presumed a static and stereotyped spatial arrangement of nuclear compartments (i.e. Lopez-Rubio *et al.*, 2009). Recent data pointing to a more dynamic nuclear organisation (Salcedo-Amaya *et al.*, 2009; Weiner *et al.*, 2011) suggest that there may be more to our current understanding of *P. falciparum* nuclear organisation than these static models show. However, this has been limited to biochemical assays and global assessments of chromatin organisation. The relevance of these findings to transcriptional activity and repression has not been previously shown, nor the relative organisation and possible dynamics of many transcription regulatory factors and domains.

This study set out to investigate the spatial relationship between several factors related to transcriptionally active or repressive domains, as well as the potential dynamics of such organisation within the *P. falciparum* parasite nucleus during the IDC. A high-content fluorescent microscopy based approach was selected for such a study in order to overcome many of the current limitations to conventional microscopy approaches and to allow the generation of high-resolution information regarding parasite nuclear organisation of domains of transcriptional activity, based on data from very large sample sets.

The implementation of such an imaging approach hinged on our ability to prepare optimally fixed samples and to specifically, sensitively and reproducibly label target molecules of interest within these samples. The optimised, high quality sample preparation achieved in this work, coupled with the consistent labeling obtained with each established marker allowed, for the first time in *P. falciparum* parasites, the efficient labeling of very large sample sets (a few hundred to thousands) of parasite nuclei, suitable for semi-automated imaging and computational image analysis. The parallel development of a bespoke computational analysis algorithm, such as has not before been implemented in the study of the parasite, allowed consistent, accurate and unbiased analysis of the large imaging data sets generated in this approach.

Such analysis of these large sample sets revealed extensive variability of the nuclear organisation of *P. falciparum*, which has been previously undetected or unreported in the literature. The demonstration of such diversity of nuclear organisation as seen here in ring-stage parasites implies an underlying biological mechanism that may be revealed in this variability. One possible explanation is that parasite nuclear organisation may be dynamic, such that the different spatial patterns detected in the fixed samples are in fact transient states adopted by the parasite. The time course assay carried out in this work suggests a dynamic, age-dependent variability of the nuclear organisation, perhaps as a form of maturation of the parasite's nuclear architecture as it progresses through the IDC. This correlates with recent publications showing dynamic changes in the chromatin organisation within the nucleus (Weiner *et al.*, 2011) and histone modification distributions across the genome (Salcedo-Amaya *et al.*, 2009) during the parasite's IDC. Such dynamic organisation would have significant implications for our understanding of nuclear architecture and its role in transcriptional regulation in the parasite. For example if such dynamics could be confirmed and were found to continue into the later stages of the IDC, one may postulate that such a mechanism may play a role in the co-ordination of the tightly regulated cascade of transcriptional activity reported by Bozdech *et al.* (2003) to occur throughout the parasite IDC.

Our observations of distinct perinuclear localisation of both transcription repressive markers and those involved with active transcription support the model that the *P. falciparum* nuclear periphery features distinct compartments of transcriptional repression (or PERCs) (Lopez-Rubio *et al.*, 2009) as well as sites of active

transcription (Mancio-Silva *et al.*, 2010). However, although the perinuclear *var* foci appear to be a persistent feature of the parasite's nucleus, the dynamic nuclear organisation suggests that these H3K9me3-enriched heterochromatic islands may not be as static as previously thought, implying that the hypothesised PERCs may be more transient or mobile than initially assumed. Similarly, although the perinuclear foci of transcriptional activity markers are suggestive of a transcription factory model of transcriptional organisation, such multi-gene clusters of active transcription are unlikely to remain tethered at the nuclear periphery, based on the dynamic nature of the different transcriptional compartments suggested by our data. The observed variable organisation of regions of transcriptional activity and repression also implies a similar variable organisation of a multitude of other nuclear factors involved in transcriptional regulation in the parasite including that of telomere-associated chromatin modifiers (Perez-Toledo *et al.,* 2009; Flueck *et al.,* 2010; Chene *et al.,* 2012; Volz *et al.,* 2012), filamentous actin (Zhang *et al.,* 2011), ApiAP2 transcription factors and regulators (De Silva *et al.,* 2008; Flueck *et al.*, 2010) and noncoding RNA species (Li *et al.*, 2008; Epp *et al.*, 2009; Broadbent *et al.*, 2011). Further investigations into the extent of organisational variability or dynamics for each of these factors may help in elucidating some interactions or regulatory pathways for the co-ordination of such gross organisational dynamics.

An alternative explanation for the diversity of nuclear organisation detected may be one of deliberate diversification of transcriptional potential and associated parasite fitness within the parasite population during the IDC. Recent work by Rovira-Graells *et al.* (2012) has shown that the *P. falciparum* parasite makes use of heritable epigenetic and transcriptional heterogeneity within populations as a form of "bet-hedging" against environmental changes. This ensures that at least a small proportion of the parasite is likely to have improved fitness under new conditions, thus improving the chance of parasite survival among the wide range of conditions encountered by the parasite throughout its life cycle. One may expect such heterogeneity to be evident in the nuclear architecture of a parasite population, perhaps in a manner similar to the diversity we have observed here among ring-stage parasites.

Although the biological functions and mechanisms behind the diversity in nuclear organisation in the *P. falciparum* parasite are as yet uncertain, the discovery of such

variability of nuclear architecture indicates a much greater level of complexity of parasite biology, and particularly transcriptional regulation within the parasite, than previously observed or expected. The fact that this organisational variability has not been previously reported in the literature may be indicative of a bias in the current research field. This may have come about due to limits in imaging technology applicable to *Plasmodium*, under-sampling in assays, as well as low confidence in the labels used, such that, as the more static organisation models have become established (i.e. Lopez-Rubio *et al.,* 2009; Volz *et al.*, 2010), detected variations may have been discarded as non-specific signals.

Compounding this problem may be the technical challenges inherent in working with *P. falciparum* parasites. This is reflected in the extensive optimisation required for the establishment of sample preparation and labeling assays in this work. The difficulty in adapting many techniques established in different organisms or laboratories often hinders the application of new and exciting technologies to the study of the parasite, as seen with smFISH and STORM here. These challenges may be due to biological differences and complexities of the organism and, coupled with the organisational variability uncovered here, point to the complexity of the parasite, as a not-yet well understood organism and model for the study of transcriptional regulation and nuclear architecture.

This inherent parasite complexity and diversity should be taken into account both in the construction of models for our current understanding of parasite transcriptional regulation as well as in any future studies regarding parasite gene expression. Interestingly, it would appear that the *P. falciparum* parasite's characteristic complexity and extensive use of epigenetic and spatial regulatory mechanisms may be a weak point in its functioning that may successfully be targeted for drug treatment (Salcedo-Amaya *et al.*, 2010). For example, the parasite's use of unique histone modification regulatory pathways may allow the development of histone modification enzyme-specific drugs targeting the parasite, similar to those used in targeting cancer cells (Biancotto *et al.*, 2010). The regulatory factors involved in essential dynamic processes such as transcription foci assembly may also prove possible targets for drug treatment. Thus elucidation of the full repertoire of epigenetic mechanisms employed by the parasite, as well as the function of variable spatial organisation in regulation of the parasite's gene expression, may allow the identification of unique enzymes,

pathways or mechanisms to target in the parasite, providing us with potentially powerful weapons against this widespread pathogen.

In conclusion, in this work we have demonstrated the potential of high-content fluorescent microscopy assays for the study of the spatial organisation and dynamics in the *P. falciparum* parasite nucleus. Select organisational trends as well as strong evidence for variability in the parasite's nuclear architecture, with extensive implications for our understanding of parasite biology and transcriptional regulation have been shown. As technological advances continue, our increasing capacity to implement emerging high-content and super-resolution techniques can be expected to greatly facilitate microscopy-based studies of a range of various nuclear components in *P. falciparum,* for the purpose of understanding organisational and transcriptional heterogeneity within the parasite.

Despite the large volume of information generated in this study, it remains possible that some information regarding nuclear labeling patterns would have been lost due to the two-dimensional approach used. Future studies should, ideally, make use of a three-dimensional approach to ensure further construction of accurate models of the complexity and dynamics of nuclear organisation. The future establishment and inclusion of RNA-FISH or smFISH and BrUTP incorporation assays in such studies may finally bring to light the extent to which regulatory mechanisms deciphered for *var* gene regulation may apply to non-antigen coding genes, as well as the effect of organisational variation on both antigen-encoding and non-antigen encoding genes. Future studies would be also be aided by more extensive use of super-resolution techniques such as STORM or even dual-coloured STORM, in the investigation of sub-diffractive organisation and interactions of nuclear factors and their biological functions. Coupled with data from high-content assays, such techniques can reveal subtleties in spatial organisations and structures as well as allow the sensitive detection of sites of single molecules or clusters of few molecules, which may be important in understanding variation and dynamics in nuclear architecture.

References

Abbe E. 1873. Beiträge zur Theorie des Mikroskops und der mikroskopischen Wahrnehmung. Archiv für Mikroskopische Anatomie 9: 413-420.

Baker GL. 2008. Master of Science dissertation: Cloning and expressing PfMyb2, a *Plasmodium falciparum* DNA-binding protein. University of Witwatersrand, South Africa.

Berger A, Cabal G, Fabre E, Duong T, Buc H, Nehrbass U, Olivo-Marin JC, Gadal O, Zimmer C. 2008. High-resolution statistical mapping reveals gene territories in live yeast. Nature Methods 5: 1031-1037.

Biancotto C, Frige G, Minucci S. 2010. Histone modification therapy of cancer. Advanced Genetics 70: 341-386.

Blobel G. 1985. Gene gating: A hypothesis. Proceedings of the National Academy of Science 82: 8527-8529.

Bozdech Z, Llinas M, Pulliam BL, Wong ED, Zu J, DeRisi JL. 2003. The Transcriptome of the Intra-erythrocytic Developmental Cycle of *Plasmodium falciparum*. Public Library of Science 1: 85-100.

Broadbent KM, Park D, Wolf AR, Van Tyne D, Sims JS, Ribacke U, Volkman S, Duraisingh M, Wirth D, Sabeti PD, Rinn JL. 2011. A global transcriptional analysis of *Plasmodium falciparum* malaria reveals a novel family of telomere-associated lncRNAs. Genome Biology 12: R56.

Cabal G, Genovesio A, Rodriguez-Navarro S, Zimmer C, Gadal O, Lesne A, Buc H, Feuerbach-Fournier F, Olivo-Marin JC, Hurt EC, Nehrbass U. 2006. SAGA interacting factors confine sub-diffusion of transcribed genes to the nuclear envelope. Nature 441: 770-773.

Chambeyron S, Bickmore W. 2004. Chromatin decondensation and nuclear reorganization of the HoxB locus upon induction of transcription. Genes & Development 18: 1119-1130.

Chene A, Vembar SS, Riviere L, Lopez-Rubio JJ, Claes A, Siegel TN, Sakamoto H, Scheidig-Benatar C, Hernandez-Rivas R, Scherf A. 2012. PfAlbas constitute a new eukaryotic DNA/RNA-binding protein family in malaria parasites. Nucleic Acids Research 40: 3066-3077.

Contreras-Dominguez M, Moraes CB, Dorval T, Genovesio A, de Macedo Dossin F, Freitas-Junior L. 2010. A modified fluorescence *in situ* hybridization protocol for *Plasmodium falciparum* greatly improves nuclear architecture conservation. Molecular and Biochemical Parasitology 173: 48-52.

Coulson R, Hall N, Ouzounis C. 2003. Comparative genomics of transcriptional control in the human malaria parasite *Plasmodium falciparum.* Genome Research 14: 1548-1554.

Cowman AF, Baldi DL, Healer J, Mills KE, O'Donnell RA, Reed MB, Triglia T, Wickham ME, Crabb BS. 2000. Functional analysis of proteins involved in *Plasmodium falciparum* merozoite invasion of red blood cells. FEBS Letters 476: 84–88.

Cremer T, Cremer C. 2001. Chromosome territories, nuclear architecture and gene regulation in mammalian cells. Nature 2: 292-301.

Cremer M, von Hase J, Volm T, Brero A, Kreth G, Walter J, Fischer C, Solovei I, Cremer C, Cremer T. 2001. Non-random radial higher-order chromatin arrangements in nuclei of diploid human cells. Chromosome Research 9: 541-561.

Cui L, Miao J. 2010. Chromatin mediated epigenetic regulation in the malaria parasite *Plasmodium falciparum.* Eukaryotic Cell 9: 1138-1149.

De Silva EK, Gehrke AR, Olszewski K, Leon I, Chahal JS, Bulyk ML, Llinas M. 2008. Specific DNA-binding by apicomplexan AP2 transcription factors. Proceedings of the National Academy of Sciences 105: 8393–8398.

Dzikowski R, Frank M, Deitch K. 2006. Mutually exclusive expression of virulence genes by malaria parasites is regulated independently of antigen production. PLOS Pathogens 2: e22.

Dzikowski R, Li F, Amulic B, Eisberg A, Frank M, Patal S, Wellems T, Deitsch K. 2007. Mechanisms underlying mutually exclusive expression of virulence genes by malaria parasites. EMBO reports 8: 959-965.

Eltoum I, Fredenburgh J, Myers RB, Grizzle WE. 2001. Introduction to the theory and practice of fixation of tissues. Journal of Histontechnology 24: 173-190.

Epp C, Li F, Howitt CA, Chookajorn T, Deitsch KW. 2009. Chromatin associated sense and antisense non-coding RNAs are transcribed from the *var* gene family of virulence genes of the malaria parasite *Plasmodium falciparum*. RNA 15: 116-127.

Freitas-Junior LH, Bottius E, Pirrit LA, Deitsch KW, Scheidig C, Gulnet F, Nehrbass U, Wellems T, Scherf A. 2000. Frequent ectopic recombination of virulence factor genes in telomeric chromosome clusters of *P. falciparum*. Nature 407: 1018-1022.

Freitas-Junior LH, Hernandez-Rivas R, Ralph SA, Montiel-Condado D, Ruvalcaba-Salazar OK, Rojas-Meza AP, Mancio-Silva L, Leal-Silvestre RJ, Gontijo AM, Shorte S, Scherf A. 2005. Telomeric Heterochromatin Propagation and Histone Acetylation Control Mutually Exclusive Expression of Antigenic Variation Genes in Malaria Parasites. Cell 121: 25-36.

Flueck C, Bartfai R, Niederwieser I, Witmer K, Alako BT, Moes S, Bozdech Z, Jenoe P, Stunnenberg HG, Voss TS. 2010. A major role for the *Plasmodium falciparum* ApiAP2 protein PfSIP2 in chromosome end biology. PLOS Pathogens 6: e1000784.

Griffiths CA. 2009. Honours project report: Sub-nuclear localisation of co-expressed genes, for the elucidation of transcriptional factories in *Plasmodium falciparum.* University of Pretoria, South Africa.

Hanssen E, Carlton P, Deed S, Klonis N, Sedat J, DeRisi J, Tilley L. 2010. Whole cell imaging reveals novel modular features of the exomembrane system of the malaria parasite, *Plasmodium falciparum*. International Journal of Parasitoogy 40: 123-134.

Heilemann M, van de Linde S, Mukherjee A, Sauer M. 2009. Super-resolution imaging with small organic fluorophores. Angewandte Chemie 48: 6903-6908.

Henriques R, Lelek M, Fornasiero EF, Valvorta F, Zimmer C, Mhlanga MM. 2010. QuickPALM: 3D real-time photoactivation nanoscopy image processing in ImageJ. Nature Methods 7: 339-340.

Henriques R, Griffiths C, Rego EH, Mhlanga MM. 2011. PALM and STORM: unlocking live-cell super-resolution. Biopolymers 95: 322-330.

Horrocks PE, Wong E, Russel K, Emes RD. 2009. Control of gene expression in *Plasmodium falciparum*- ten years on. Molecular and Biochemical Parasitology 164: 9-25.

Issar N, Ralph S, Mancio-Silva L, Keeling C, Scherf A. 2009. Differential sub-nuclear localisation of repressive and activating histone methyl modifications in *P. falciparum.* Microbes and Infection 11: 403-407.

Kraemer S, Smith J. 2006. A family affair: *var* genes, PfEMP1 binding, and malaria disease. Current Opinions in Microbiology 9: 374-380.

Kumaran R, Thakar R, Spector D. 2008. Chromatin Dynamics and Gene Positioning. Cell 132: 929-934.

Kyes S, Christodoulou Z, Pinches R, Kriek N, Horrocks P, Newbold C. 2007. *Plasmodium falciparum var* gene expression is developmentally controlled at the level of RNA polymerase II-mediated transcription initiation. Molecular Microbiology 63: 1237-1247.

Lambros C, Vanderberg JP. 1979. Synchronization of *Plasmodium falciparum* erythrocytic stages in culture. Journal ot Parasitology 65: 418-420

Li F, Sonbuchner L, Kyes SA, Epp C, Deitsch KW. 2008. Nuclear non-coding RNAs are transcribed from the centromeres of *Plasmodium falciparum* and are associated with centromeric chromatin. Journal of Biological Chemistry 283: 5692–5698.

Lieberman-Aiden E, van Berkum N, Williams L, Imakaev M, Ragoczy T, Telling A, Amit I, Lajoie B, Sabo P, Dorschner M, Sandstrom R, Bernstein B, Bendor M, Groudine M, Gnirke A, Stamatoyannopoulos J, Mirny L, Lander E, Dekker J. 2009. Comprehensive mapping of long-range interactions reveals folding principles of the human genome. 2009. Science 326: 289-293.

Lomvardas S, Barnea G, Pisapia DJ, Mendelsohn M, Kirkland J, Axel R. 2006. Interchromosomal Interactions and Olfactory Receptor Choice. Cell Host & Microbe 126: 403-413.

Lopez-Rubio JJ, Gontijo AM, Nunes MC, Issar N, Hernandez Rivas R, Scherf A. 2007. 5' Flanking region of *var* genes nucleate histone modification patterns linked to phenotypic inheritance of virulence traits in malaria parasites. Molecular Microbiology 66: 1296-1305.

Lopez-Rubio JJ, Mancio-Silva L, Scherf A. 2009. Genome-wide Analysis of Heterochromatin Associates Clonally Variant Gene Regulation with Perinuclear Repressive Centers in Malaria Parasites. Cell Host & Microbe 5: 179-190.

(a) Mancio-Silva L, Rojas-Meza AP, Vargas M, Scherf A, Hernandez-Rivas R. 2008. Differential Association of Orc1 and Sir2 proteins to telomeric domains in *Plasmodium falciparum*. Journal of Cell Science 121: 2046-2053.

(b) Mancio-Silva L, Freitas-Junior LH, Scherf A. 2008. Fluorescent *in situ* hybridization (FISH) DNA–DNA for *Plasmodium falciparum*. In: Moll K, Ljungström I, Perlmann H, Scherf A, Wahlgren M, editors. Methods in malaria research. 5th ed. MR4/ATCC and BioMalPar: 223–224.

Mancio-Silva L, Zhang Q, Scheidig-Benatar C, Scherf A. 2010. Clustering of dispersed ribosomal DNA and its role in gene regulation and chromosome-end associations in malaria parasites. Proceedings of the National Academy of Sciences 107: 15117-15122.

Merrick CJ, Duraisingh MT. 2010. Epigenetics in *Plasmodium*: What do we really know? Eukaryotic Cell 9: 1150-1158.

Meyersfeld D. 2005. Doctoral Thesis: Aspects of gene expression and regulation in *Plasmodium falciparum* gametocytogenesis. University of Witwatersrand, South Africa.

Misteli T. 2005. Concepts in nuclear architecture. BioEssays 27: 477-487.

Mitchell JA, Fraser P. 2008. Transcription factories are nuclear subcompartments that remain in the absence of transcription. Genes and Development 22: 20-25.

Osborne CS, Chakalova L, Brown KE, Carter D, Horton A, Debrand E, Goyenechea B, Mitchell JA, Lopes S, Reik W, Fraser P. 2004. Active genes dynamically colocalize to shared sites of ongoing transcription. Nature Genetics 36: 1065-1071.

Perez-Toledo K, Rojas-Meza AP, Mancio-Silva L, Hernandez-Cuevas NA, Delgadillo DM, Vargas M, Martinez-Calvillo S, Scherf A, Hernandez-Rivas R. 2009. *Plasmodium falciparum* heterochromatin protein 1 binds to tri-methylated histone 3 lysine 9 and is linked to mutually exclusive expression of var genes. Nucleic Acids Research 37: 2596-2606.

Pombo A, Jackson DA, Hollinshead M, Wang Z, Roeder RG, Cook PR. 1999. Regional specialization in human nuclei: visualization of discrete sites of transcription by RNA polymerase III. The EMBO Journal 18: 2241-2253.

Raj A, van den Bogaard P, Rifkin SA, van Oudenaarden A, Tyagi S. 2008. Imaging individual mRNA molecules using multiple singly labeled probes. Nature Methods 5: 877-879.

Ralph S, Scheidig-Benatar C, Scherf A. 2005. Antigenic variation in *Plasmodium falciparum* is associated with movement of *var* loci between subnuclear locations. Proceedings of the National Academy of Sciences 102: 5414-5419.

Riglar DT, Richard D, Wilson DW, Boyle MJ, Dekiwadia C, Turnbull L, Angrisano F, Marapana DS, Rogers KL, Whitchurch CB, Beeson JG, Cowman AF, Ralph SA, Baum J. 2011. Super-resolution dissection of coordinated events during malaria parasite invasion of the human erythrocyte. Cell Host & Microbe 9: 9–20.

Rovira-Graells N, Gupta AP, Planet E, Crowley VM, Mok S, de Pouplana LR, Preiser PR, Bozdech Z, Cortés A. 2012. Transcriptional variation in the malaria parasite *Plasmodium falciparum.* Genome Research 22: 925-938.

Rust MJ, Bates M, Zhuang X. 2006. Sub-diffraction-limit imaging by stochastic optical reconstruction microscopy (STORM). Nature Methods 3: 793-795.

Rychlik W, Spencer WJ, Rhoads RE. 1990. Optimization of the annealing temperature for DNA amplification *in vitro*. Nucleic Acids Research 18: 6409-6412.

Saksouk N, Bhatti MM, Kieffer S, Smith AT, Musset K, Garin J, Sullivan WJ Jr., Cesbron-Delauw MF, Hakimi MA. 2005. Histone-modifying complexes regulate gene expression pertinent to the differentiation of the protozoan parasite *Toxoplasma gondii*. Molecular Cell Biology 25: 10301-10314.

Salcedo-Amaya AM, van Driel MA, Alako BT, Trelle MB, van den Elzen AM, Cohen AM, Janssen-Megens EM, van de Vegte-Bolmer M, Selzer RR, Iniguez AL, Green RD, Sauerwein RW, Jensen ON, Stunnenberg HG. 2009. Dynamic histone H3 epigenome marking during the intraerythrocytic cycle of *Plasmodium falciparum*. Proceedings of the National Academy of Sciences 106: 9655-9660.

Salcedo-Amaya AM, Hoeijmakers WAM, Bartfai R, Stunnenburg H. 2010. Malaria: Could its unusual genome be the weak spot? The International Journal of Biochemistry and Cell Biology 42:781-784

Scherf A, Hernandez-Rivas R, Buffet P, Bottius E, Benatar C, Pouvelle B, Gysin J, Lanzer M. 1998. Antigenic variation in malaria: *in situ* switching, relaxed and mutually exclusive transcription of *var* genes during intra-erythrocytic development in *Plasmodium falciparum.* The EMBO Journal 17: 5481-5426.

Schneider R, Grosschedl R. 2007. Dynamics and interplay of nuclear architecture, genome organization, and gene expression. Genes & Development 21: 3027-3043.

Sexton T, Schober H, Gasser S. 2007. Gene regulation through nuclear organisation. Nature Structural & Molecular Biology 14: 1049-1055.

Spilianakis C, Lalioti M, Town T, Lee G, Flavell R. 2005. Interchromosomal association between alternatively expressed loci. Nature 435: 637-645.

Taddei A, Hediger F, Neumann F, Gasser S. 2004. The function of nuclear architecture: a genetic approach. Annual Reviews in Genetics 38: 305-345.

Trager W, Jensen J. Human malaria parasites in continuous culture. 1976. Science 193: 673-675.

Tuteja R. 2007. Malaria: an overview. FEBS Journal 274: 4670-4679.

Vogelsang J, Kasper R, Steinhauer C, Person B, Heilemann M, Sauer M, Tinnefeld P. 2008. A reducing and oxidizing system minimizes photobleaching and blinking of fluorescent dyes. Angewandte Chemie International Edition 47: 5465-5469.

Volpi EV, Chevret E, Jones T, Vatcheva R, Williamson J, Beck S, Campbell RD, Goldsworthy M, Powis SH, Ragoussis J, Trowsdale J, Sheer D. 2000. Large-scale chromatin organization of the major histocompatibility complex and other regions of human chromosome 6 and its response to interferon in interphase nuclei. Journal of Cell Science 113: 1565-1576.

Voss TS, Healer J, Marty AJ, Duffy MF, Thompson JK, Beeson JG, Reeder JC, Crabb BS, Cowman AF. 2006. A *var* gene promoter controls allelic exclusion of virulence genes in *Plasmodium falciparum* malaria. Nature 439: 1004-1008.

Volz J, Carvalho T, Ralph S, Gilson P, Thompson J, Tonkin C, Langer C, Crabb B, Cowman A. 2010. Potential epigenetic regulatory proteins localise to distinct nuclear sub-compartments in *Plasmodium falciparum*. International Journal for Parasitology 40: 109-121.

Volz J, Bartfai R, Petter M, Langer C, Josling GA, Tsuboi T, Schwash F, Baum J, Rayner JC, Stunnenburg HG, Duffy MF, Cowman AF. 2012. PfSET10, a *Plasmodium falciparum* methyltransferase, maintains the active *var* gene in a poised state during division. Cell Host & Microbe 11:7-18.

Xu M, Cook P. 2008. Similar active genes cluster in specialized transcription factories. Journal of Cell Biology 181: 615-623.

Weiner A, Dahan-Pasternak N, Shimoni E, Shinder V, von Huth P, Elbaum M, Dzikowski R. 2011. 3D nuclear architecture reveals coupled cell cycle dynamics of chromatin and nuclear pores in the malaria parasite *Plasmodium falciparum*. Cellular Microbiology 13:967-977.

Wissing F, Sanchez CP, Rohrbach P, Ricken S, Lanzer M. 2002. Illumination of the malaria parasite *Plasmodium falciparum* alters intracellular pH: Implications for live cell imaging. Journal of Biological Chemistry 277: 37747-37755.

Zhang Q, Huang Y, Zhang Y, Fang X, Claes A, Duchateau M, Namane A, Lopez-Rubio JJ, Pan W, Scherf A. 2011. A critical role of perinuclear filamentous actin in spatial repositioning and mutually exclusive expression of virulence genes in Malaria parasites. Cell Host & Microbe 10: 451-463.

Appendix A.1. Additional information regarding STORM

The resolution of light microscopy is limited by the diffraction of light as it passes through different media. This diffraction perturbs or broadens the image of an object such that, if two objects are closer than a particular distance, the resolution limit, then their images start to overlap and interfere with each other's and they cannot be distinguished. This resolution limit is dependent on the wavelength of light, but for most purposes can be considered to be approximately 200nm (Abbe, 1873).

The diffraction of an image can be approximated by a mathematical function, a Gaussian distribution, such that, if we were to image just one object, or in the case of fluorescent microscopy, one fluorophore, we can calculate the original signal, and determine the centre of mass of the object with an accuracy greater than the resolution limit. STORM (Rust *et al*., 2006; reviewed in McEvoy *et al*., 2010 and Henriques *et al*., 2011) makes use of this principle by modulating the emission profile of a population of fluorophores such that they repeatedly cycle through the light and dark states, or "blink", in a stochastic manner. Thus only a subset of the fluorophore population in a sample emits signal at any given time and signal from a limited number of fluorophores, with non-overlapping images, can be detected in a given moment. By acquiring a series of multiple (1000's to 100000's) sequential images for a single field of view, images of the majority of the fluorophores in a sample can be acquired where no surrounding fluorophores are emitting signal. The centre of mass of each object in a field of view can then be accurately calculated. A localisation accuracy of up to 20nm can be attained for such an acquisition procedure. This accuracy, or resolution, is dependent primarily on the brightness of the fluorophore signal in relation to background signal, or the signal-to-noise-ratio (SNR) (Henriques *et al*., 2011).

Modulation of the emission profile of fluorophores is achieved using high intensity light of two different wavelengths to stimulate the fluorophore to emit light, and to then force it back down to the dark ground state. In addition, the inclusion of oxidizing and reducing agents in the imaging buffer establishes a redox system in the imaging environment. This serves to protect the fluorophore from permanent photobleaching, as well as assist the fluorophore in cycling between the light and dark

states, via an ill-defined triplet state (Vogelsang *et al.,* 2008, reviewed by Henriques *et al*., 2011) (Figure A-1).

The QuickPALM processing algorithm (Henriques *et al*., 2010), uses a CLEAN algorithm to process each detected signal in each of the 1000's to 100000's of images acquired for a single STORM acquisition. The algorithm assesses the size (diameter), symmetry and circularity and SNR. Based on these criteria, the QuickPALM algorithm determines the likelihood of each point signal being signal from a single sub-diffractive molecule (fluorophore). If a signal meets these criteria, it is deemed a true object, and the centre of mass of the signal is calculated. The centre of mass determined for each object in each frame is plotted onto a single image to build a super-resolution reconstruction of the original data set.

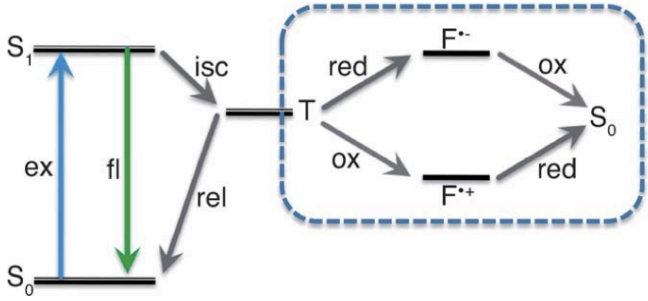

Figure A-1: Schematic of the cycling of fluorophores between the light and dark states, via the triplet state. The absorbtion of a photon by a ground state (S_0) fluorophore excites the fluorohphore (ex) such that it occupies a singlet state (S_1). The fluorophore may return to the ground state by emitting energy as light (fl). Alternatively, a fluorophore occasionally enters the dark triplet state (T) by a process called intersystem crossing (isc). From the unstable triplet state, the fluorophore is particularly susceptible to permanent oxidative photobleaching, so that spontaneous relaxation back to the ground state (rel) is a rare occurrence. Within the boxed region: The presence of oxidizing and reducing agents in the imaging environment protects the triplet state from reactive oxygen species. Electron transfer reactions with the redox reagents result in fluorophore radicals ($F^{\bullet+}$ and $F^{\bullet-}$). These unstable forms are retrieved back to the ground state by the reciprocal reduction or oxidation reaction. This process allows the fluorophore to cycle between dark (ground and triplet) and light (singlet) states while avoiding photobleaching. Taken from Henriques *et al*. (2011).

Appendix A.2. Additional results from assay optimisations in Chapter 2.

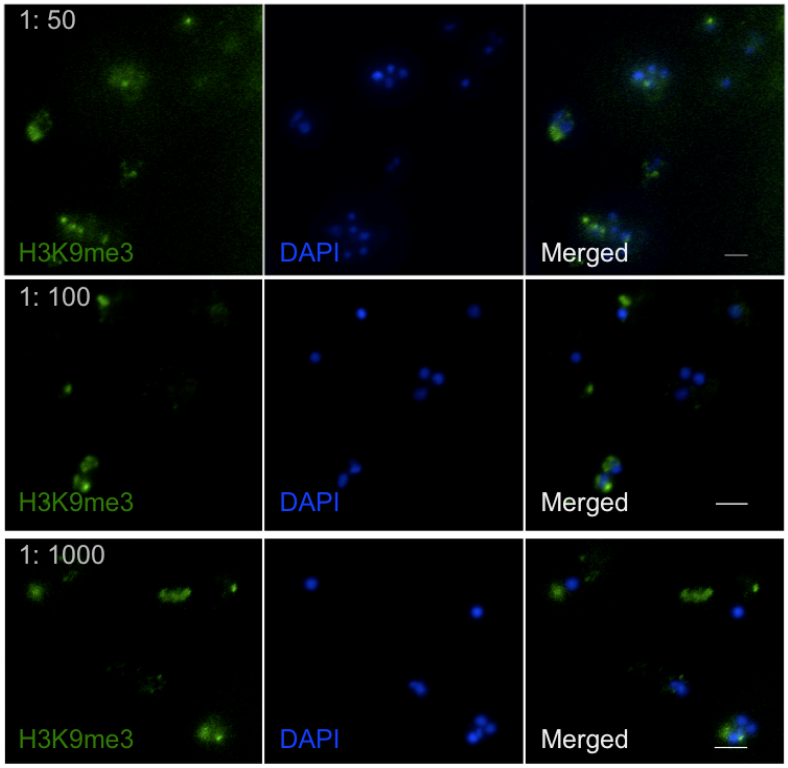

Figure A-2: Titration of mouse-anti-H3K9me3 antibody for IF. Representative results for IF assays carried out using 1:50, 1:100 and 1:1000 mouse-anti-H3K9me3 primary antibody, as indicated, with anti-mouse-ATTO488 secondary antibody (green). Parasite nuclei were stained with DAPI (blue). Scale bars=3 µm.

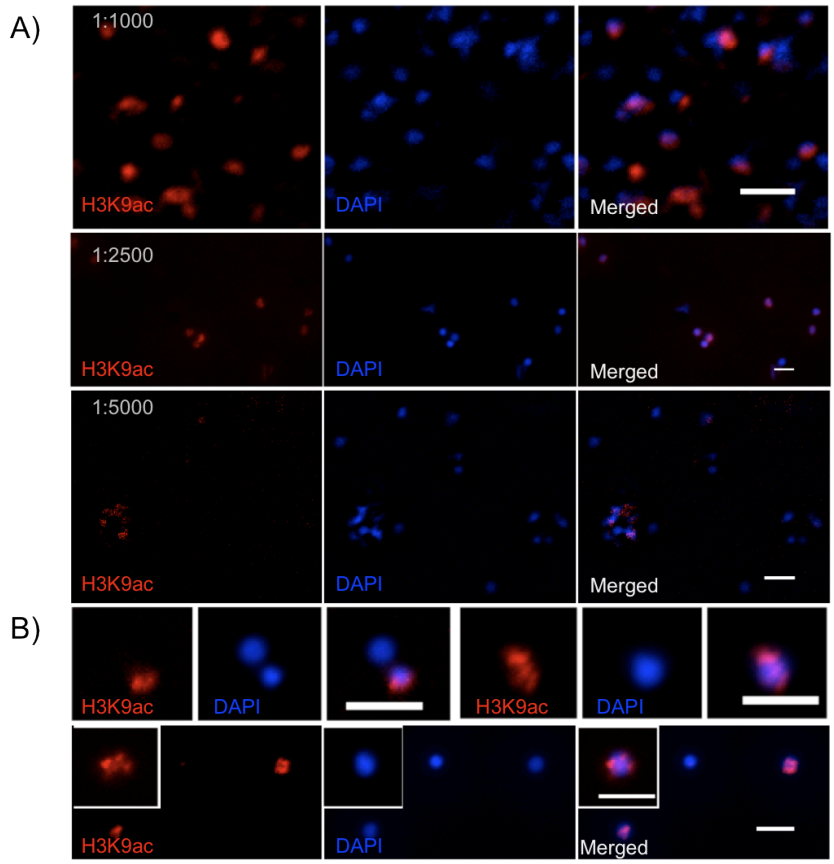

Figure A-3: Titration of rabbit-anti-H3K9ac antibody for IF. A) Representative results for IF assays carried out using 1:1000, 1:2500 and 1:5000 rabbit-anti-H3K9ac primary antibody, as indicated, with anti-rabbit-AlexaFluor532 secondary antibody (red). B) Additional representative images of H3K9ac labeling at 1:2000 – 1:2500 dilution. Parasite nuclei were stained with DAPI (blue). Scale bars=3 µm.

Appendix B.1. Image processing methodology

The following methodology was written by Rethabile Kuthlang as a description of the Computational image analysis algorithm implemented by him for this work:

Supervised classification was used to quantify the distributions of the PfMyb2, H3K9ac and H3K9me3 markers in parasite populations. The nuclear distribution of each marker was studied using shape and size features. These features were defined with respect to the nucleus. The classes that describe the marker distributions were heuristically defined. The following classes were derived from the features:

- Cap: a spot that localises on the edge of the nucleus and protrudes outwards.
- Cup: a spot that covers approximately a third of the nuclear perimeter. It is an elongated "cap".
- 1 perinuclear spot: a single spot that localises on the edge of the nucleus.
- 2 perinuclear spots: two spots that localizes on the edge of the nucleus.
- 3+ perinuclear spots: three or more spots localised on the edge of the nucleus.
- Sub-nuclear diffuse region ("Half nucleus diffuse"): a spot that covers a wide area of the nucleus, but less than half.
- Diffuse labeling through nuclear region ("Full nucleus diffuse"): a spot that covers over half the area of the nucleus.

The classification algorithm input consisted of the multi-channel image, with nuclear labels and markers of interest. The nuclear images were passed through a hierarchical K-means filter (Dufour *et al*., 2006) to detect the individual nuclei in the image. The hierarchical K-means function, as implemented in the ICY open-source image analysis platform, iteratively thresholds the image based on a K-means classification of the image histogram. The value of K, the number of clusters, was set to 6. The detected nuclei were then area filtered, with the minimum size set at 10 pixels and maximum size set at 365 pixels. The thresholds were determined empirically. The nuclear marker channels were individually inputted to the spot detection algorithm in ICY, based on the discrete wavelet transform (Olivo-Marin, 2002). The spot detector was set at 100% sensitivity to spots of size 4 to 7 pixels. The algorithm outputted detected spots, which were each categorized into one of the classes by the classifier using the derived features. The script was then able to plot the population distribution

and correlation graphs for each of the *a priori* determined classes so that, for the inputted image, the final output was the detected nuclei, and for each nucleus the co-localising protein was classified into one of the feature based classes. The protein distributions could be manually examined for the set of input images.

References:

Dufour A, Meas-Yedid V, Grassart A, Olivo-Marin JC. 2008. Automated Quantification of Cell Endocytosis Using Active Contours and Wavelet, Proc. ICPR 2008, Tampa, FL, USA.

Olivo-Marin JC. 2002. Extraction of spots in biological images using multiscale products. *Pattern Recognition* 35: 1989-1996.

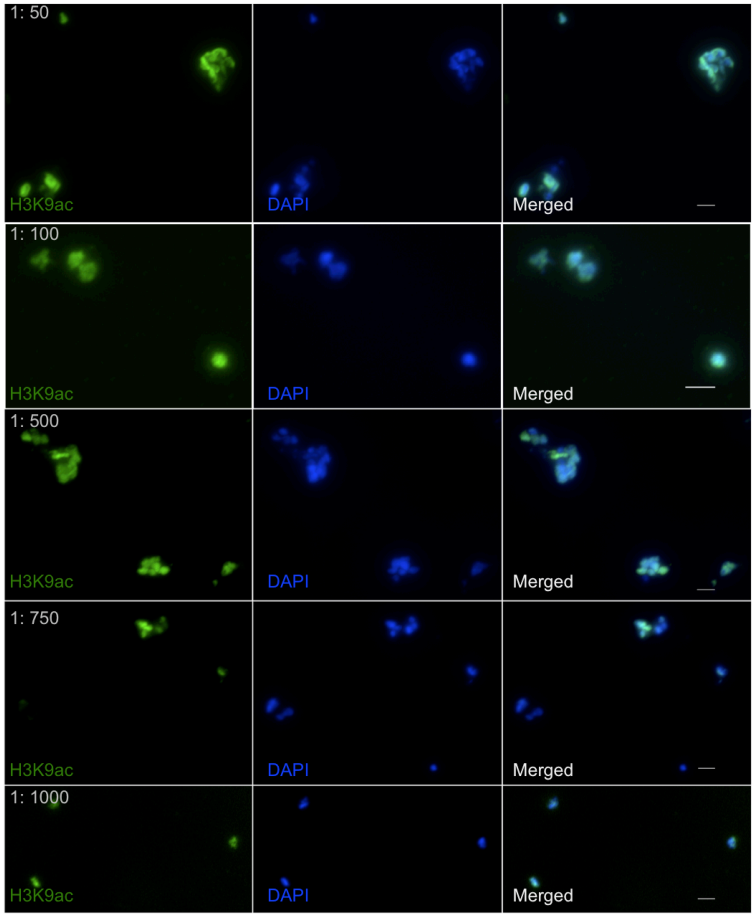

Figure A-4: Titration of mouse-anti-H3K9ac antibody for IF. Representative results for IF assays carried out using 1:50, 1:100, 1:500, 1:750 and 1:1000 mouse-anti-H3K9ac primary antibody, as indicated, with anti-mouse-ATTO488 secondary antibody (green). Parasite nuclei were stained with DAPI (blue). Scale bars=3 µm.

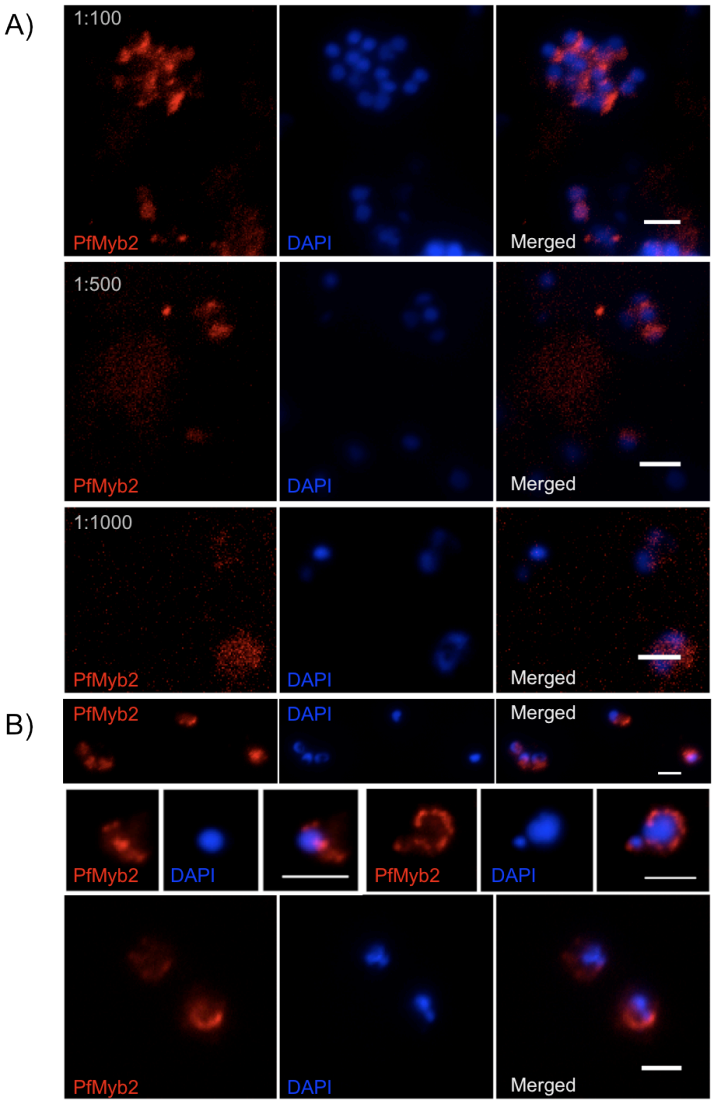

Figure A-5: Titration of anti-PfMyb2 antibody for IF. A) Representative results for IF assays carried out using 1:100, 1:500 and 1:1000 chicken-anti-PfMyb2 primary antibody, as indicated, with anti-chicken-TMR secondary antibody (red). The parasite nuclei were stained with DAPI (blue). B) Additional representative images of PfMyb2 labeling at 1:100 dilution. Scale bars=3 µm.

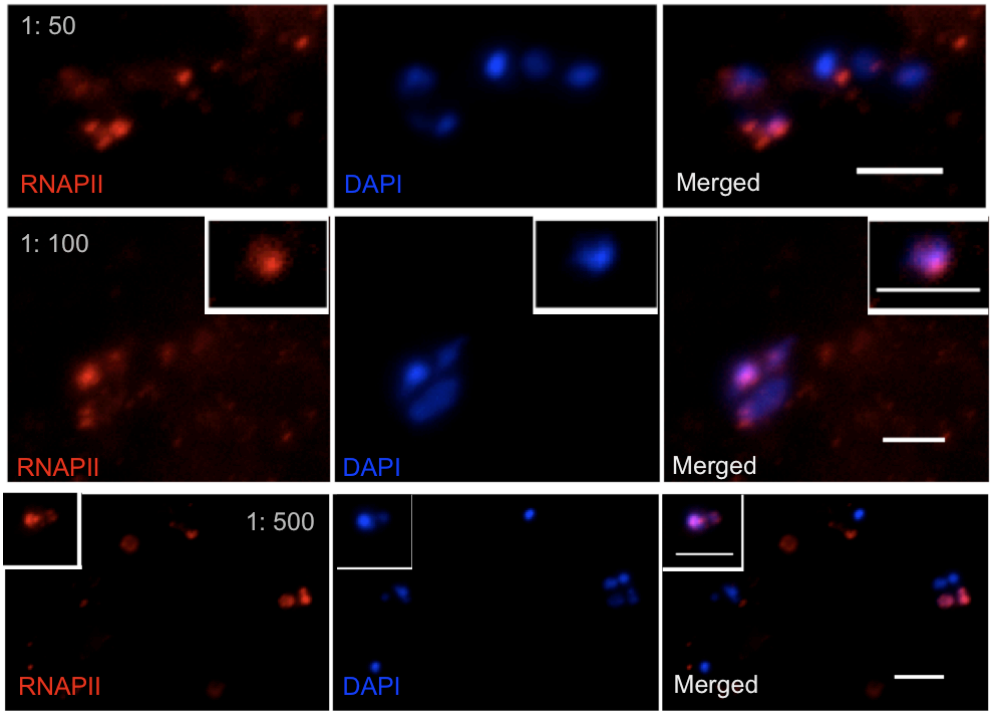

Figure A-6: Titration of anti-RNAPII antibody for IF. Representative results for IF assays carried out using 1:50, 1:100 and 1:500 rabbit-anti-RNAPII primary antibody, as indicated, with anti-rabbit-Alexafluor594 secondary antibody (red). The parasite nuclei were stained with DAPI (blue). Scale bars=3 µm.

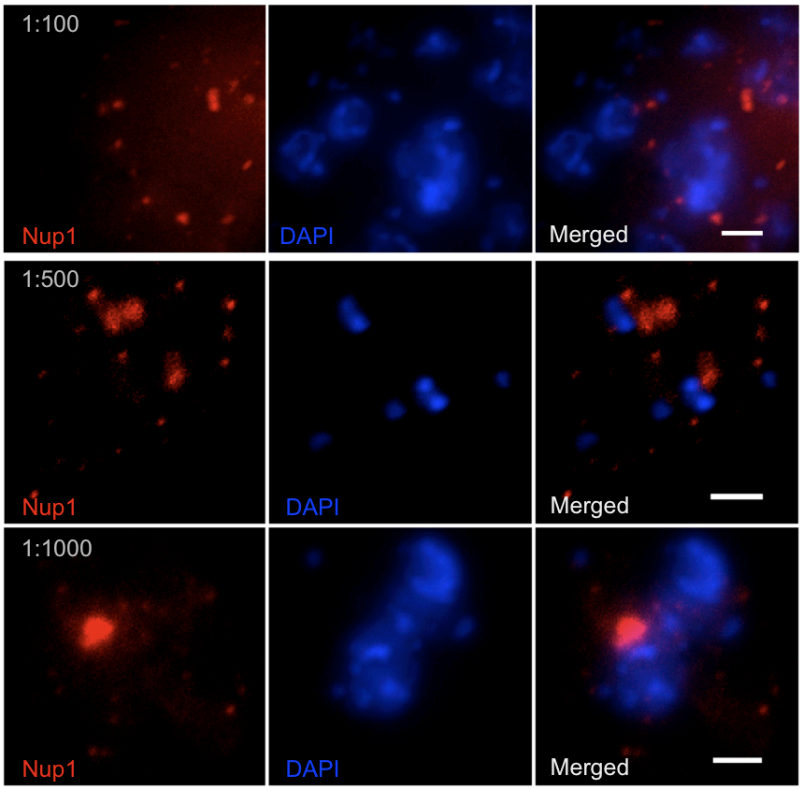

Figure A-7: Titration and testing of anti-PfNup antibody for IF. Representative results for IF assays carried out using 1:100, 1:500 and 1:1000 rat-anti-PfNup1 primary antibody, as indicated, with anti-rat-CY5 secondary antibody (red). The parasite nuclei were stained with DAPI (blue). Scale bars =3 µm.

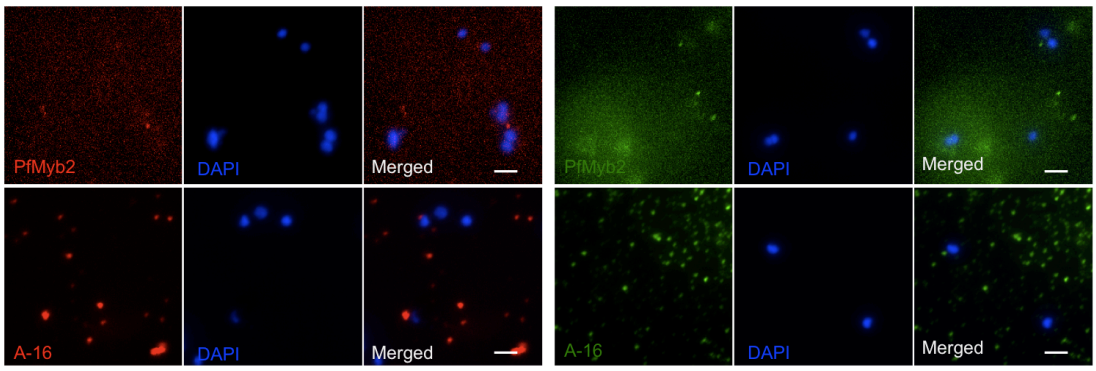

Figure A-8: IF results using fluorophore-conjugated primary antibodies. Representative images of primary IF using unpurified anti-PfMyb2 and anti-fibrillarin A-16, directly conjugated to ATTO488 (green) and FluoProbe647H (red), as labeled. The parasite nuclei were stained with DAPI (blue). Scale bar =3 µm.

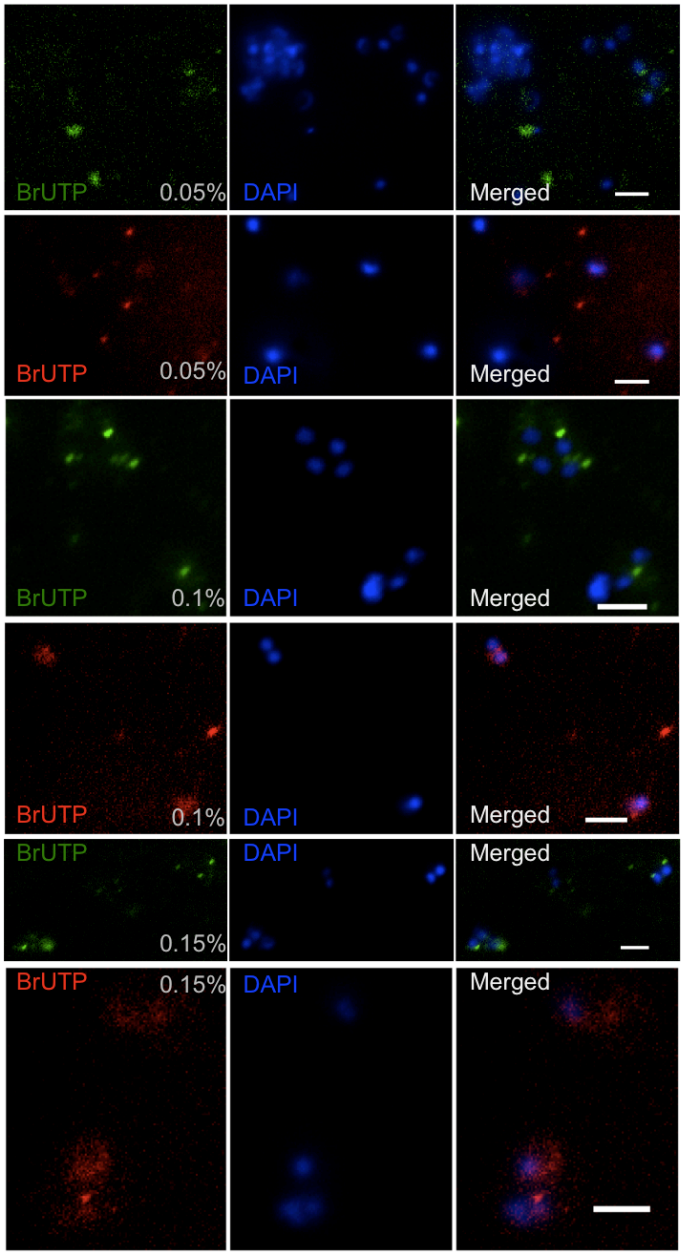

Figure A-9: Titration of saponin lysis and permeabilisation of parasites prior to BrUTP incorporation. Representative figures of anti-BrUTP IF, after BrUTP was incorporated in samples treated to saponin lysis at 0.05%, 0.10% and 0.15% saponin, as indicated in the images. Incorporated BrUTP was detected with 1:100 mouse anti-BrUTP and 1:500 rabbit-anti-mouse-ATTO488 (green) or rabbit-anti-mouse-ATTO565 (red). The parasite nuclei were stained with DAPI (blue). Scale bars=3 µm.

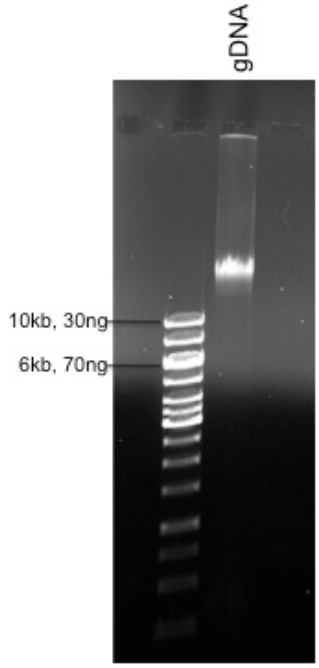

Figure A-10: Agarose gel of extracted gDNA from *P. falciparum*. Left lane: 1kb DNA ladder. Right lane: 0.5 µg extracted gDNA (approx. 20 kb, 25 ng/µl).

Appendix A.3. smFISH probe sequences.

Table A-1: List of smFISH oligonucleotide probes and sequences for the detection of IMP-DHG, CTPSynth And AdSucSynth transcripts

Probe Name	Probe Sequence (5' to 3')
IMP-DH1	aacttcatctgctttccatc
IMP-DH2	atatgtataggacatgacgc
IMP-DH3	tccgggcatacatattatgt
IMP-DH4	gcgttatgttatctgtcata
IMP-DH5	gagatgatattaccggtgtt
IMP-DH6	ttatgtcccgttactgtatc
IMP-DH7	caaagctaaagctattgaca
IMP-DH8	atgaatcacacctaaaccac
IMP-DH9	cctcttcaatttgcttttct
IMP-DH10	cattctcaaacctcttaacc
IMP-DH11	gggaaaatgtataaggatca
IMP-DH12	acatctgctacagtatgttc
IMP-DH13	ccaacacgattctttgtttc
IMP-DH14	ctactgttatcggatatgat
IMP-DH15	aatttagaacctaccttacc
IMP-DH16	caacacctgttattatacca

IMP-DH17	caccgatcttcatactttta
IMP-DH18	ctgtaacaacatcagttgtc
IMP-DH19	gcatcagataaatttatggg
IMP-DH20	ggaagaacacttttttttc
IMP-DH21	cgacatactaaagctataag
IMP-DH22	cgcatggggaaatattctat
IMP-DH23	cgatatagatgcacctacaa
IMP-DH24	gctctttctaaatcatgttc
IMP-DH25	ccttgtgatgaatctataca
IMP-DH26	ctggatgagctgatttaatt
IMP-DH27	cattaccaccaataattgga
IMP-DH28	tttgcttgttgagaagtaac
IMP-DH29	ctgcacctgcatctattaaa
IMP-DH30	cccataccaatacgtaaaac
IMP-DH31	tgttgtacaaattgaaccac
IMP-DH32	tacctacagcacatacatct
IMP-DH33	ataaacagctgttccttgtg
IMP-DH34	gtatgagcatatttacttac
IMP-DH35	cctccatctgcaatagtttt
IMP-DH36	gccttcacaatattacctga
IMP-DH37	caaaatctgctcctaaagat

IMP-DH38	ctgccaacaaatttcctaac
IMP-DH39	tcactgcaactttcttcagt
IMP-DH40	cggacgttattttcaaaata
IMP-DH41	catactacccatacctctat
IMP-DH42	ctacttttgaattgaatcc
IMP-DH43	gatactccttgagagacttt
IMP-DH44	gaccgatcctttatctacta
IMP-DH45	gctttgaatagatgtggaat
IMP-DH46	actctggaatccatgtttta
IMP-DH47	ctggaatgtttcttataccc
IMP-DH48	cactgactttaccttcttta
AdSucSyn1	tgatgatcaaatatgttcat
AdSucSyn2	ctacattccctttatccaca
AdSucSyn3	cattgtgcacctaatattgc
AdSucSyn4	ttttcctttcccttcatcac
AdSucSyn5	gaatattctgataacatatc
AdSucSyn6	gcacctccattaaatctaca
AdSucSyn7	tgatatcgtatgtcctgcat
AdSucSyn8	gtaaagcatatttcttatca
AdSucSyn9	catataatacaccacatggt
AdSucSyn10	ccgtttcctaatacacttat

AdSucSyn11	tgattttacatgtattacca
AdSucSyn12	ctgattcaatttcttccatt
AdSucSyn13	tctatctaacaactttcccc
AdSucSyn14	gtgctttatttgataaatat
AdSucSyn15	cgtttcttggattgaatcaa
AdSucSyn16	gtacctatttgttttccttc
AdSucSyn17	tggtccaatacctcttttg
AdSucSyn18	ctggaagctttagtagaata
AdSucSyn19	agttcctaatcttataccta
AdSucSyn20	ccattaagtggtctattaat
AdSucSyn21	gagttctttttctttgtcat
AdSucSyn22	ctcttaactttaagtgataa
AdSucSyn23	ggaaataacatcaactattc
AdSucSyn24	gttttctaaatttgtattca
AdSucSyn25	gcaccttcaattaatacttt
AdSucSyn26	caatatctaacatagctgca
AdSucSyn27	gttacatatggatatgttcc
AdSucSyn28	accaactgttgtacagctac
AdSucSyn29	attccaagtcctgagaaaac
AdSucSyn30	cacctacaactaaattcagt
AdSucSyn31	ccaactctggttaagtaact

AdSucSyn32	attcagttaagaaagggcca
AdSucSyn33	cttaaatattgaccaacgtc
AdSucSyn34	cgttccatattcatgacctt
AdSucSyn35	accttcttggtctcttggta
AdSucSyn36	ataacattggtatgtcgagc
AdSucSyn37	ctattaatgcacttaacata
AdSucSyn38	ccagataaaacatccaattt
AdSucSyn39	cacacaataatatttcctct
AdSucSyn40	caagcagttctcctgttttt
AdSucSyn41	tttcttcttcaacagggtag
AdSucSyn42	acaggttcatattcttctga
AdSucSyn43	ccatccactgaatttttcat
AdSucSyn44	tacaagttgagatgtcttct
AdSucSyn45	gcattttctggtaattcatc
AdSucSyn46	ccaaactattggagttttta
AdSucSyn47	ttctattaggacctacacca
AdSucSyn48	ggttaaaattctttttaact
CTPSyn1	tcatcatctacactatccat
CTPSyn2	ccggtcacaatgatgtattt
CTPSyn3	accaagtccactcatattac
CTPSyn4	tactactcatagctgttcct

CTPSyn5	cgttcctgcatcaatgttta
CTPSyn6	tctccatgttcatatggaga
CTPSyn7	cccccatcttctaatacata
CTPSyn8	cgctcataatttcctaaatc
CTPSyn9	cctaagtattcacctttcg
CTPSyn10	tggtactacttgtaccgttt
CTPSyn11	tttggatagcatccgttaca
CTPSyn12	ggcacatacaagggatttta
CTPSyn13	aatatcaccaacagtaccac
CTPSyn14	ggcttctaaatatacagctg
CTPSyn15	gacatagacatacatcatca
CTPSyn16	ctgttctcttagatttccaa
CTPSyn17	ctatgttgtgtaggttttgt
CTPSyn18	ggttttaatcctgcttctct
CTPSyn19	gcttcttgtgttaatggttc
CTPSyn20	ctgcgagttgtttccatata
CTPSyn21	cttgttcgcttgatgattca
CTPSyn22	gatgctgtatatttccctac
CTPSyn23	ccacattctaaacatgcatg
CTPSyn24	cataggagtatttccttgct
CTPSyn25	ctgtactactgttttcatgg

CTPSyn26	cagaagtggtatcatctaca
CTPSyn27	cccaggccttttcatatttt
CTPSyn28	cccatccacagattttaatg
CTPSyn29	caaatcctccaggtactaaa
CTPSyn30	tttccttcgatacctctagt
CTPSyn31	gggtatattatgtaaacggc
CTPSyn32	gcattcctaagcatattcct
CTPSyn33	gctacatctatgacagctat
CTPSyn34	ctccgaatttgcattcacat
CTPSyn35	cgacattttcgacattttcc
CTPSyn36	ctcgtttatatgaacactcg
CTPSyn37	ctgttgtatcttgactacag
CTPSyn38	gccaattctttcggattatg
CTPSyn39	catgtttttgacgttctgta
CTPSyn40	ctgtcatatatgtatcttgg
CTPSyn41	ggatctgtatcatcatacgt
CTPSyn42	ctcccttattatcatcacct
CTPSyn43	tgattgtttcacacctagac
CTPSyn44	cagcttctaataagggtaca
CTPSyn45	ggatgaaattgaacacctac
CTPSyn46	gacttaaatggtctcgaagt

CTPSyn47	gatgctaacacaaatgcaag
CTPSyn48	cctgaacataacttattgcc

Appendix A.4. smFISH probe conjugation and purification results.

Table A-2: Amount of DNA remaining after each precipitation step during smFISH probe conjugation with fluorophores.

Target gene transcripts	Fluorophore	Pooled probes starting amount		After first precipitation		After conjugation and precipitation	
		concentration (ng/ul)	total DNA (ng)	concentration (ng/ul)	total DNA (ng)	concentration (ng/ul)	total DNA (ng)
IMP-DHG		1499	719520	3194,3	638860		
	ATTO647N					447,3	89460
	ATTO495					1640,7	328140
CTP-Synth		1233,7	592176	2750,9	550180		
	ATTO647N					594,9	118980
	ATTO495					1470,7	294140
AdSuc Synth		1186,5	569520	2538,4	507680		
	ATTO647N					357,2	71440
	ATTO495					1411,3	282260

A) CTPSynth- ATTO647N

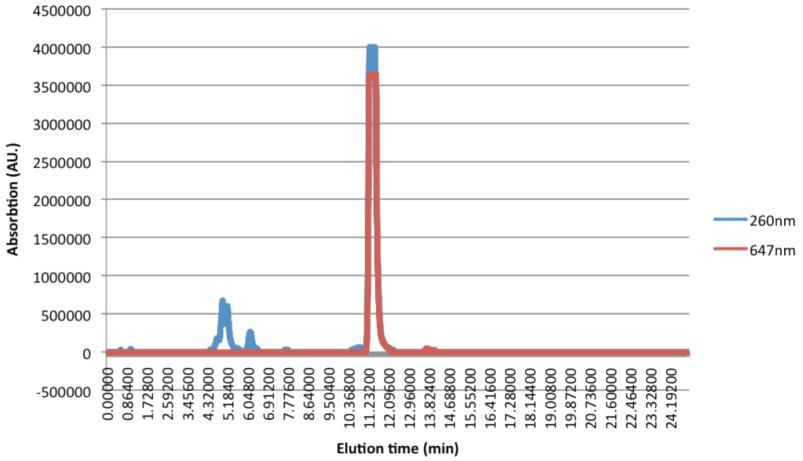

B) AdSucSynth -ATTO647N

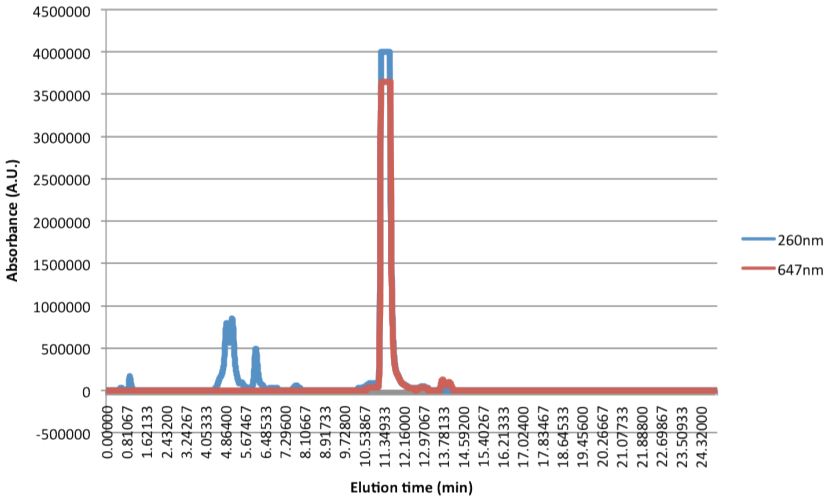

C) IMP-DHG- ATTO647N

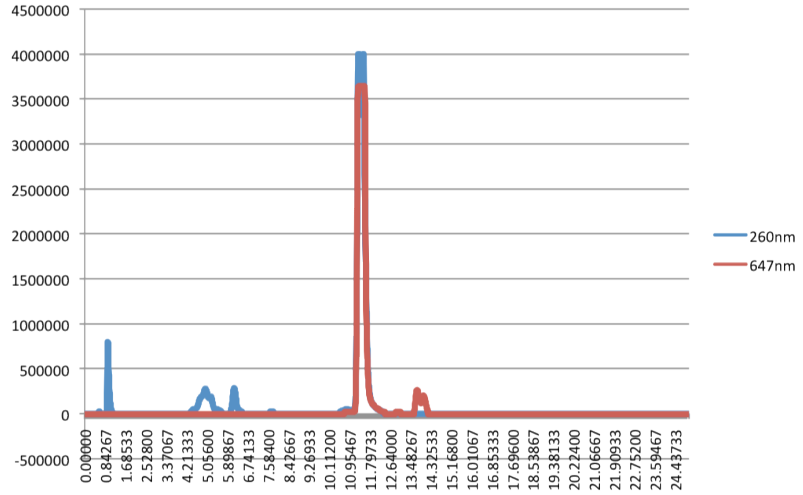

Figure A-11 (previous page): HPLC chromatograms of ATTO647N-conjugated smFISH probe purification. Elution profiles of conjugation reaction mixtures for the purification of ATTO647N-conjugated A) CTPSynthetase , B) Adenyl Succinate Synthetase and C) IMP-dehydrogenase probes. Unconjugated probe elutes as a peak in the 260 nm channel only; fluorophore-conjugated probe is detected as peaks in both the 260 nm and 647 nm channels and unconjugated fluorophore elutes as a peak in the 647 nm channel only.

A) CTPSynth –ATTO495

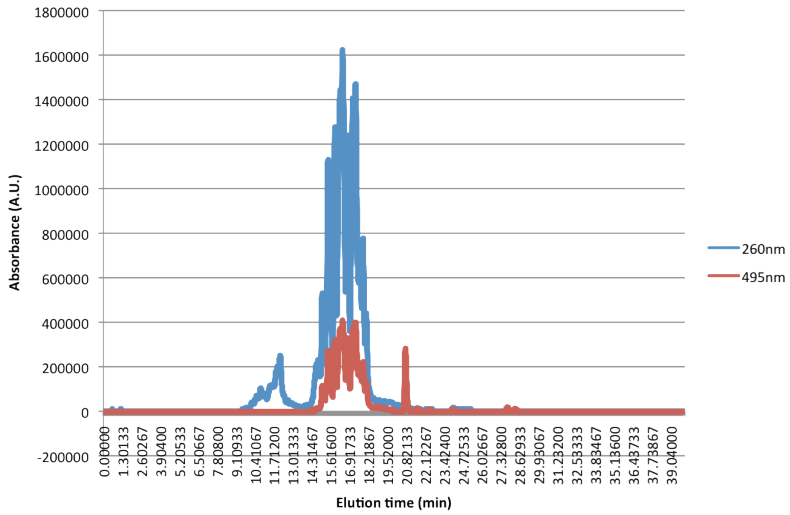

B) AdSucSynth –ATTO495

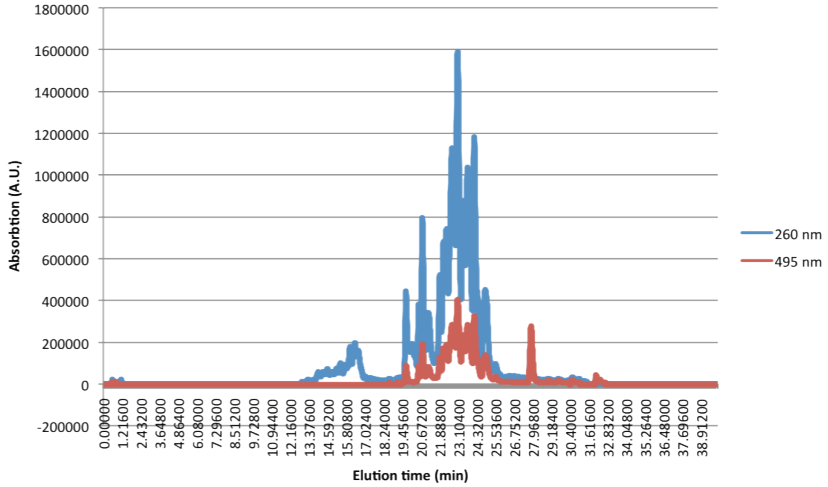

C) IMP-DHG –ATTO495

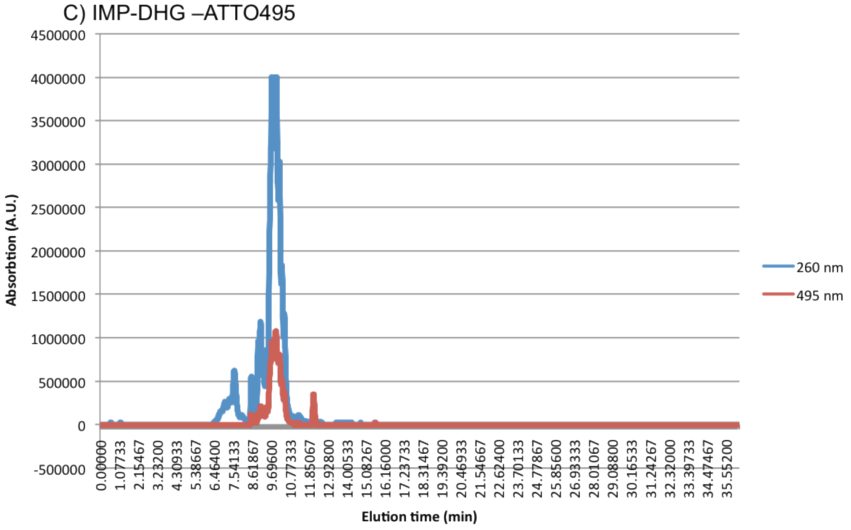

Figure A-12 (previous page): HPLC chromatograms of ATTO495-conjugated smFISH probe purification. Elution profiles of conjugation reaction mixtures for the purification of ATTO495-conjugated A) CTPSynthetase , B) Adenyl Succinate Synthetase and C) IMP-dehydrogenase probes. Unconjugated probe elutes as a peak in the 260 nm channel only; fluorophore-conjugated probe is detected as peaks in both the 260 nm and 495 nm channels and unconjugated fluorophore elutes as a peak in the 495 nm channel only.

Appendix B.2. Additional fluorescent labeling results

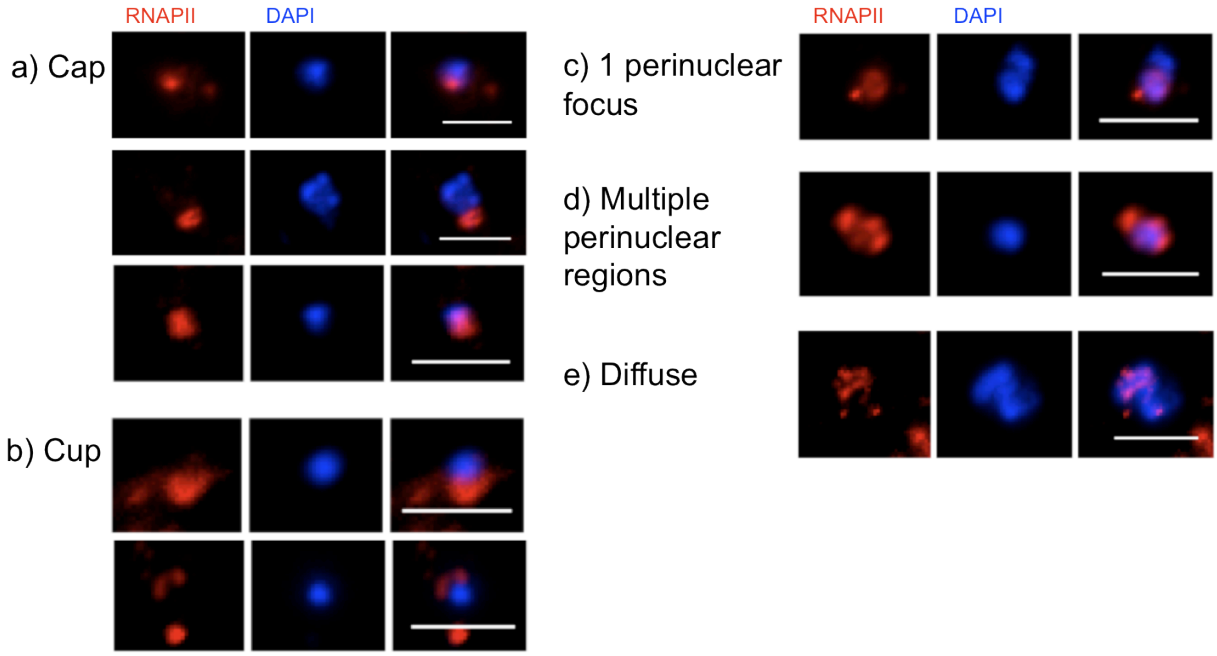

Figure B-1: IF labeling of RNAPII can be assigned to similar classes as those used for PfMyb2 labeling. Representative images of RNAPII labeling (red) that adopt similar sub-nuclear distribution patterns to the a) cap, b) cup, c) single perinuclear foci, d) multiple perinuclear regions and d) diffuse labeling, commonly observed with PfMyb2 labeling. Nuclei are labeled with DAPI (blue). Scale bars =3 μm.

Appendix A.1. Additional information regarding STORM

The resolution of light microscopy is limited by the diffraction of light as it passes through different media. This diffraction perturbs or broadens the image of an object such that, if two objects are closer than a particular distance, the resolution limit, then their images start to overlap and interfere with each other's and they cannot be distinguished. This resolution limit is dependent on the wavelength of light, but for most purposes can be considered to be approximately 200nm (Abbe, 1873).

The diffraction of an image can be approximated by a mathematical function, a Gaussian distribution, such that, if we were to image just one object, or in the case of fluorescent microscopy, one fluorophore, we can calculate the original signal, and determine the centre of mass of the object with an accuracy greater than the resolution limit. STORM (Rust *et al*., 2006; reviewed in McEvoy *et al*., 2010 and Henriques *et al*., 2011) makes use of this principle by modulating the emission profile of a population of fluorophores such that they repeatedly cycle through the light and dark states, or "blink", in a stochastic manner. Thus only a subset of the fluorophore population in a sample emits signal at any given time and signal from a limited number of fluorophores, with non-overlapping images, can be detected in a given moment. By acquiring a series of multiple (1000's to 100000's) sequential images for a single field of view, images of the majority of the fluorophores in a sample can be acquired where no surrounding fluorophores are emitting signal. The centre of mass of each object in a field of view can then be accurately calculated. A localisation accuracy of up to 20nm can be attained for such an acquisition procedure. This accuracy, or resolution, is dependent primarily on the brightness of the fluorophore signal in relation to background signal, or the signal-to-noise-ratio (SNR) (Henriques *et al*., 2011).

Modulation of the emission profile of fluorophores is achieved using high intensity light of two different wavelengths to stimulate the fluorophore to emit light, and to then force it back down to the dark ground state. In addition, the inclusion of oxidizing and reducing agents in the imaging buffer establishes a redox system in the imaging environment. This serves to protect the fluorophore from permanent photobleaching, as well as assist the fluorophore in cycling between the light and dark

states, via an ill-defined triplet state (Vogelsang *et al.,* 2008, reviewed by Henriques *et al*., 2011) (Figure A-1).

The QuickPALM processing algorithm (Henriques *et al*., 2010), uses a CLEAN algorithm to process each detected signal in each of the 1000's to 100000's of images acquired for a single STORM acquisition. The algorithm assesses the size (diameter), symmetry and circularity and SNR. Based on these criteria, the QuickPALM algorithm determines the likelihood of each point signal being signal from a single sub-diffractive molecule (fluorophore). If a signal meets these criteria, it is deemed a true object, and the centre of mass of the signal is calculated. The centre of mass determined for each object in each frame is plotted onto a single image to build a super-resolution reconstruction of the original data set.

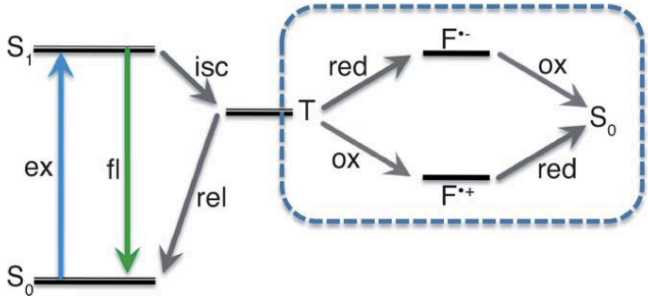

Figure A-1: Schematic of the cycling of fluorophores between the light and dark states, via the triplet state. The absorbtion of a photon by a ground state (S_0) fluorophore excites the fluorohphore (ex) such that it occupies a singlet state (S_1). The fluorophore may return to the ground state by emitting energy as light (fl). Alternatively, a fluorophore occasionally enters the dark triplet state (T) by a process called intersystem crossing (isc). From the unstable triplet state, the fluorophore is particularly susceptible to permanent oxidative photobleaching, so that spontaneous relaxation back to the ground state (rel) is a rare occurrence. Within the boxed region: The presence of oxidizing and reducing agents in the imaging environment protects the triplet state from reactive oxygen species. Electron transfer reactions with the redox reagents result in fluorophore radicals ($F^{\bullet+}$ and $F^{\bullet-}$). These unstable forms are retrieved back to the ground state by the reciprocal reduction or oxidation reaction. This process allows the fluorophore to cycle between dark (ground and triplet) and light (singlet) states while avoiding photobleaching. Taken from Henriques *et al*. (2011).

Appendix A.2. Additional results from assay optimisations in Chapter 2.

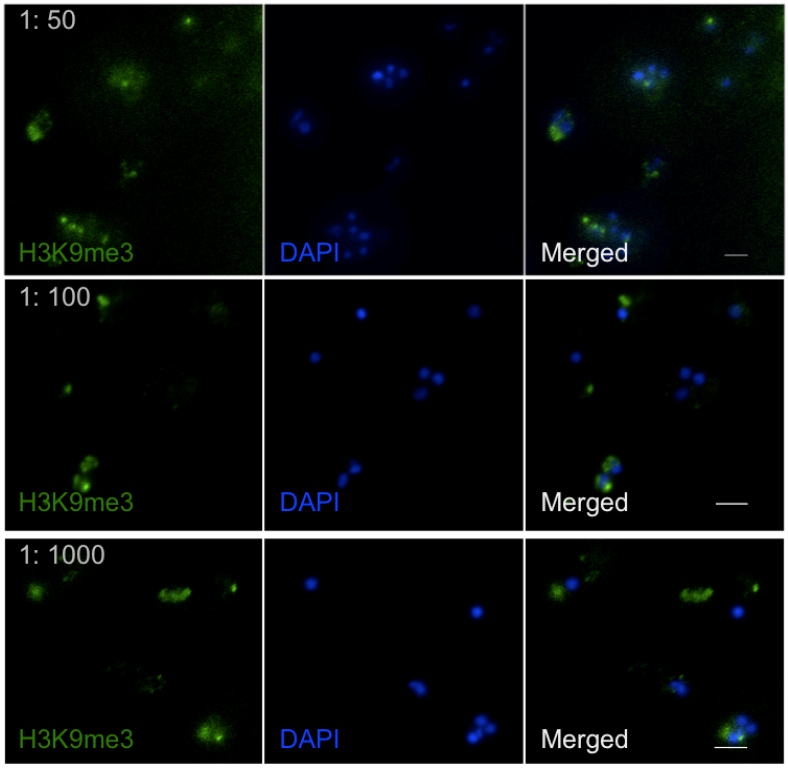

Figure A-2: Titration of mouse-anti-H3K9me3 antibody for IF. Representative results for IF assays carried out using 1:50, 1:100 and 1:1000 mouse-anti-H3K9me3 primary antibody, as indicated, with anti-mouse-ATTO488 secondary antibody (green). Parasite nuclei were stained with DAPI (blue). Scale bars=3 µm.

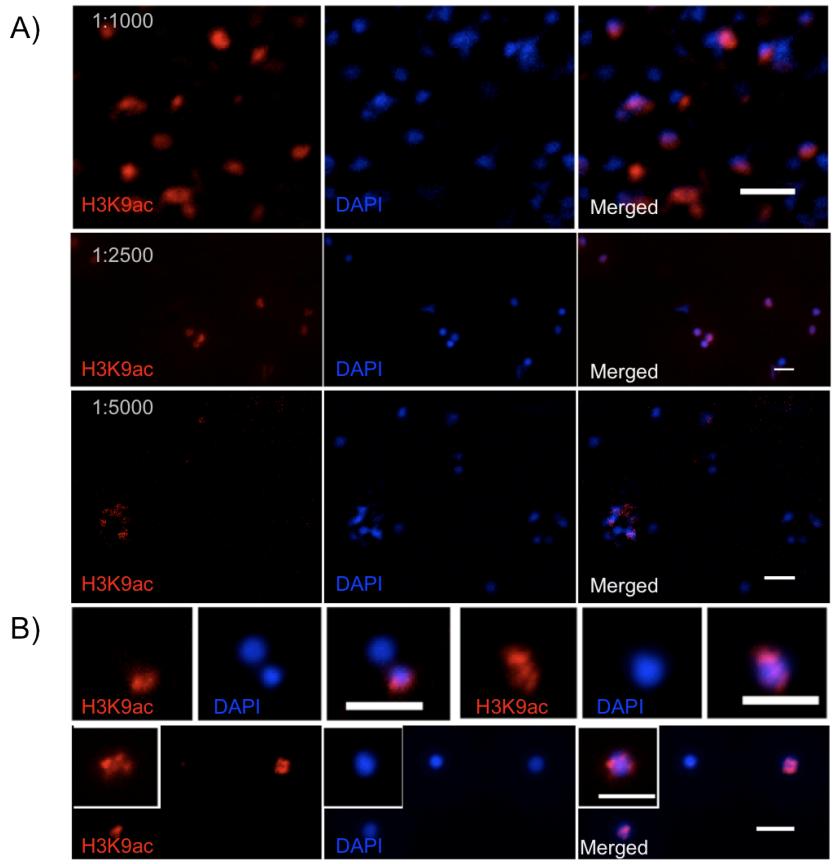

Figure A-3: Titration of rabbit-anti-H3K9ac antibody for IF. A) Representative results for IF assays carried out using 1:1000, 1:2500 and 1:5000 rabbit-anti-H3K9ac primary antibody, as indicated, with anti-rabbit-AlexaFluor532 secondary antibody (red). B) Additional representative images of H3K9ac labeling at 1:2000 – 1:2500 dilution. Parasite nuclei were stained with DAPI (blue). Scale bars=3 µm.

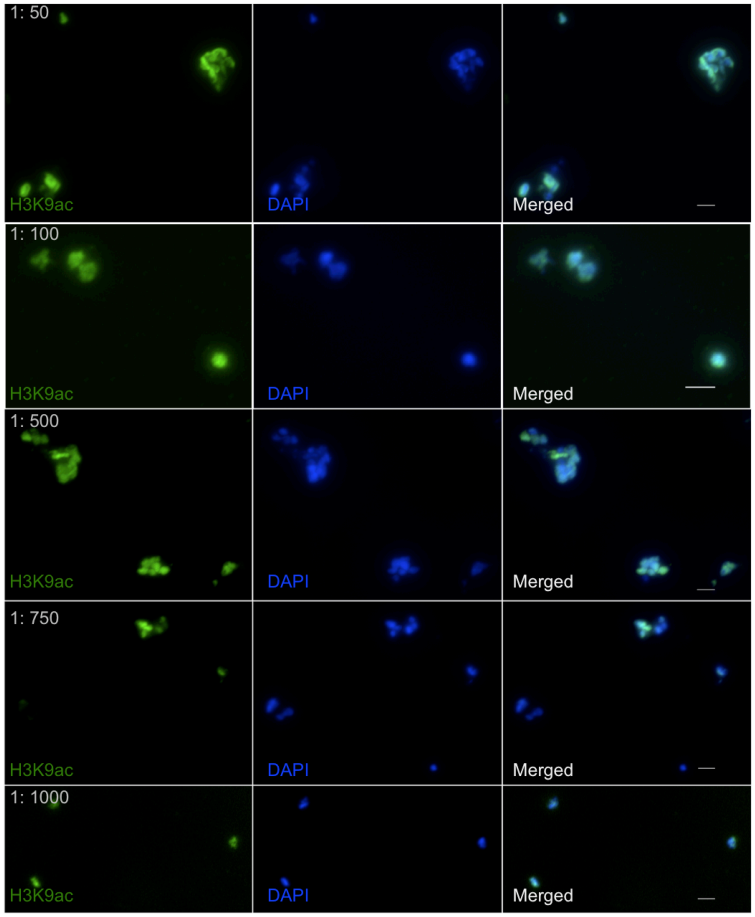

Figure A-4: Titration of mouse-anti-H3K9ac antibody for IF. Representative results for IF assays carried out using 1:50, 1:100, 1:500, 1:750 and 1:1000 mouse-anti-H3K9ac primary antibody, as indicated, with anti-mouse-ATTO488 secondary antibody (green). Parasite nuclei were stained with DAPI (blue). Scale bars=3 µm.

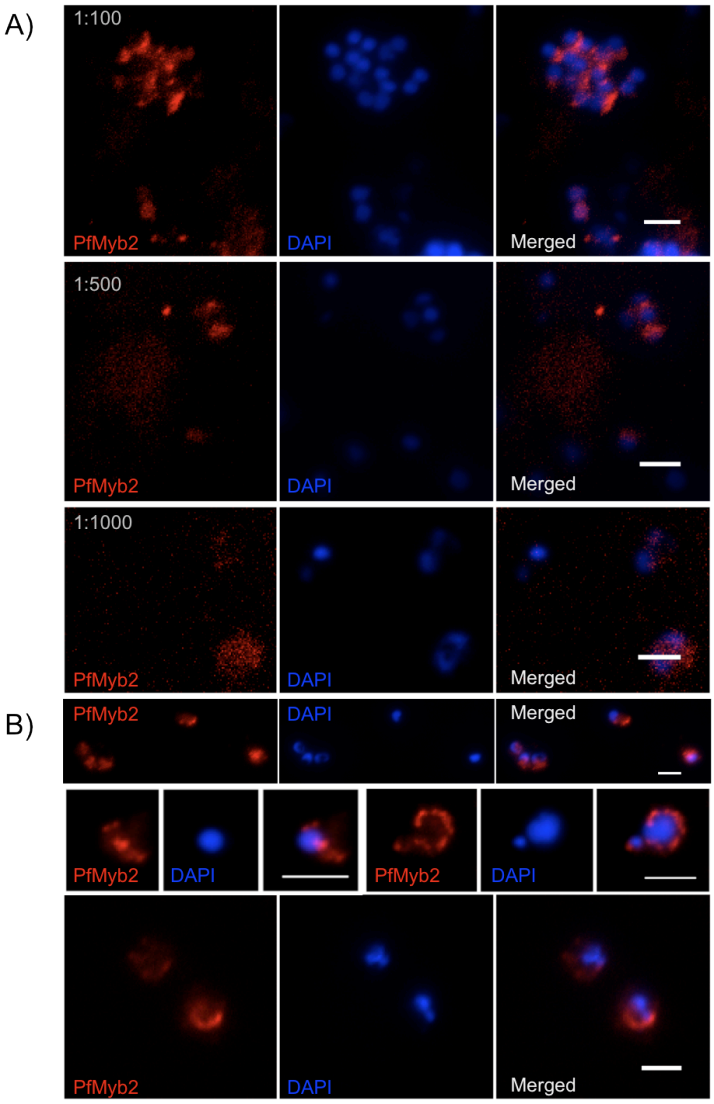

Figure A-5: Titration of anti-PfMyb2 antibody for IF. A) Representative results for IF assays carried out using 1:100, 1:500 and 1:1000 chicken-anti-PfMyb2 primary antibody, as indicated, with anti-chicken-TMR secondary antibody (red). The parasite nuclei were stained with DAPI (blue). B) Additional representative images of PfMyb2 labeling at 1:100 dilution. Scale bars=3 µm.

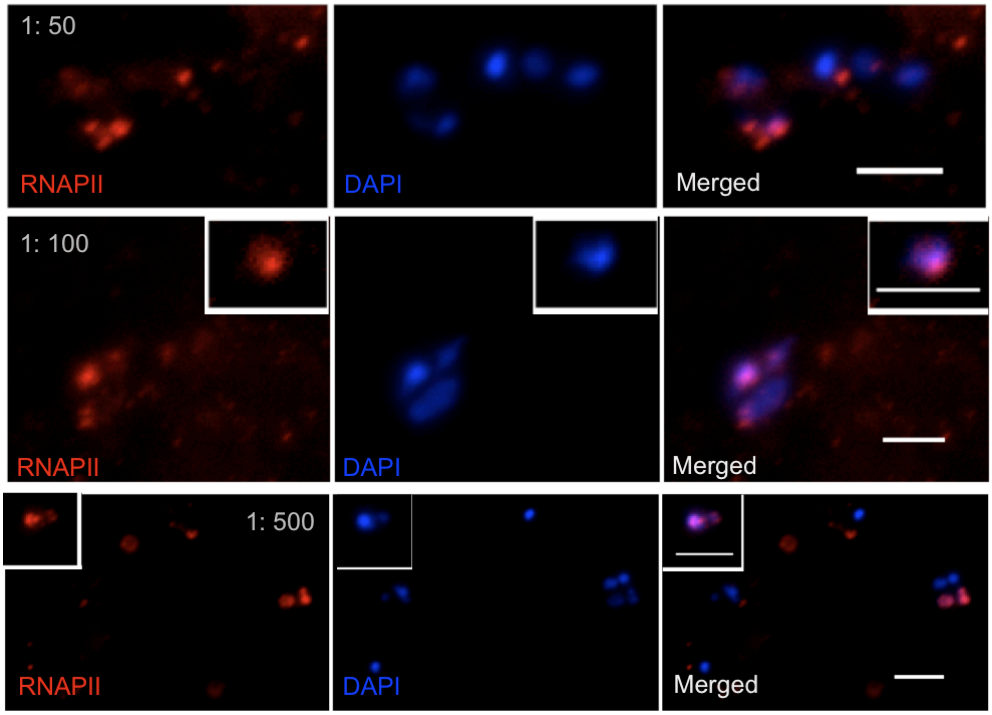

Figure A-6: Titration of anti-RNAPII antibody for IF. Representative results for IF assays carried out using 1:50, 1:100 and 1:500 rabbit-anti-RNAPII primary antibody, as indicated, with anti-rabbit-Alexafluor594 secondary antibody (red). The parasite nuclei were stained with DAPI (blue). Scale bars=3 µm.

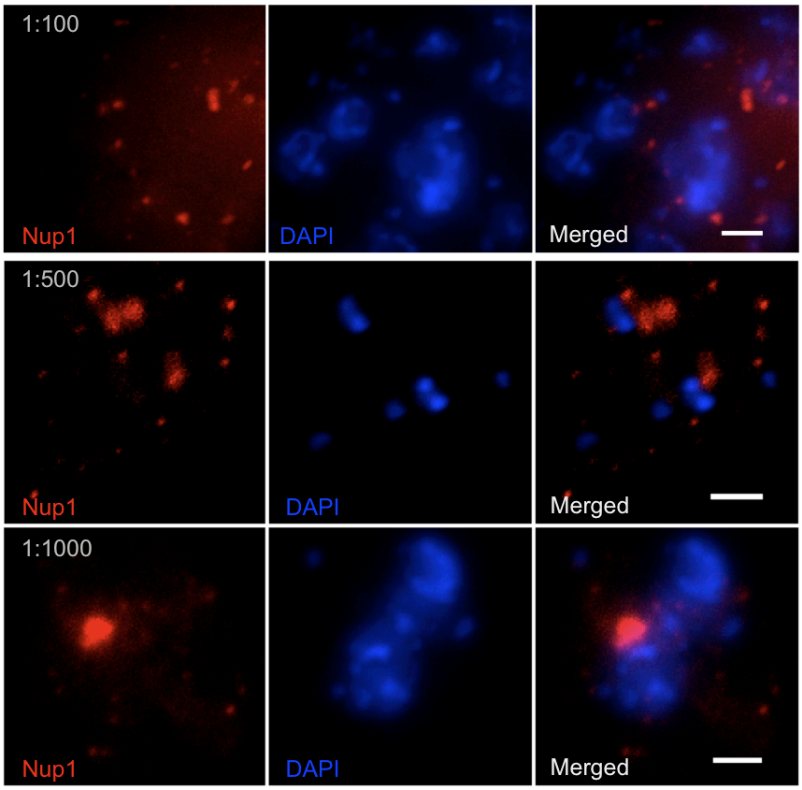

Figure A-7: Titration and testing of anti-PfNup antibody for IF. Representative results for IF assays carried out using 1:100, 1:500 and 1:1000 rat-anti-PfNup1 primary antibody, as indicated, with anti-rat-CY5 secondary antibody (red). The parasite nuclei were stained with DAPI (blue). Scale bars =3 µm.

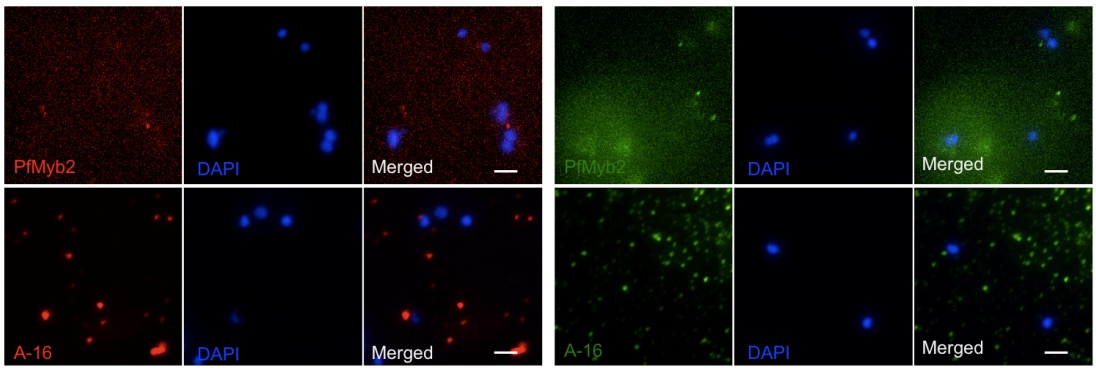

Figure A-8: IF results using fluorophore-conjugated primary antibodies. Representative images of primary IF using unpurified anti-PfMyb2 and anti-fibrillarin A-16, directly conjugated to ATTO488 (green) and FluoProbe647H (red), as labeled. The parasite nuclei were stained with DAPI (blue). Scale bar =3 µm.

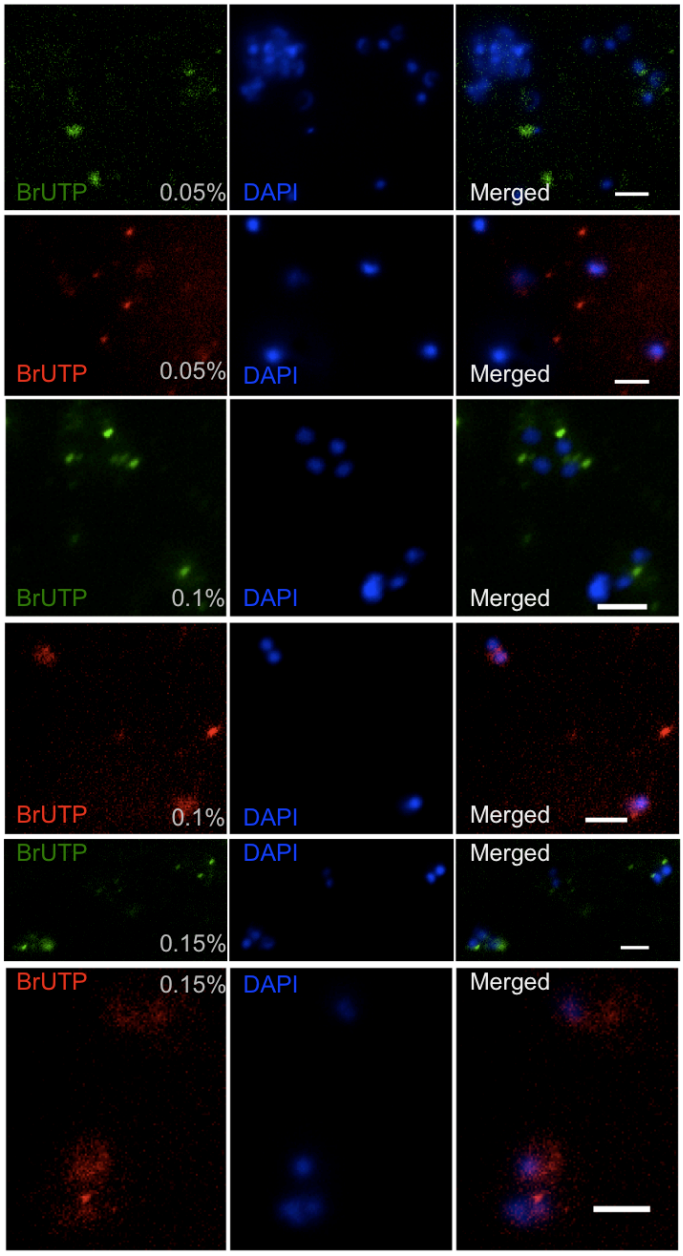

Figure A-9: Titration of saponin lysis and permeabilisation of parasites prior to BrUTP incorporation. Representative figures of anti-BrUTP IF, after BrUTP was incorporated in samples treated to saponin lysis at 0.05%, 0.10% and 0.15% saponin, as indicated in the images. Incorporated BrUTP was detected with 1:100 mouse anti-BrUTP and 1:500 rabbit-anti-mouse-ATTO488 (green) or rabbit-anti-mouse-ATTO565 (red). The parasite nuclei were stained with DAPI (blue). Scale bars=3 µm.

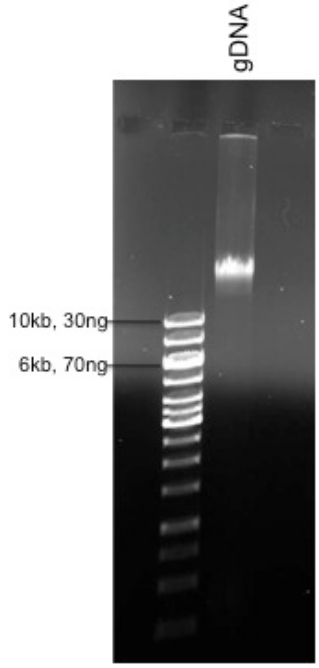

Figure A-10: Agarose gel of extracted gDNA from *P. falciparum*. Left lane: 1kb DNA ladder. Right lane: 0.5 µg extracted gDNA (approx. 20 kb, 25 ng/µl).

Appendix A.3. smFISH probe sequences.

Table A-1: List of smFISH oligonucleotide probes and sequences for the detection of IMP-DHG, CTPSynth And AdSucSynth transcripts

Probe Name	Probe Sequence (5' to 3')
IMP-DH1	aacttcatctgctttccatc
IMP-DH2	atatgtataggacatgacgc
IMP-DH3	tccgggcatacatattatgt
IMP-DH4	gcgttatgttatctgtcata
IMP-DH5	gagatgatattaccggtgtt
IMP-DH6	ttatgtcccgttactgtatc
IMP-DH7	caaagctaaagctattgaca
IMP-DH8	atgaatcacacctaaaccac
IMP-DH9	cctcttcaatttgcttttct
IMP-DH10	cattctcaaacctcttaacc
IMP-DH11	gggaaaatgtataaggatca
IMP-DH12	acatctgctacagtatgttc
IMP-DH13	ccaacacgattctttgtttc
IMP-DH14	ctactgttatcggatatgat
IMP-DH15	aatttagaacctaccttacc
IMP-DH16	caacacctgttattatacca

IMP-DH17	caccgatcttcatactttta
IMP-DH18	ctgtaacaacatcagttgtc
IMP-DH19	gcatcagataaatttatggg
IMP-DH20	ggaagaacacttttttttc
IMP-DH21	cgacatactaaagctataag
IMP-DH22	cgcatggggaaatattctat
IMP-DH23	cgatatagatgcacctacaa
IMP-DH24	gctctttctaaatcatgttc
IMP-DH25	ccttgtgatgaatctataca
IMP-DH26	ctggatgagctgatttaatt
IMP-DH27	cattaccaccaataattgga
IMP-DH28	tttgcttgttgagaagtaac
IMP-DH29	ctgcacctgcatctattaaa
IMP-DH30	cccataccaatacgtaaaac
IMP-DH31	tgttgtacaaattgaaccac
IMP-DH32	tacctacagcacatacatct
IMP-DH33	ataaacagctgttccttgtg
IMP-DH34	gtatgagcatatttacttac
IMP-DH35	cctccatctgcaatagtttt
IMP-DH36	gccttcacaatattacctga
IMP-DH37	caaaatctgctcctaaagat

IMP-DH38	ctgccaacaaatttcctaac
IMP-DH39	tcactgcaactttcttcagt
IMP-DH40	cggacgttattttcaaaata
IMP-DH41	catactacccatacctctat
IMP-DH42	ctacttttgaattgaatcc
IMP-DH43	gatactccttgagagacttt
IMP-DH44	gaccgatcctttatctacta
IMP-DH45	gctttgaatagatgtggaat
IMP-DH46	actctggaatccatgtttta
IMP-DH47	ctggaatgtttcttataccc
IMP-DH48	cactgactttaccttcttta
AdSucSyn1	tgatgatcaaatatgttcat
AdSucSyn2	ctacattccctttatccaca
AdSucSyn3	cattgtgcacctaatattgc
AdSucSyn4	ttttcctttcccttcatcac
AdSucSyn5	gaatattctgataacatatc
AdSucSyn6	gcacctccattaaatctaca
AdSucSyn7	tgatatcgtatgtcctgcat
AdSucSyn8	gtaaagcatatttcttatca
AdSucSyn9	catataatacaccacatggt
AdSucSyn10	ccgtttcctaatacacttat

AdSucSyn11	tgattttacatgtattacca
AdSucSyn12	ctgattcaatttcttccatt
AdSucSyn13	tctatctaacaactttcccc
AdSucSyn14	gtgctttatttgataaatat
AdSucSyn15	cgtttcttggattgaatcaa
AdSucSyn16	gtacctatttgttttccttc
AdSucSyn17	tggtccaatacctcttttg
AdSucSyn18	ctggaagctttagtagaata
AdSucSyn19	agttcctaatcttataccta
AdSucSyn20	ccattaagtggtctattaat
AdSucSyn21	gagttctttttctttgtcat
AdSucSyn22	ctcttaactttaagtgataa
AdSucSyn23	ggaaataacatcaactattc
AdSucSyn24	gttttctaaatttgtattca
AdSucSyn25	gcaccttcaattaatacttt
AdSucSyn26	caatatctaacatagctgca
AdSucSyn27	gttacatatggatatgttcc
AdSucSyn28	accaactgttgtacagctac
AdSucSyn29	attccaagtcctgagaaaac
AdSucSyn30	cacctacaactaaattcagt
AdSucSyn31	ccaactctggttaagtaact

AdSucSyn32	attcagttaagaaagggcca
AdSucSyn33	cttaaatattgaccaacgtc
AdSucSyn34	cgttccatattcatgacctt
AdSucSyn35	accttcttggtctcttggta
AdSucSyn36	ataacattggtatgtcgagc
AdSucSyn37	ctattaatgcacttaacata
AdSucSyn38	ccagataaaacatccaattt
AdSucSyn39	cacacaataatatttcctct
AdSucSyn40	caagcagttctcctgttttt
AdSucSyn41	tttcttcttcaacagggtag
AdSucSyn42	acaggttcatattcttctga
AdSucSyn43	ccatccactgaatttttcat
AdSucSyn44	tacaagttgagatgtcttct
AdSucSyn45	gcattttctggtaattcatc
AdSucSyn46	ccaaactattggagttttta
AdSucSyn47	ttctattaggacctacacca
AdSucSyn48	ggttaaaattctttttaact
CTPSyn1	tcatcatctacactatccat
CTPSyn2	ccggtcacaatgatgtattt
CTPSyn3	accaagtccactcatattac
CTPSyn4	tactactcatagctgttcct

CTPSyn5	cgttcctgcatcaatgttta
CTPSyn6	tctccatgttcatatggaga
CTPSyn7	cccccatcttctaatacata
CTPSyn8	cgctcataatttcctaaatc
CTPSyn9	cctaagtattcacctttcg
CTPSyn10	tggtactacttgtaccgttt
CTPSyn11	tttggatagcatccgttaca
CTPSyn12	ggcacatacaagggatttta
CTPSyn13	aatatcaccaacagtaccac
CTPSyn14	ggcttctaaatatacagctg
CTPSyn15	gacatagacatacatcatca
CTPSyn16	ctgttctcttagatttccaa
CTPSyn17	ctatgttgtgtaggttttgt
CTPSyn18	ggttttaatcctgcttctct
CTPSyn19	gcttcttgtgttaatggttc
CTPSyn20	ctgcgagttgtttccatata
CTPSyn21	cttgttcgcttgatgattca
CTPSyn22	gatgctgtatatttccctac
CTPSyn23	ccacattctaaacatgcatg
CTPSyn24	cataggagtatttccttgct
CTPSyn25	ctgtactactgttttcatgg

CTPSyn26	cagaagtggtatcatctaca
CTPSyn27	cccaggccttttcatatttt
CTPSyn28	cccatccacagattttaatg
CTPSyn29	caaatcctccaggtactaaa
CTPSyn30	tttccttcgatacctctagt
CTPSyn31	gggtatattatgtaaacggc
CTPSyn32	gcattcctaagcatattcct
CTPSyn33	gctacatctatgacagctat
CTPSyn34	ctccgaatttgcattcacat
CTPSyn35	cgacattttcgacattttcc
CTPSyn36	ctcgtttatatgaacactcg
CTPSyn37	ctgttgtatcttgactacag
CTPSyn38	gccaattctttcggattatg
CTPSyn39	catgtttttgacgttctgta
CTPSyn40	ctgtcatatatgtatcttgg
CTPSyn41	ggatctgtatcatcatacgt
CTPSyn42	ctcccttattatcatcacct
CTPSyn43	tgattgtttcacacctagac
CTPSyn44	cagcttctaataagggtaca
CTPSyn45	ggatgaaattgaacacctac
CTPSyn46	gacttaaatggtctcgaagt

CTPSyn47	gatgctaacacaaatgcaag
CTPSyn48	cctgaacataacttattgcc

Appendix A.4. smFISH probe conjugation and purification results.

Table A-2: Amount of DNA remaining after each precipitation step during smFISH probe conjugation with fluorophores.

Target gene transcripts	Fluorophore	Pooled probes starting amount		After first precipitation		After conjugation and precipitation	
		concentration (ng/ul)	total DNA (ng)	concentration (ng/ul)	total DNA (ng)	concentration (ng/ul)	total DNA (ng)
IMP-DHG		1499	719520	3194,3	638860		
	ATTO647N					447,3	89460
	ATTO495					1640,7	328140
CTP-Synth		1233,7	592176	2750,9	550180		
	ATTO647N					594,9	118980
	ATTO495					1470,7	294140
AdSuc Synth		1186,5	569520	2538,4	507680		
	ATTO647N					357,2	71440
	ATTO495					1411,3	282260

A) CTPSynth- ATTO647N

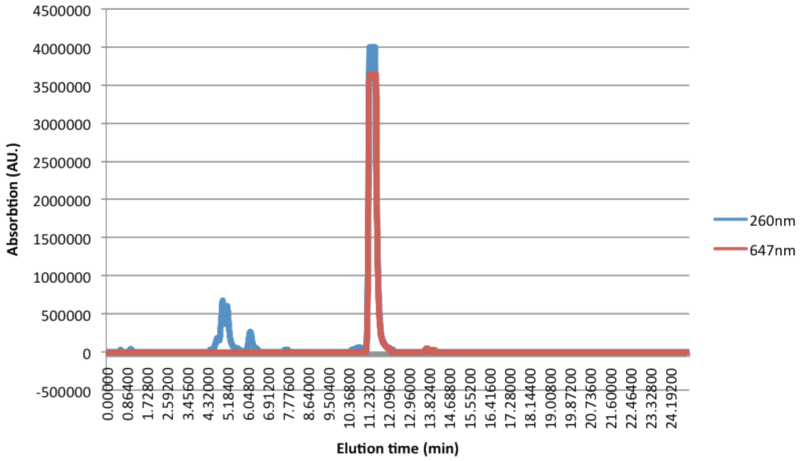

B) AdSucSynth -ATTO647N

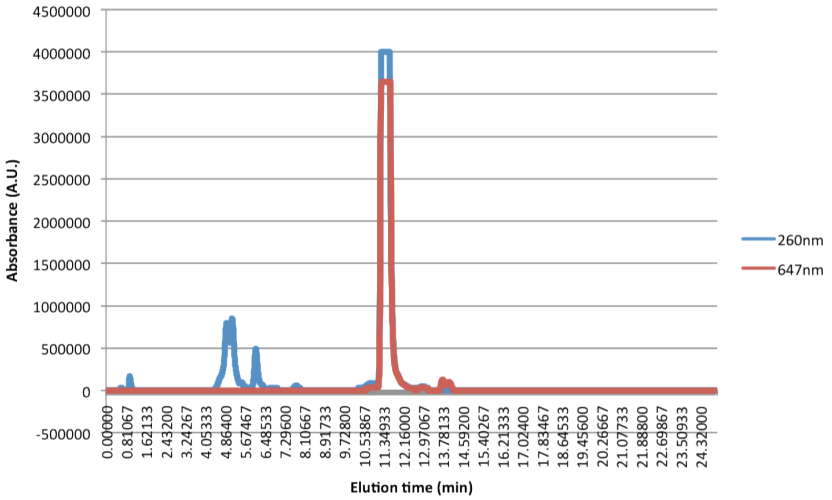

C) IMP-DHG- ATTO647N

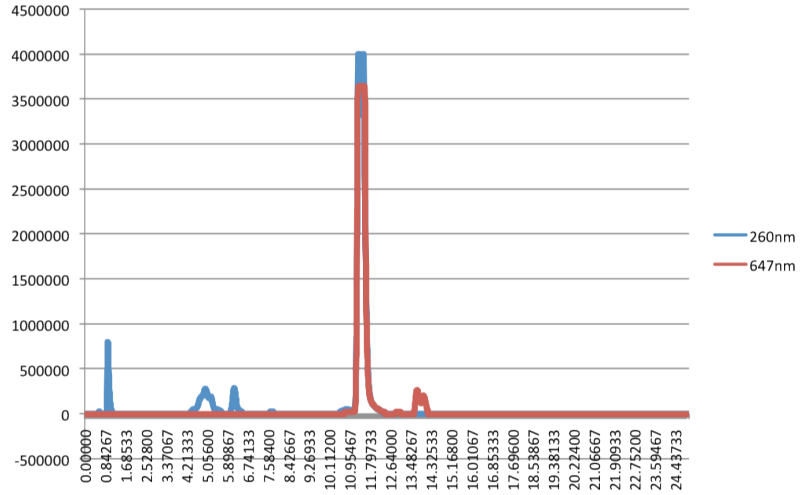

Figure A-11 (previous page): HPLC chromatograms of ATTO647N-conjugated smFISH probe purification. Elution profiles of conjugation reaction mixtures for the purification of ATTO647N-conjugated A) CTPSynthetase , B) Adenyl Succinate Synthetase and C) IMP-dehydrogenase probes. Unconjugated probe elutes as a peak in the 260 nm channel only; fluorophore-conjugated probe is detected as peaks in both the 260 nm and 647 nm channels and unconjugated fluorophore elutes as a peak in the 647 nm channel only.

A) CTPSynth –ATTO495

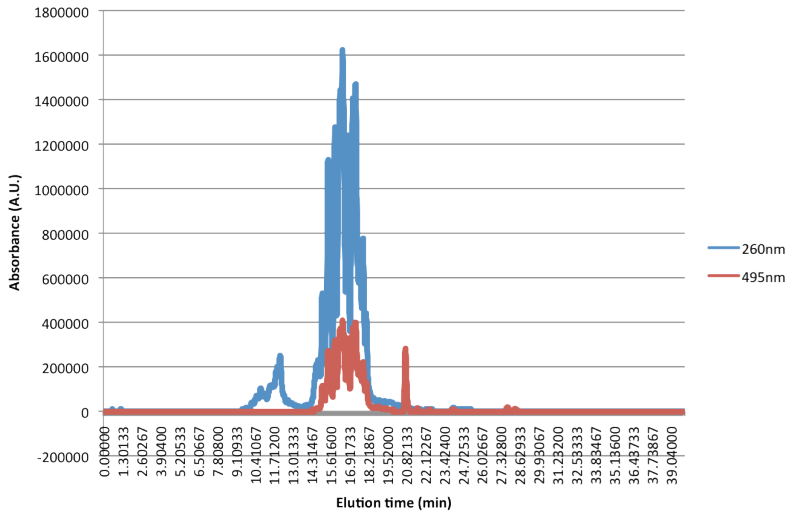

B) AdSucSynth –ATTO495

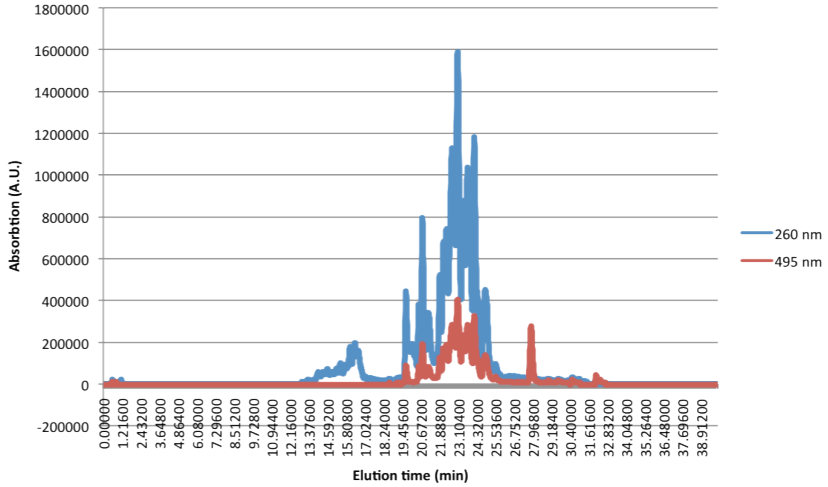

C) IMP-DHG –ATTO495

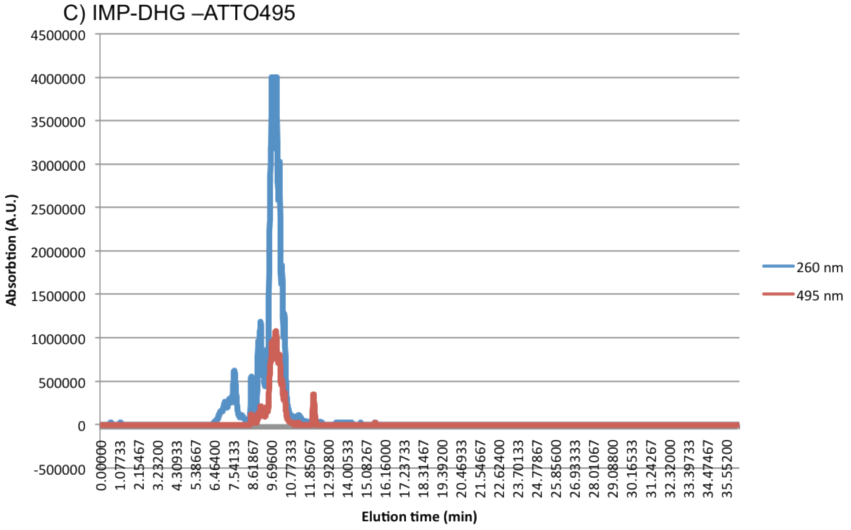

Figure A-12 (previous page): HPLC chromatograms of ATTO495-conjugated smFISH probe purification. Elution profiles of conjugation reaction mixtures for the purification of ATTO495-conjugated A) CTPSynthetase , B) Adenyl Succinate Synthetase and C) IMP-dehydrogenase probes. Unconjugated probe elutes as a peak in the 260 nm channel only; fluorophore-conjugated probe is detected as peaks in both the 260 nm and 495 nm channels and unconjugated fluorophore elutes as a peak in the 495 nm channel only.

Appendix B.1. Image processing methodology

The following methodology was written by Rethabile Kuthlang as a description of the Computational image analysis algorithm implemented by him for this work:

Supervised classification was used to quantify the distributions of the PfMyb2, H3K9ac and H3K9me3 markers in parasite populations. The nuclear distribution of each marker was studied using shape and size features. These features were defined with respect to the nucleus. The classes that describe the marker distributions were heuristically defined. The following classes were derived from the features:

- Cap: a spot that localises on the edge of the nucleus and protrudes outwards.
- Cup: a spot that covers approximately a third of the nuclear perimeter. It is an elongated "cap".
- 1 perinuclear spot: a single spot that localises on the edge of the nucleus.
- 2 perinuclear spots: two spots that localizes on the edge of the nucleus.
- 3+ perinuclear spots: three or more spots localised on the edge of the nucleus.
- Sub-nuclear diffuse region ("Half nucleus diffuse"): a spot that covers a wide area of the nucleus, but less than half.
- Diffuse labeling through nuclear region ("Full nucleus diffuse"): a spot that covers over half the area of the nucleus.

The classification algorithm input consisted of the multi-channel image, with nuclear labels and markers of interest. The nuclear images were passed through a hierarchical K-means filter (Dufour *et al*., 2006) to detect the individual nuclei in the image. The hierarchical K-means function, as implemented in the ICY open-source image analysis platform, iteratively thresholds the image based on a K-means classification of the image histogram. The value of K, the number of clusters, was set to 6. The detected nuclei were then area filtered, with the minimum size set at 10 pixels and maximum size set at 365 pixels. The thresholds were determined empirically. The nuclear marker channels were individually inputted to the spot detection algorithm in ICY, based on the discrete wavelet transform (Olivo-Marin, 2002). The spot detector was set at 100% sensitivity to spots of size 4 to 7 pixels. The algorithm outputted detected spots, which were each categorized into one of the classes by the classifier using the derived features. The script was then able to plot the population distribution

and correlation graphs for each of the *a priori* determined classes so that, for the inputted image, the final output was the detected nuclei, and for each nucleus the co-localising protein was classified into one of the feature based classes. The protein distributions could be manually examined for the set of input images.

References:

Dufour A, Meas-Yedid V, Grassart A, Olivo-Marin JC. 2008. Automated Quantification of Cell Endocytosis Using Active Contours and Wavelet, Proc. ICPR 2008, Tampa, FL, USA.

Olivo-Marin JC. 2002. Extraction of spots in biological images using multiscale products. *Pattern Recognition* 35: 1989-1996.

Appendix B.2. Additional fluorescent labeling results

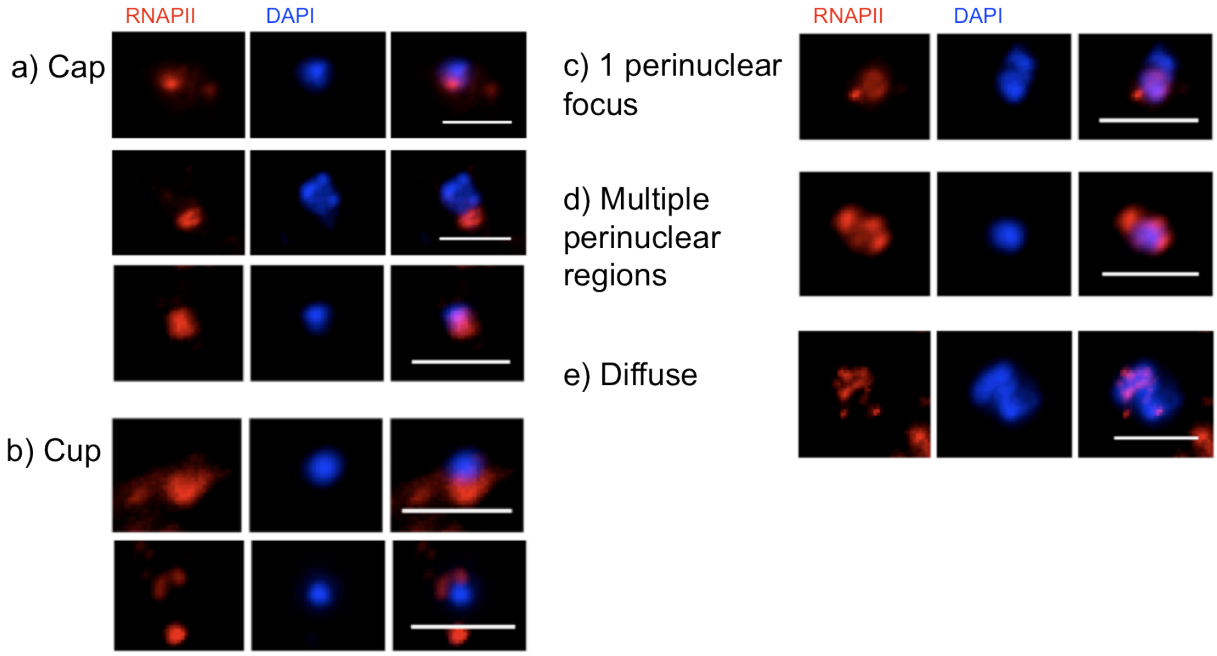

Figure B-1: IF labeling of RNAPII can be assigned to similar classes as those used for PfMyb2 labeling. Representative images of RNAPII labeling (red) that adopt similar sub-nuclear distribution patterns to the a) cap, b) cup, c) single perinuclear foci, d) multiple perinuclear regions and d) diffuse labeling, commonly observed with PfMyb2 labeling. Nuclei are labeled with DAPI (blue). Scale bars =3 μm.